Simulation of Thin Slot Spirals and Dual Circular Patch Antennas Using the Finite Element Method With Mixed Elements

J. Gong, J.L. Volakis and M.W. Nurnberger

National Aeronautics and
  Space Administration
Langley Research Center
Hampton, VA 23681-0001

January 1995

30601-4-T = RL-2423

NASA Grant No. NAG-1-1478

Grant Title: Simulation of Conformal Spiral Slot Antennas on Composite Platforms

Report Authors: J. Gong, J.L. Volakis and M.W. Nurnberger

Report Title: Simulation of Thin Slot Spirals and Dual Circular Patch Antennas Using the Finite Element Method With Mixed Elements

University Project Director: John L. Volakis
volakis@umich.edu
Telephone: (313) 746-0500

NASA-Langley Project
Monitor: Fred Beck
Telephone: (804) 864-1829

University Address: Radiation Laboratory
Department of Electrical Engineering
  and Computer Science
The University of Michigan
Ann Arbor, MI 48109-2122

Date: January, 1995

Table of Contents

Preface

This semi-annual report describes our progress up to mid-January 1995. The report contains five sections all dealing with the modeling of spiral and patch antennas recessed in metallic platforms. Of significance is the development of decomposition schemes which separate the different regions of the antenna volume. These schemes are used in modeling the spiral and the dual circular patch antennas. In the case of the spiral, a mixed (edge and node) element formulation is developed to avoid use of small elements in modeling the slot. This also allows for use of the simpler wire green's function in modeling the radiated fields. Overall, the resulting modeling approach leads to substantial simplifications and is perhaps the most efficient within the context of hybrid FEM formulations. The implementation of this formulation is nearly complete but we already fabricated and tested an archimedean slot spiral operating at a center frequency of 1.1 GHz (see Section 2 of the report). The main goal of the experiment was to examine the feasibility of a new feed design for the slot spiral antenna. This feed design consisted of a microstrip line below the metallic section of the slot spiral but, unfortunately, our first design trial required improvements to bring the axial ratio close to unity. A new design is currently under fabrication and with the help of the new software, it is our hope that the feed design issue will be resolved over the next two months.

Substantial effort was devoted over the past six months in improving the feed model in the context of the FEM. This is addressed in Sections 3 and 4 where we describe simple, but very successful implementations of the coax probe and slot-coupled microstrip line feed. In the latter case, the feed network is modeled using brick elements whereas the antenna volume is modeled using tetrahedrals. The two computational regions were then coupled by enforcing potential continuity (a new approach) across the slot joining the two regions. A design of a dual stacked circular patch configuration is included which demonstrates the validity of the potential continuity condition. Also, as noted in Section 3, the proposed coax cable model yields input impedance results which overlay the measured data.

Finally, Section 5 of the report presents an innovative scheme for truncating finite element meshes. This is an alternative to the absorbing boundary conditions and employs a perfectly matched anisotropic absorber. It was already tested for terminating transmission lines in microwave circuits and we are in the process of implementing it in our FEM antenna codes.

In the next few months our goal is to complete the spiral antenna code and employ it to examine several spiral antenna configurations operating at different bands, including that from 944-1256 MHz as discussed in the proposal. The code will be also enhanced with several features relating to feed modeling and mesh truncation. Finally, additional fabrications and antenna measurements will be made.

Slot Spiral Antenna Modeling Using Hybrid/Mixed FE–BI Technique

Jian Gong and John L. Volakis

Radiation Laboratory

Department of Electrical Engineering & Computer Science

University of Michigan

Ann Arbor, MI 48109-2122

Introduction

This part of the report is concerned with the numerical simulation of the printed Slot Spiral Antenna (SSA) using the finite element – boundary integral (FE–BI) analysis. It has been reported that the FE–BI technique is suited for modeling microstrip patch antennas of any shape, printed on layered planar structure or cylindrical platform and fed with a coaxial cable or a microstripline network underneath the radiating elements (the network feed modeling is referred to the attached article). However, direct application of the hybrid FE–BI technique to thin slot spirals requires excessive sampling rates to accurately simulate the geometry. This is particularly so when edge elements are used for tessellating the cavity volume. Although the edge elements are better suited for modeling metallic edges and corners they cause major meshing difficulties in the case of thin slots in a metallic plane. The edge elements must be specifically designed to have one of their edges perpendicular to the slot and this places severe restriction on the volume mesh in addition to increasing the computational requirements. Moreover, the FEM computational domain beneath the slot spiral antenna may contain a feeding circuitry or dielectric substrate whose structure may have a significant difference in size than that of the thin slot spiral and as a result a large, ill-conditioned system may be obtained.

To alleviate the meshing/modeling difficulties encountered with cavity–backed slot antennas, in this report we describe a mixed finite element–

1

boundary integral formulation. As in the past, the boundary integral is used to describe the radiation of the slot above the cavity. However the cavity is now modeled using a suitable mix of edge and node elements. The latter are used only at the aperture of the thin slot so that the nodes follow the center line of the slot. In this manner, regular size elements can be used regardless of the slot's width and any meshing restrictions are substantially relaxed. The proposed mixed element FE–BI formulation introduces three different computational regions and as expected this complicates the generation of the discrete system. In the following sections, we describe the proposed mixed element FE–BI formulation and proceed with the development of the system by ensuring field continuity at the interfaces of the computational regions. We conclude with the presentation of some preliminary results.

Mixed FEM Formulation

Consider the configuration where a thin slot spiral antenna (SSA) is etched on a dielectric substrate recessed in a cavity enclosed by perfectly electric conducting (PEC) walls. For the purpose of this analysis, the cavity region will be considered as inhomogeneous and of arbitrary geometry. To solve for the field in the interior and exterior region via the finite element method, standard approach is to minimize the functional

$$\mathcal{F} = \frac{1}{2} \int_V \left\{ (\nabla \times \mathbf{E}) \frac{1}{\mu_r} \cdot (\nabla \times \mathbf{E}) - k_0^2 \epsilon_r \mathbf{E} \cdot \mathbf{E} \right\} dV + jk_0 Z_0 \int_S \mathbf{E} \times \mathbf{H} \cdot \hat{n} \, dS, \quad (1)$$

where S denotes the slots cross–section, V is the cavity volume below the slot and $(\mathbf{E}, \mathbf{H})$ are the electric and magnetic fields, respectively. In discretizing $\mathcal{F}$ we must introduce appropriate field expressions in each of the computational regions. On the slots surface the boundary integral will be used to relate the tangential components of $\mathbf{E}$ and $\mathbf{H}$. This yields a functional only in terms of $\mathbf{E}$, and upon differentiating $\mathcal{F}$ with respect to $\mathbf{E}$ we then obtain a system of equations for the solution of the node/edge fields. Since the cavity volume consists of node and edge elements, we consider two field expressions. For the eth element these are of the form

$$\mathbf{E}^e = \begin{cases} \sum_{k=1}^{6} E_k \mathbf{V}_k(\mathbf{r}) & \mathbf{r} \in V_1 \\ \sum_{q=1}^{4} (\hat{x} E_{xq} + \hat{y} E_{yq} + \hat{z} E_{zq}) N_q(\mathbf{r}) & \mathbf{r} \in V_2 \end{cases}, \quad (2)$$

where V_1 and V_2 denote the volumes occupied by the edge and node elements, respectively. The coefficients E_k represents the edge fields at the kth

2

edge–based shape functions defined in [1]. Similarly, N_q denotes the node–based shape function for the node q and E_{xq} is the field coefficient for the x-component of the nodal field. The node–based shape functions are given by

$$N_i(\mathbf{r}) = \frac{a_i + b_i x + c_i y + d_i z}{6V^e}, \quad i \Longrightarrow i, j, m, n \tag{3}$$

where

$$V^e = \frac{1}{6} det \begin{vmatrix} 1 & x_i & y_i & z_i \\ 1 & x_j & y_j & z_j \\ 1 & x_m & x_m & z_m \\ 1 & x_n & y_n & z_n \end{vmatrix} \tag{4}$$

is the eth element volume and

$$
\begin{aligned}
a_i &= +det \begin{vmatrix} x_j & y_j & z_j \\ x_m & y_m & z_m \\ x_n & y_n & z_n \end{vmatrix}, & b_i &= -det \begin{vmatrix} 1 & y_j & z_j \\ 1 & y_m & z_m \\ 1 & y_n & z_n \end{vmatrix}, \\
c_i &= -det \begin{vmatrix} x_j & 1 & z_j \\ x_m & 1 & z_m \\ x_n & 1 & z_n \end{vmatrix}, & d_i &= -det \begin{vmatrix} x_j & y_j & 1 \\ x_m & y_m & 1 \\ x_n & y_n & 1 \end{vmatrix},
\end{aligned}
\tag{5}
$$

in which the indices i, j, m, n are in the cyclic order and represent the node numbers of the eth element.

A special attention shall be paid to the treatment for the nodes in the slot, along whose axis the tangential $\mathbf{E}$ component must be set to zero in order to satisfy the boundary condition. This can be accomplished by rewriting the second expression in (2) as

$$\mathbf{E}^e = \sum_{q=1}^{3} (\hat{x} E_{xq} + \hat{y} E_{yq} + \hat{z} E_{zq}) N_q(\mathbf{r}) + (\hat{m} E_{m4} + \hat{z} E_{z4}) N_4(\mathbf{r}), \tag{6}$$

if the $4th$ node happens to be in the slot, and $\hat{m} = \hat{z} \times \hat{l}$. It is observed that this boundary condition treatment indeed reduces the degree of freedom for each node from three to two. The nodes on pec walls may similarly be dealt with using this technique and in particular the degrees of freedom for each node on pec walls becomes one. Therefore, one has the expansion

$$\mathbf{E}^e = \sum_{q=1}^{3} (\hat{x} E_{xq} + \hat{y} E_{yq} + \hat{z} E_{zq}) N_q(\mathbf{r}) + \hat{z} E_{z4} N_4(\mathbf{r}), \tag{7}$$

assuming the 4*th* node is on a pec wall. If an element's facet coincides with the pec ground plane, the degrees of freedom associated with this element will be 6 rather than 12, as is usually the case. The implementation of boundary condition is treated at the stage of entry generation and matrix assembly to avoid redundant matrix size declaration.

From the above, the field everywhere in $V = V_1 + V_2$ can then be expressed in discrete form as

$$\mathbf{E} = \sum_e \mathbf{E}^e, \tag{8}$$

and when this is substituted in (1) we obtain the system of equations

$$\sum_{e_1 \in V_1} \left[A^{(1)} \right] \{E_k\} + \sum_{e_2 \in V_2} \left[A^{(2)} \right] \{E_{qx}\} + \{BI - subsystem\} = 0. \tag{9}$$

These element equations must be assembled to generate a partly sparse, partly full system of equation, and in doing so it is necessary to identify the relationships among the edges, nodes and boundary field coefficients. In addition, the node shape functions defined in (3) are not divergence free, i.e. they do not satisfy the $\nabla \cdot \mathbf{E} = 0$ condition, and thus to eliminate non–Maxwellian solutions, it is instructive to add the term

$$\int_{e_2 \in V2} \frac{1}{\mu_r} \left\{ \sum_u \nabla N_q \cdot \hat{u} \right\} \left\{ \sum_u \nabla N_p \cdot \hat{u} \right\} dV \tag{10}$$

to the matrix element of $\left[A^{(2)} \right]$. Note the sum in $\{\}$ is over the u (= x, y and z) components. The assembly of the element equations is more challenging for our specific case because of the mixed volume elements and their interface with the boundary elements. Before addressing this issue, we first describe the formulation of the BI subsystem, thus completing the specification of the element equations (9).

Boundary Integral For Thin Slot/Wire Structure

As already presented in the above section, the functional (1) contains a term involving the tangential component of the magnetic field, $\hat{n} \times \mathbf{H}$, on the aperture S or the slot area(s), where $\hat{n}$ is normal to the aperture and for our case $\hat{n} = \hat{z}$. This field should be represented via an integral equation in terms of the electric field $\mathbf{E}$ or the equivalent magnetic current in the thin

slot. To construct the integral equation, we start with a mixed potential integral equation for thin wires of arbitrary shape. Figure 2 shows the top view of a thin spiral slot antenna which is located on the boundary separating the exterior free space from the finite element 3D domain (cavity).

The complementary physical problem corresponds to an electrically conducting thin wire of arbitrary shape carrying the electric current $\mathbf{I}_e$ along only the axial direction. The associated integral equation can be written as

$$\hat{l} \cdot \left\{ \mathbf{E} = -j\omega\bar{A} - \nabla\phi \right\} = \begin{cases} \hat{l} \cdot \mathbf{E}^i & \mathbf{r} \in source\ gap \\ 0 & otherwise \end{cases}, \qquad (11)$$

where $\mathbf{E}^i$ represents a plane wave incidence or a delta gap source, $\hat{l}$ is a unit vector tangential to the thin wire at point $\mathbf{r}$ and

$$\bar{A} = \mu \int_l G\mathbf{I}_e\,dl, \quad \phi = j\frac{\nabla \cdot \bar{A}}{\omega\mu_0\epsilon_0} = \frac{j}{\omega\mu_0}\nabla \cdot \int_l G\mathbf{I}_e\,dl. \qquad (12)$$

In these, $\mathbf{I}_e$ is the electric current and G the free space Green's function

$$G(\mathbf{r}, \mathbf{r}') = \frac{e^{-jk|\mathbf{r}-\mathbf{r}'|}}{4\pi\omega_0\epsilon_0}$$

On substituting (12) into (11), we obtain the integral euqtion

$$0 = \hat{l} \cdot jkZ_0 \int_l \left\{ \bar{\bar{\delta}} + \frac{1}{k^2}\nabla\nabla \right\} G \cdot \mathbf{I}_e\,dl + \begin{cases} \hat{l} \cdot \mathbf{E}^i & \mathbf{r} \in source\ gap \\ 0 & otherwise \end{cases}. \qquad (13)$$

in which $\bar{\bar{\delta}}$ is the unit dyad.

The quadratic basis functions

$$\mathbf{r}(\xi) = 2(\xi - \frac{1}{2})(\xi - 1)\mathbf{r}_{n-1} + 4\xi(1 - \xi)\mathbf{r}_{n-1/2} + 2\xi(\xi - \frac{1}{2})\mathbf{r}_n, \qquad (14)$$

where $n = 1, 2, \ldots, N$, are chosen to expand the electric current $\mathbf{I}_e$ and ξ is the simplex coordinate whose range is $[0, 1]$. Galerkin technique for the residual testing is employed for the method of moment (MoM) implementation of (13), and it should be remarked that the thin structure assumption (which is adequate for spiral antenna analysis) leads to a one dimensional boundary integral subsystem. This significantly increases the efficiency of the simulation and the geometry is prescribed using an independent pre–process program to generate a 'five–point per record' (corresponding to two adjacent segments) data set as an input file. The singularity for the self–cell entries
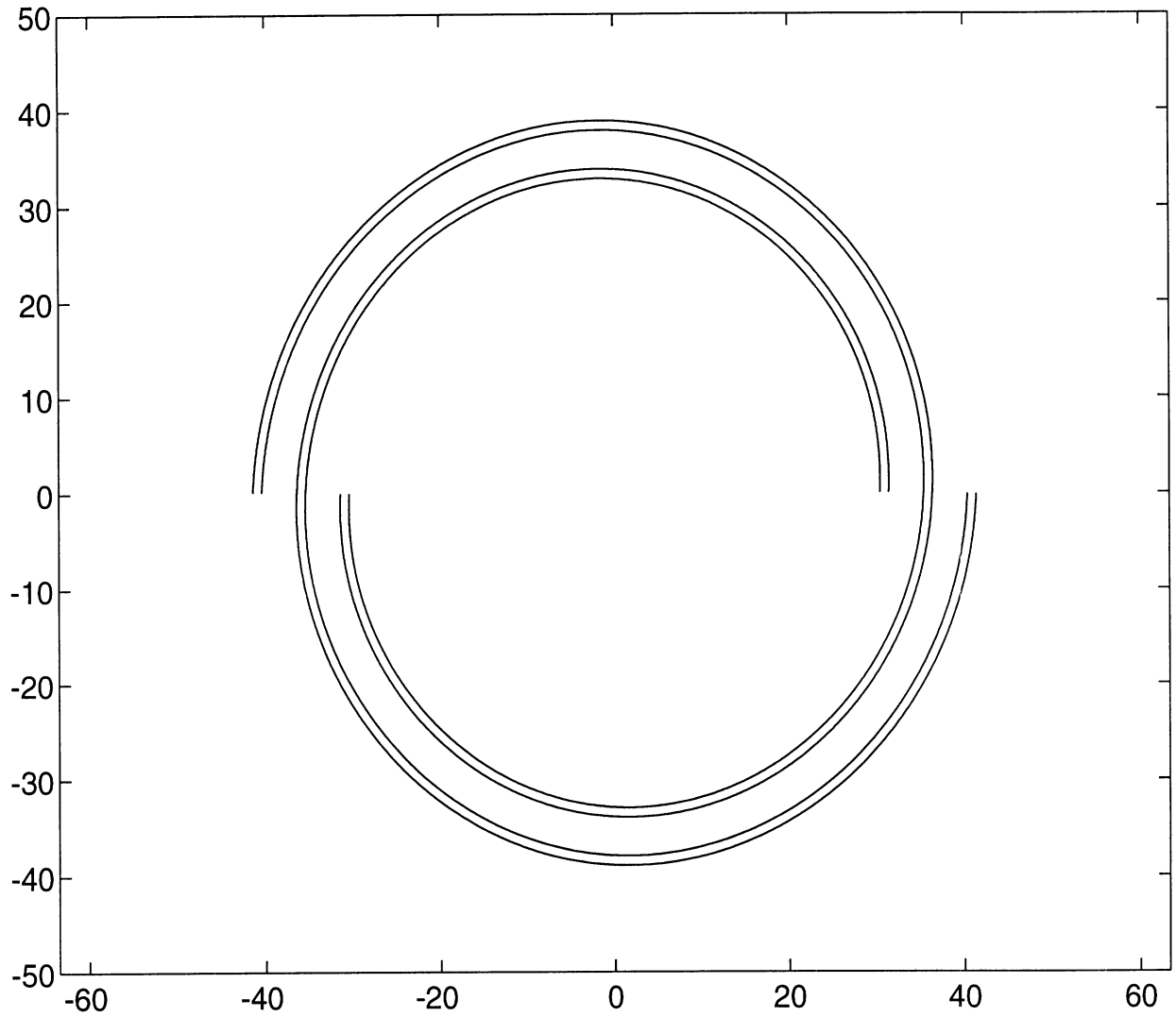
Figure 1: A typical spiral slot etched on top of ground plane. The spiral is defined as $r = a\theta + b$ for one arm and a, b may be determined by $a = \frac{r_2 - R_1}{\theta_2 - \theta_1}$, $b = r_1 - a\theta_1 = r_2 - a\theta_2$, where $r_{1,2}\theta_{1,2}$ represent the polar coordinates for the inner ends and outer ends, respectively.

is dealt with by assuming a finite width spiral slot structure and this leads to a simple numerical evaluation of the matrix elements. The accuracy of this implementation was validated by comparing with the referenced data available in the literature [2, 3, 4]. Figure 2 and 3 show the comparison of real and imaginary parts for the electric currents generated by a voltage gap excitation on a circular wire ring. Indded an excellent agreement is observed.

Additional results for different thin spiral configurations are given later in this part of the report and these clearly show the promising capability of the technique.

Returning to the surface integral of then functional (1), we have

$$jkZ_0 \int_S \mathbf{E} \times \mathbf{H} \cdot \hat{n} \, dS = -jkZ_0 \int_l (\mathbf{E} \times \hat{z}) W \cdot \mathbf{H} \, dl \qquad (15)$$

with $dS = W \, dl$ and W is the width of the slot. If $W(\mathbf{E} \times \hat{z})$ is defined as an equivalent (line) magnetic current, the magnetic field $\mathbf{H}$ measured at the $z = 0$ plane can be expressed as

$$\mathbf{H} = -jk_0 Y_0 \int_{l'} \bar{\bar{G}}_m \cdot \mathbf{I}'_m \, dl' \qquad (16)$$

where $\bar{\bar{G}}_m$ is

$$\bar{\bar{G}}_m = 2 \left\{ \bar{\bar{\delta}} + \frac{1}{k_0^2} \nabla\nabla \right\} G,$$

in which the factor of 2 accounts for the ground plane contribution. Then (15) becomes

$$-jkZ_0 \int_l (\mathbf{E} \times \hat{z}) W \cdot \mathbf{H} \, dl = -k_0^2 \int_l \int_{l'} \mathbf{I}_m \cdot \bar{\bar{G}}_m \cdot \mathbf{I}_m \, dl' \, dl \qquad (17)$$

$$= -2k_0^2 \int_l \int_{l'} \mathbf{I}_m \cdot \left\{ \bar{\bar{\delta}} + \frac{1}{k_0^2} \nabla\nabla \right\} G \cdot \mathbf{I}'_m \, dl' \, dl.$$

Note that following the standard discretization procedure, the magnetic currents $\mathbf{I}_m$ and $\mathbf{I}'_m$ in (18) are expanded using the quadratic basis functions in (14) in terms of a one dimensional variable ξ and this variable number reduction is due to the application of a prescribed geometry date set, as aforemention. We observe that the unknown coefficients for both currents at the observation and source points, respectively, should be treated in different manner. That is, the differentiation for extremization is only applied to the current coefficients at the observation points, remaining those at the source points constant. This formulation leads to a same discrete form integral

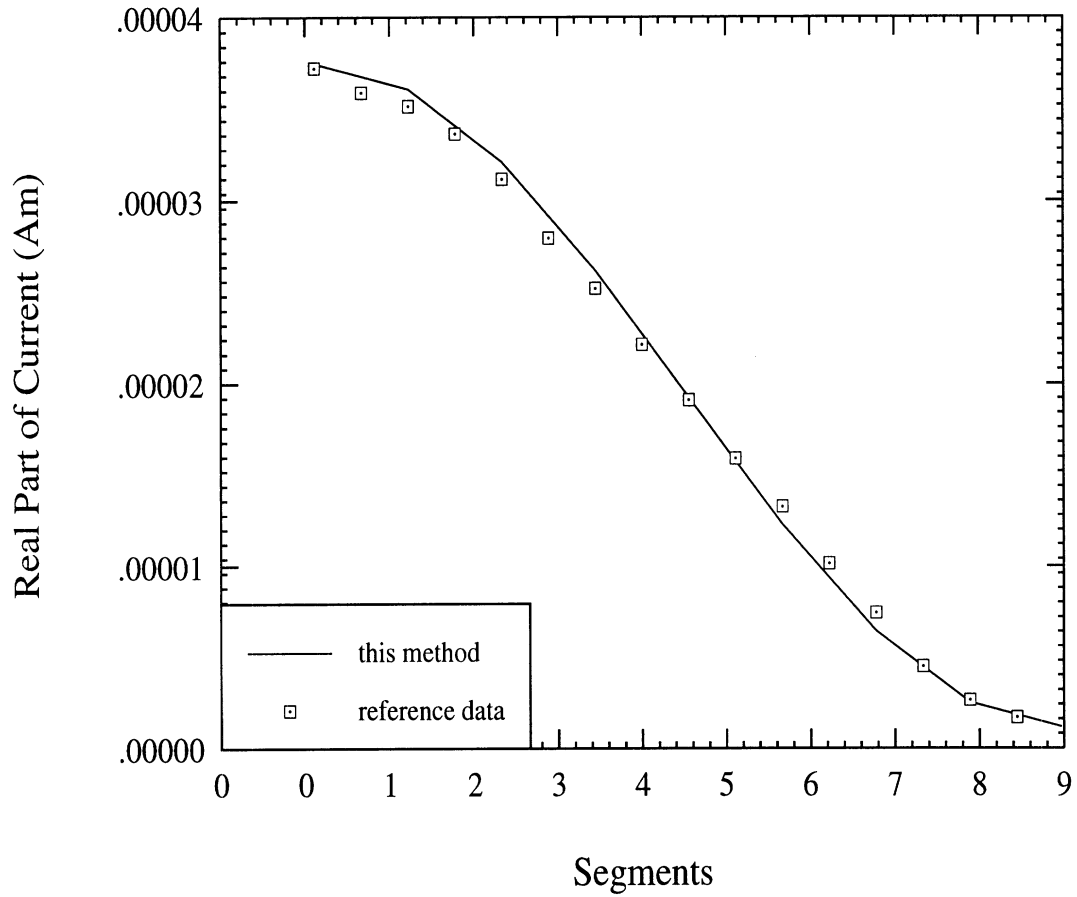# The Real Part of Current on a Circular Loop Wire

Figure 2: Real part of current in a circular wire ring antenna of radius 0.0627λ at 3 GHz.

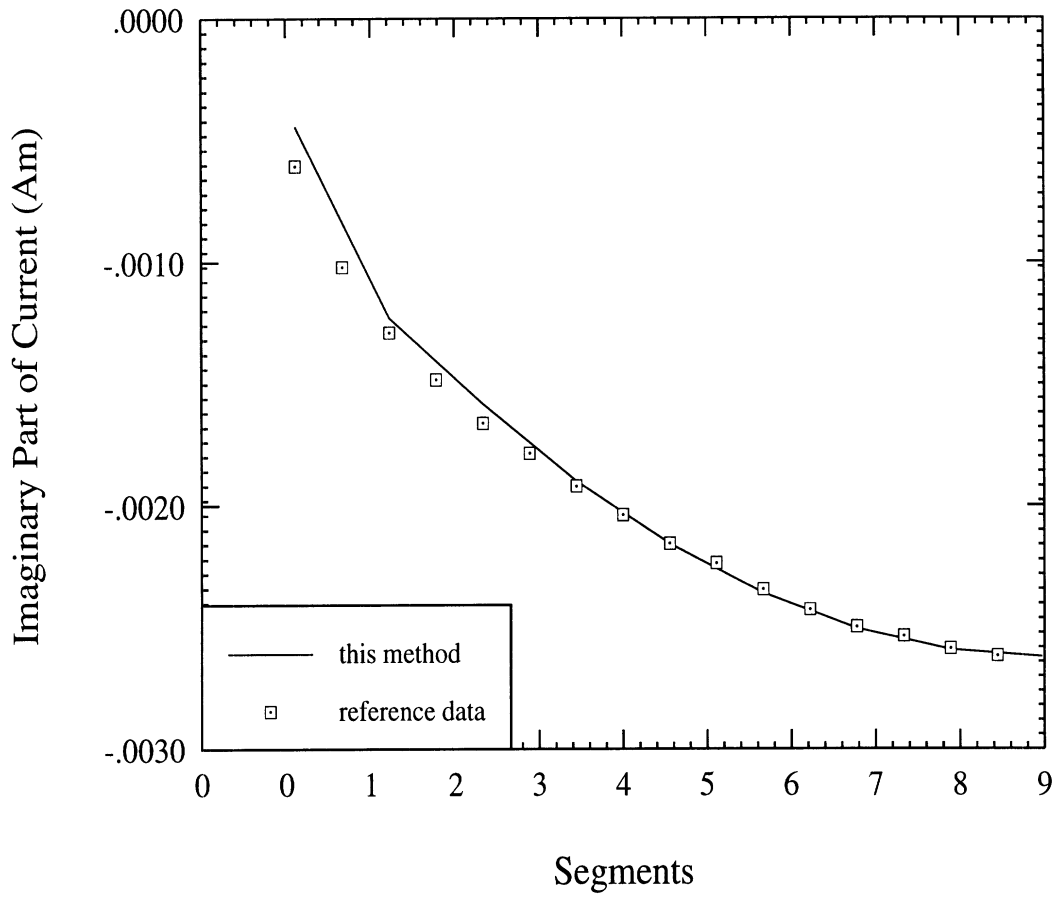# Imaginary Part of Current on Loop Wire

Figure 3: Imaginary part of current in the same circular ring wire antenna as in figure 2.

9

equation as the one derived from (13), where Galerkin's technique was used, except for a constant factor.

It should be noted that in implementing the method of moment for the slot spiral, the finite width W of the slot has to be involved (to maintain the correct units) and indeed it is an important geometric parameter for the spiral description when the Green's function is evaluated at the self–cell terms. In addition, the forms for the dyadic Green's function and the equivalent magnetic current are not arbitrarily chosen; usually one determines the other. However, the overall result should always give rise to the same answer.

System Combination

We describe in this section the issues relating to the interface of edge and node–based element regions, as well as the generation of the overall system for solution. For discussion purposes, the following notation is used in this section:

- Three subsystems:

    a. edge–basis FEM: $\mathbf{E}^a$

    b. node–basis FEM: $\mathbf{E}^b$

    c. BI: $\mathbf{E}^s$

- Basis functions:

    a. edge–basis: $\mathbf{V}_i$

    b. node–basis: $\mathbf{N}_j$

    c. BI: $\mathbf{S}_q$

It is known that the hybrid FE–BI system is conventionally combined by enforcing the continuity of the tangential electric fields on the aperture linking the cavity field unknowns and those in the boundary integral. For patch antennas, since the aperture size is relatively large around the patch, this practice is appropriate. However, in the presence of the thin slots, this scheme is no longer valid because it would lead to very fine meshes and thus a large number of unknowns. This difficulty is avoided herewidth by making use of nodal elements in the thin slot and its adjacent region. In particular, applying (6) and (7) for field expansions offers the inherent opportunity of combining the fields above and below the slot without a need to either increase the mesh sampling rate or carry out interpolations, both of which

worsen the system condition. The way of combining the node–based FEM system b with a thin slot BI is similar to that for patch antenna simulation where the cavity unknowns beneath the ground plane coincide with the BI unknowns. Here, we choose nodal basis elements and the field unknowns in the slot are defined on specific *nodes* in both system b and the BI subsystem. A one-to-one correspondence of the fields in these two subsystems allows a direct combination (see [1]).

Consider the two separate FEM subsystems (one for nodal elements and the other for edge elements). It is apparent that explicit coupling across their interface is needed and in this report we propose a technique to couple the node and edge–based FEM systems without altering the condition number. Consider an interface Γ between region V_1 (edge elements) and V_2 (node elements). Since the tangential field continuity requires

$$\hat{t} \cdot \mathbf{E}^{(a)} = \hat{t} \cdot \mathbf{E}^{(b)}, \qquad \mathbf{r} \in \Gamma \tag{18}$$

where $\hat{t}$ is a tangential unit vector in Γ and

$$\mathbf{E}^{(a)} = \sum_i E_i^{(a)} \mathbf{S}_i(\mathbf{r}), \qquad \mathbf{E}^{(b)} = \sum_j E_j^{(b)} \mathbf{N}_j(\mathbf{r}). \tag{19}$$

The expansion functions $\mathbf{S}_i(\mathbf{r})$ lie in the interface Γ, i.e., there is no normal component perpendicular to the interface; but functions $\mathbf{N}_j(\mathbf{r})$, in general, have both components. If $\hat{m}$ is defined to be normal to the interface, then (18) may be rewritten as

$$\hat{m} \times \hat{m} \times \mathbf{E}^{(b)} = \mathbf{E}^{(a)} \qquad \mathbf{r} \in \Gamma \tag{20}$$

or

$$\hat{m} \times \hat{m} \times \sum_j E_j^{(b)} \mathbf{N}_j(\mathbf{r}) - \sum_i E_i^{(a)} \mathbf{S}_i(\mathbf{r})$$
$$= \sum_j E_j^{(b)} \mathbf{P}_j(\mathbf{r}) - \sum_i E_i^{(a)} \mathbf{S}_i(\mathbf{r}) = 0 \tag{21}$$

where $\mathbf{P}_j(\mathbf{r}) = \hat{m} \times \hat{m} \times \mathbf{N}_j(\mathbf{r})$. We introduce a vector residue

$$\mathbf{R} = \sum_j E_j^{(b)} \mathbf{P}_j(\mathbf{r}) - \sum_i E_i^{(a)} \mathbf{S}_i(\mathbf{r}), \tag{22}$$

and a functional term for coupling the system a and b may then be given by

$$\mathcal{F}^{ab} = \int_\Gamma \bar{\lambda} \cdot \mathbf{R} \, dS. \tag{23}$$

11

$\bar{\lambda}$ is called a *vector* Lagrange multiplier (as opposed to a conventional scalar multiplier) and it may be expanded in terms of vector basis functions in the same fashion for vector fields $\mathbf{E}$. In particular, we assume an expansion function $\mathbf{T}_p$ and

$$\bar{\lambda} = \sum_p \lambda_p \mathbf{T}_p(\mathbf{r}). \tag{24}$$

Hence,

$$\mathcal{F}^{ab} = \int_\Gamma \sum_p \lambda_p \mathbf{T}_p(\mathbf{r}) \cdot (\sum_j E_j^{(b)} \mathbf{P}_j(\mathbf{r}) - \sum_i E_i^{(a)} \mathbf{S}_i(\mathbf{r})) \, dS. \tag{25}$$

Differentiation with respect to λ_p, E_i and E_j yields,

$$\frac{\partial \mathcal{F}^{ab}}{\partial \lambda_p} = \sum_j E_j^{(b)} \int_\Gamma \mathbf{T}_p \cdot \mathbf{P}_j \, DS - \sum_j E_i^{(a)} \int_\Gamma \mathbf{T}_p \cdot \mathbf{S}_i \, DS$$

$$\frac{\partial \mathcal{F}^{ab}}{\partial E_j^{(b)}} = \sum_p \lambda_p \int_\Gamma \mathbf{T}_p \cdot \mathbf{P}_j \, DS$$

$$\frac{\partial \mathcal{F}^{ab}}{\partial E_i^{(a)}} = -\sum_p \lambda_p \int_\Gamma \mathbf{T}_p \cdot \mathbf{S}_i \, DS \tag{26}$$

These are the explicit expressions for coupling the subsystems a and b (first two discrete terms in (9)). It is observed that when the expansion function $\mathbf{T}_p$ is proporly chosen, the entire discrete system of equations is symmetric after combination of the three subsystems. This is one of the most significant and attractive features of the formulation proposed and described in this report.

It should be remarked that this hybrid FEM formulation, regardless of its complexity, is promising and capable of simulating a thin slot antenna supported by a cavity or cascaded cavity structure that is recessed in a planar or curved platform. More composite configurations such as aperture coupled feeding network or inhomogeneous dielectric fillings may be tackled with no extra burden.

12

References

[1] J. Gong, J.L. Volakis, A.C. Woo and H. G. Wang, "A Hybrid Finite Element-Boundary Integral Method for the Analysis of Cavity-backed Antennas of Arbitrary Shape," *IEEE Trans Antenna and Propagat.*,Vol. 42, No. 9, pp 1233–1242, 1994

[2] N.J. Champagne II, J. Williams and D.R. Wilton, "The use of curved segments for numerically modeling thin wire antennas and scatterers," *IEEE Trans Antenna and Propagat.*,Vol. 40., No. 6, pp 682–689, 1992

[3] H. Nakano, S. Okuzawa and H. Mimaki, "Two-arm slot spiral antenna," *Electromagnetics,* Vol. 14, No. 3-4, pp 397–413, 1994

[4] H. Nakano *Spiral and helical antennas,*
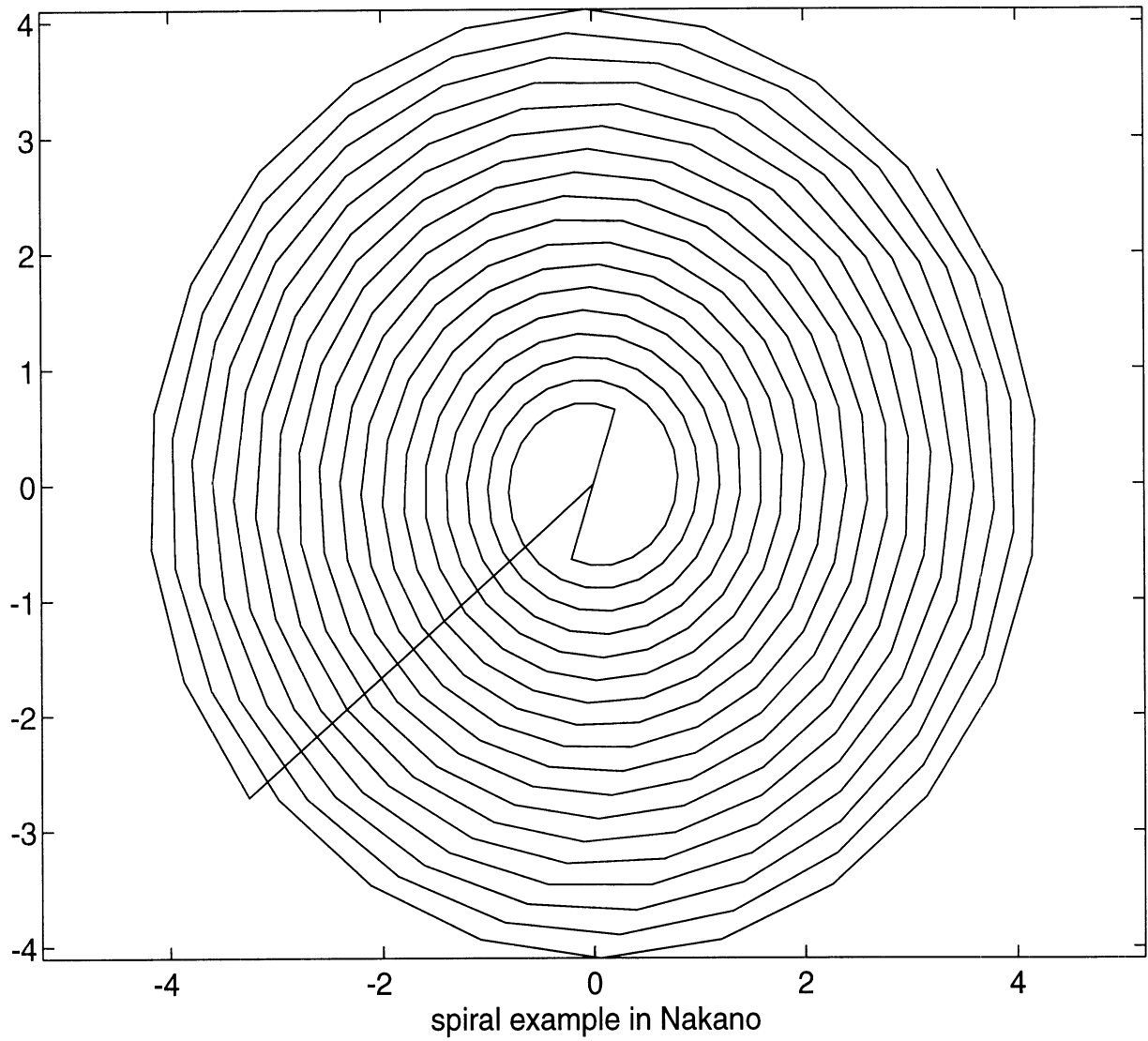
Figure 4: Geometry of a two arm Archemedeam Spiral in refernece [4]. The line connecting the outer end to the center is not present in practice and the feeds are located at two inner ends.
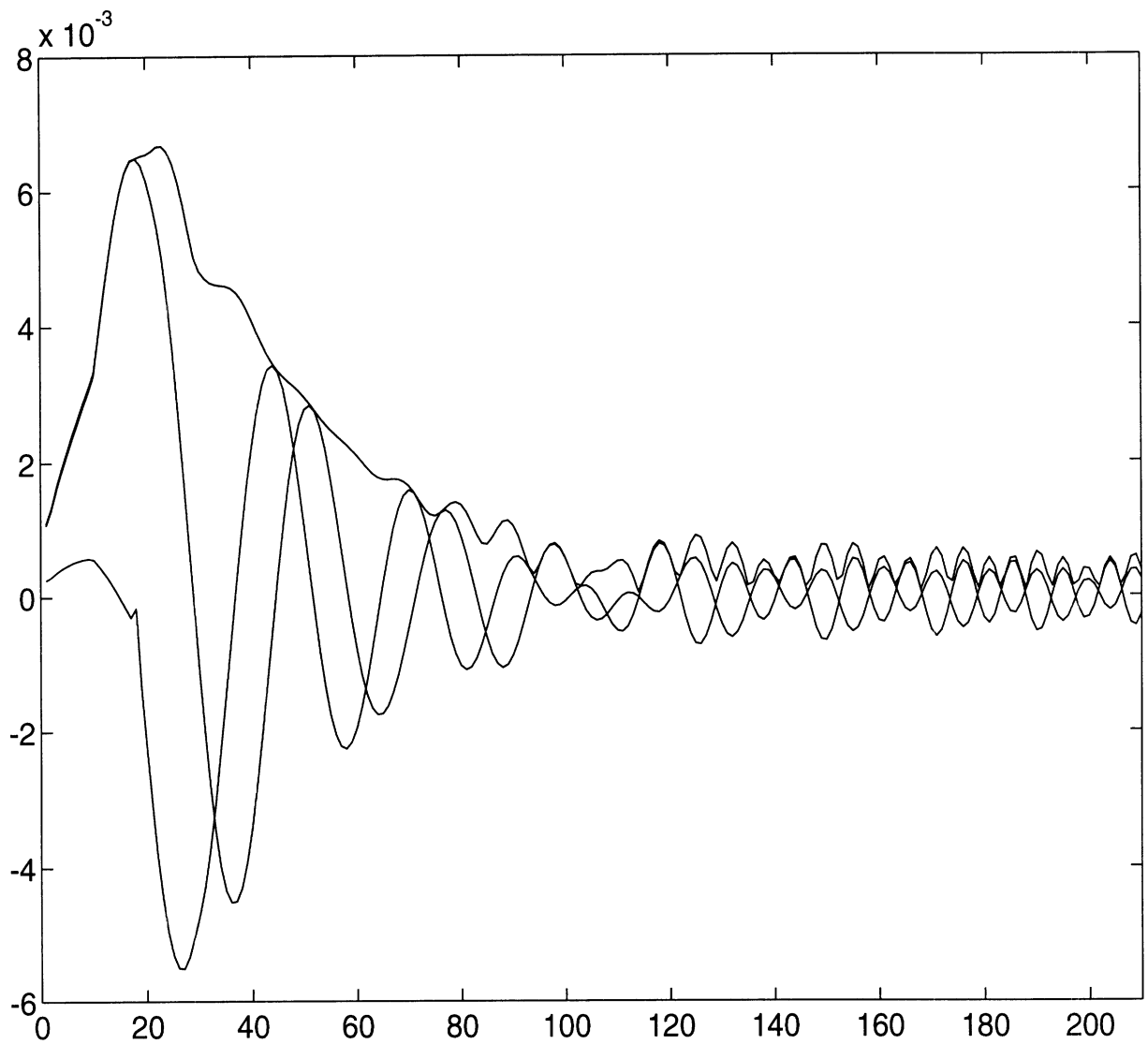
Figure 5: Predicted current distributions on the spiral in figure 4 and an excellent agreement is observed in comparison to the results shown in [4].
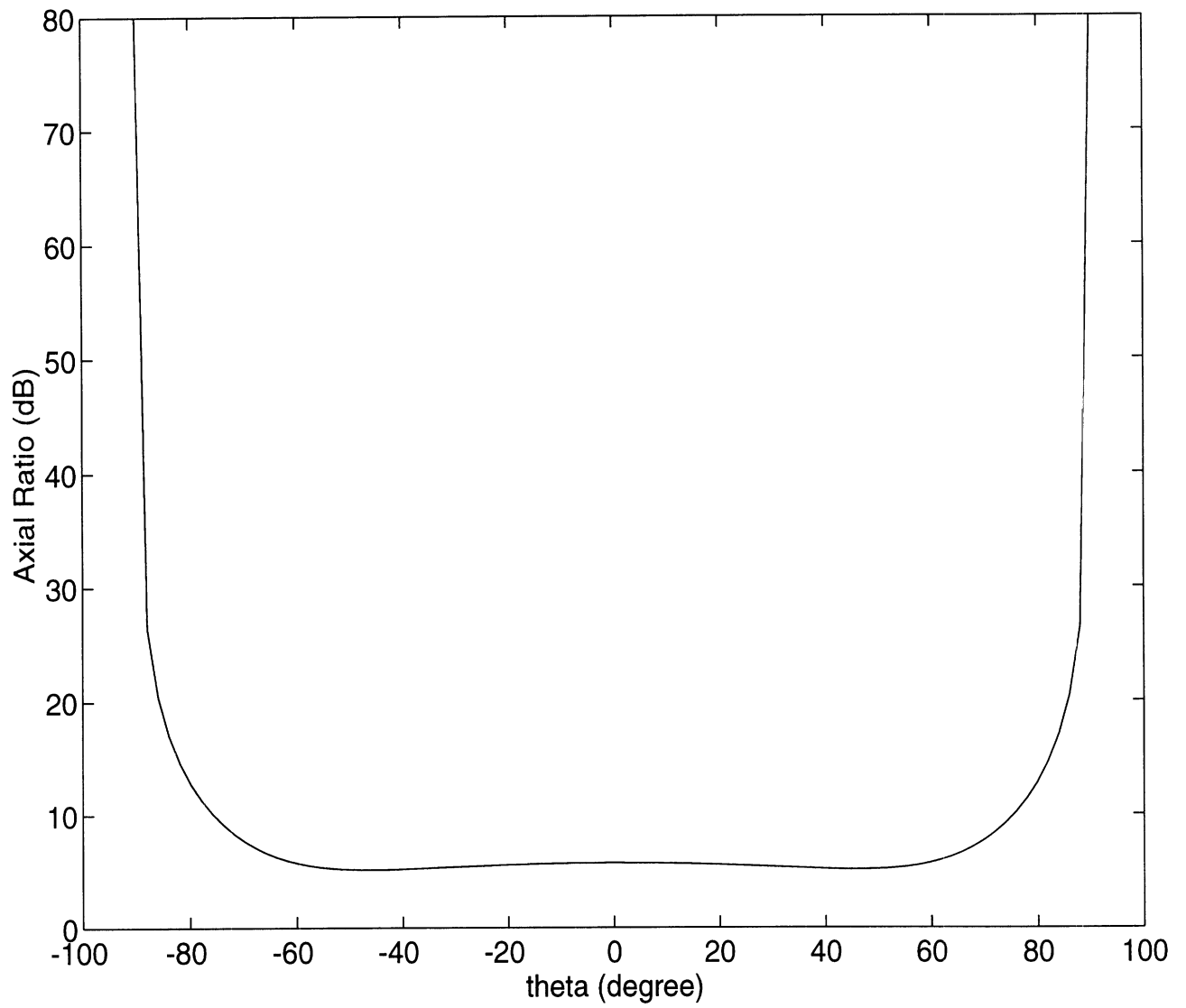
Figure 6: Axial ratio vs. θ for the two-arm spiral antenna shown in fihure 1.
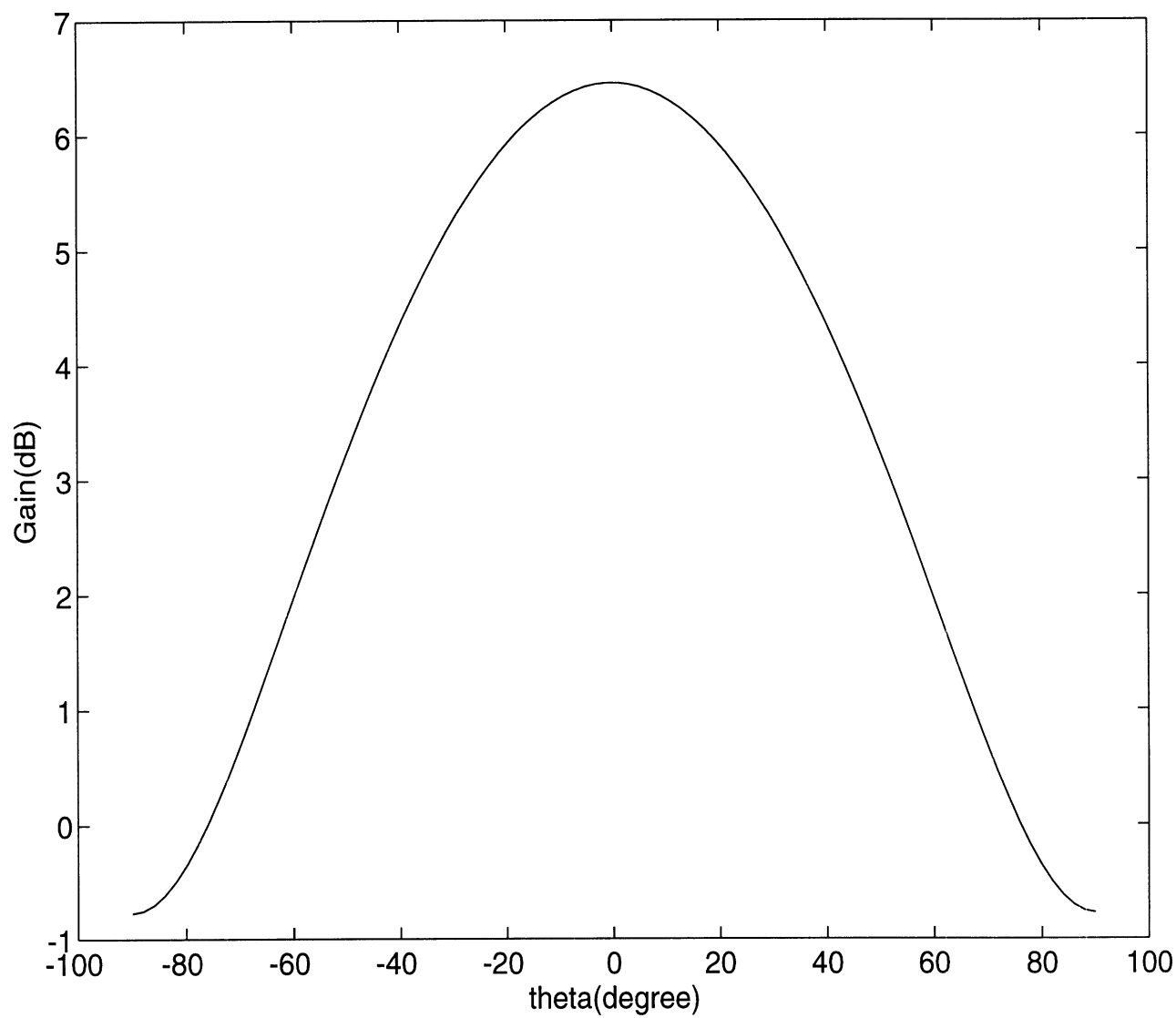
Figure 7: Gain pattern vs. θ for the spiral in figure 1.

17
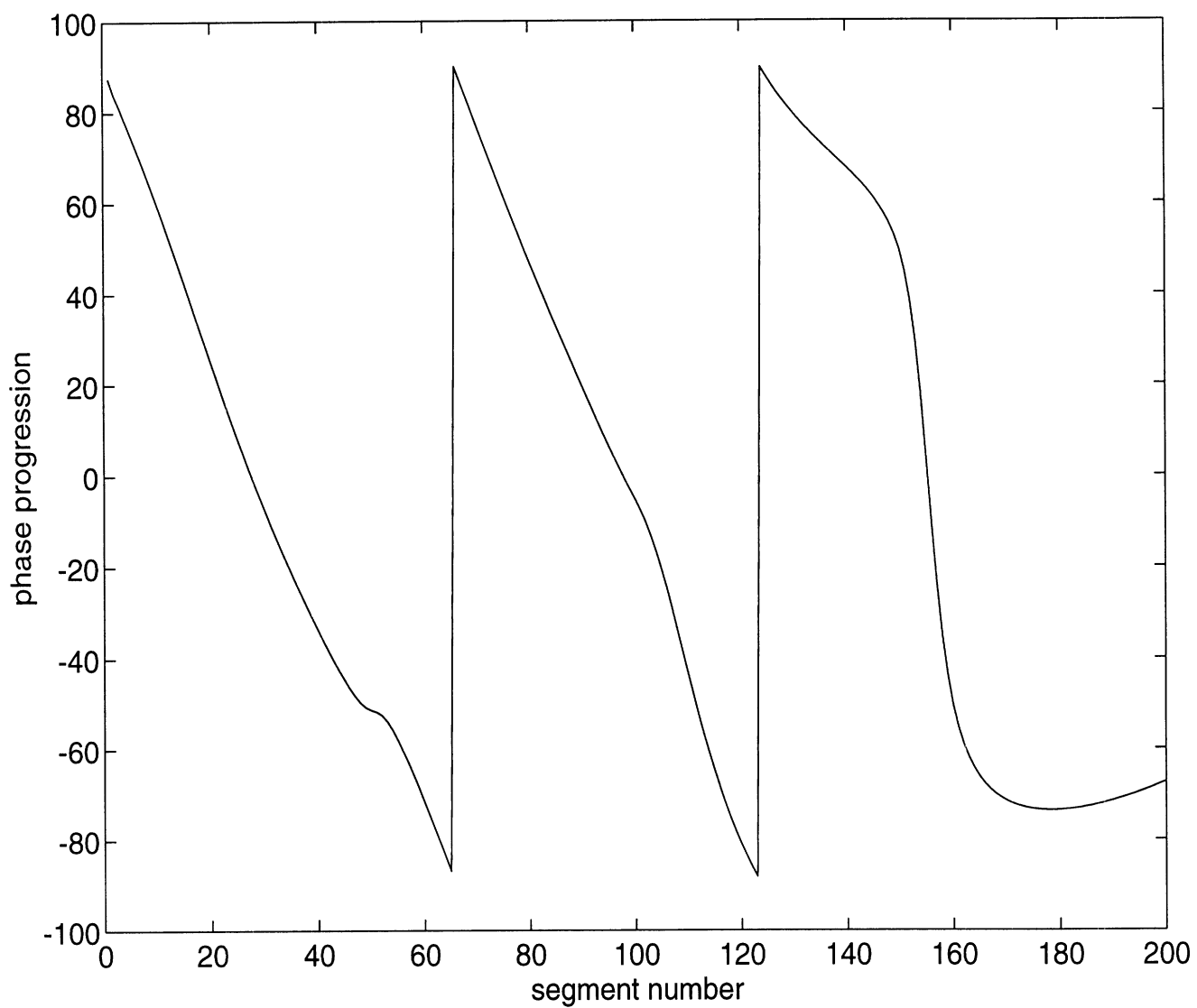
Figure 8: Phase changes along the spiral in figure 1.
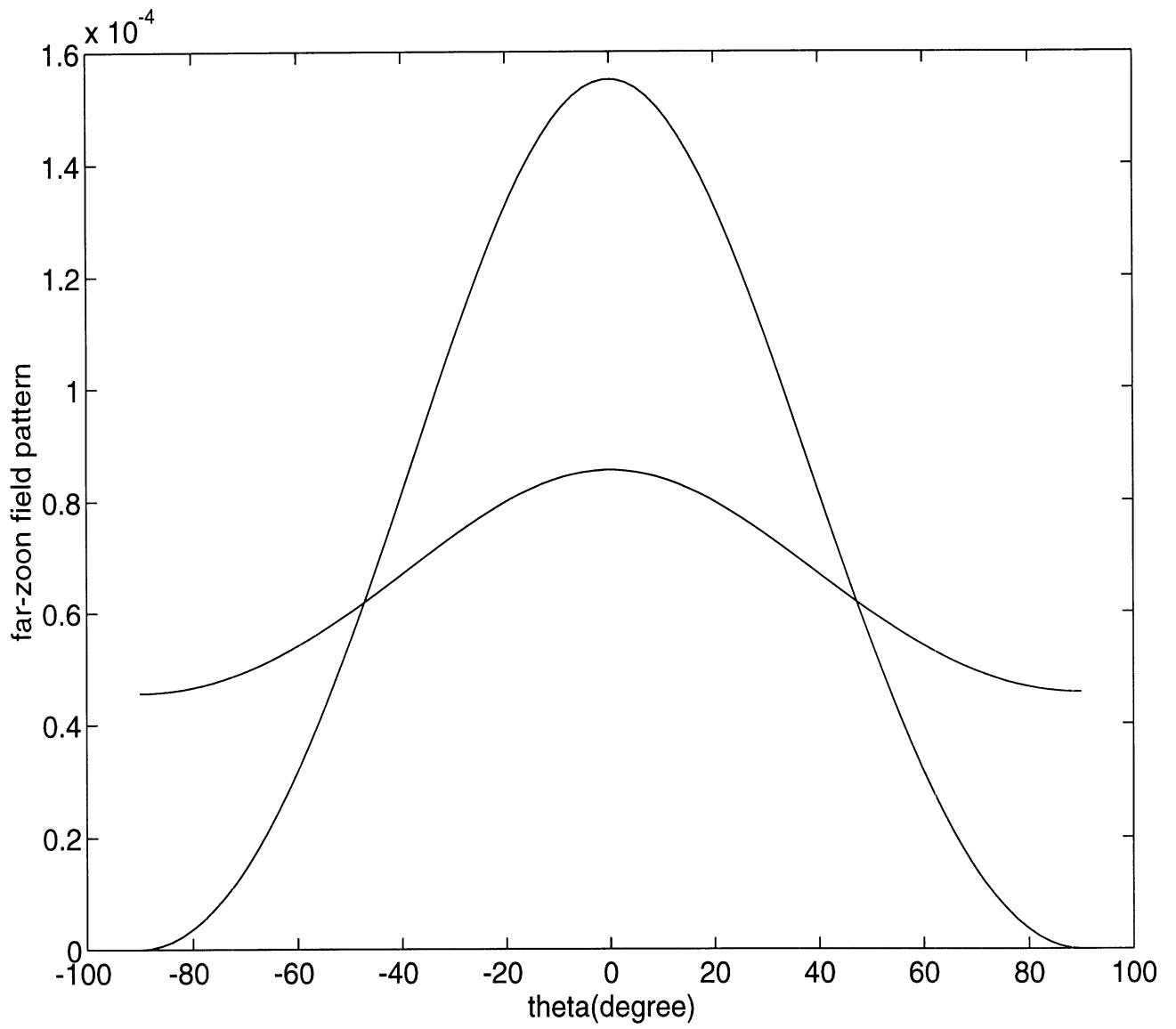
Figure 9: Radiation pattern for the spiral in figure 1.
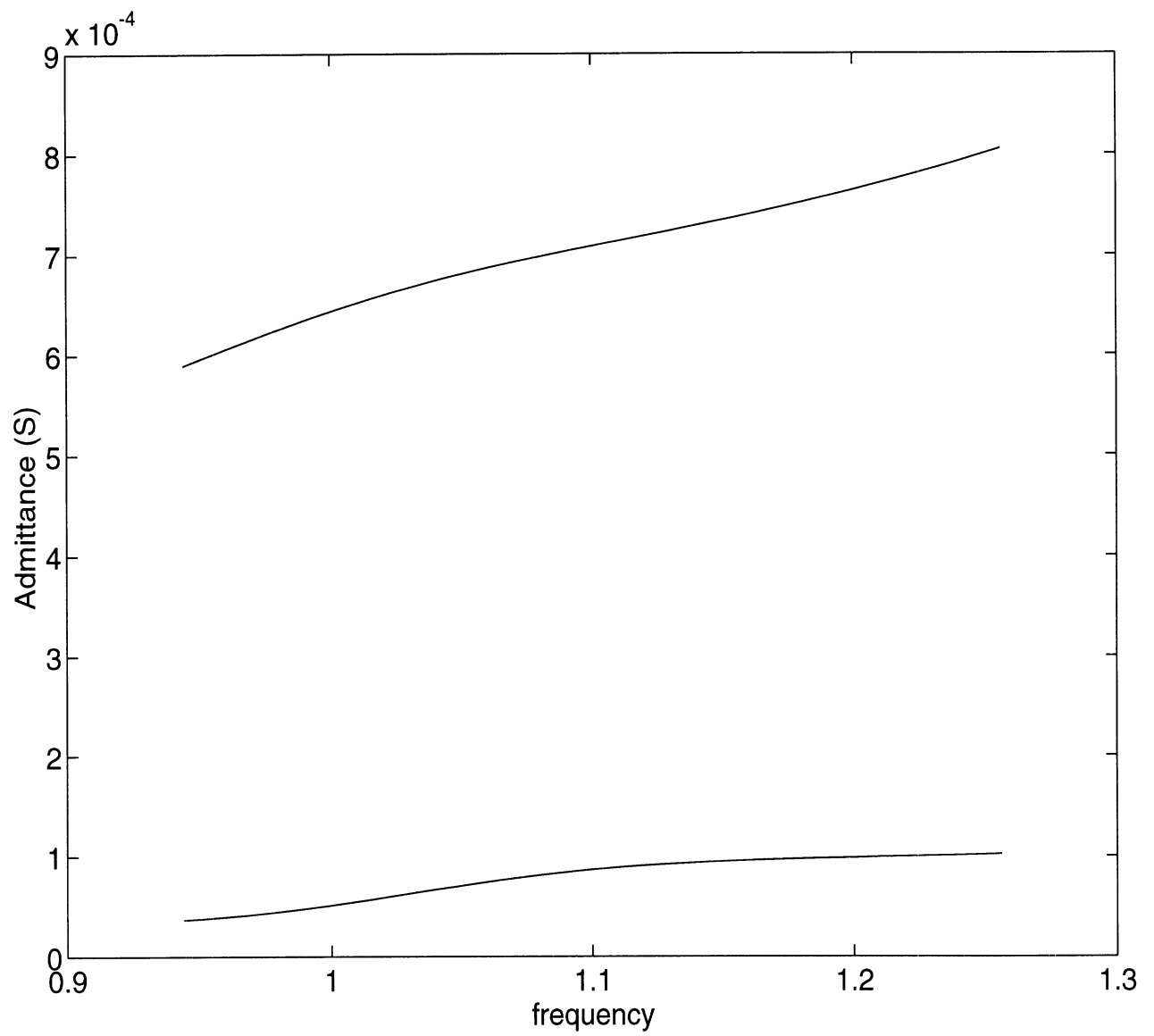
Figure 10: Admittance vs frequency for the spiral antenna in figure 1.

Design Considerations for an Archimedean Slot Spiral Antenna

Michael W. Nurnberger and John L. Volakis

Radiation Laboratory
Department of Electrical Engineering
and Computer Science
The University of Michigan
Ann Arbor, MI 48109-2122

January 12, 1995

Design Considerations for an Archimedean Slot Spiral Antenna

1 Design Goals

Develop a 118–157 MHz, vertically polarized, low-profile (or conformal) antenna as a replacement for VHF AM blade antennas on aircraft. This design is to be arrived at by scaling the dimensions of an antenna designed for a center frequency of 1.1 GHz. The design prior to scaling may have the following maximum dimensions: Diameter < 3.70" and Thickness < 0.50". The suggested/required antenna type is a 4-arm spiral antenna.

2 Initial Comments

Although a 4-arm spiral design was originally suggested, a 2-arm spiral may also be used, as both mode-1 and mode-2 (sum and difference) radiation patterns aren't required. While a 4-arm spiral can easily be designed should both sum and difference patterns be required, the 2-arm design will provide the required sum pattern and simplify the design problem somewhat—only one feed is required, and the feed area geometry is more straightforward. Polarization requirements dictate that a slot spiral be used, as opposed to a wire spiral.

3 Potential Antenna Designs

Two similar radiating structures were considered. The first is the standard archimedean spiral antenna, as shown in Figure 1a. The second is a hollow archimedean spiral antenna—essentially a standard archimedean spiral with the inner portion removed, depicted in Figure 1b. The design shown in Figure 1a is known to work, while the modification shown in Figure 1b offers the potential of an integrated feed network and a fully planar design. This will be discussed in more depth in a later section.

22

4 Potential Feed Designs

As mentioned above, two different antenna structures were investigated. Geometrically, they are quite similar, but they allow two fundamentally different feed designs.

The first class of feeds make use of the standard archimedean spiral geometry shown in Figure 1a. While the combination of this antenna and these feeds extends the bandwidth of the system beyond that indicated in the original specification, it also allows the use of standard spiral antenna design and feeding techniques.

Several standard feeding techniques exist for spiral antennas. One common method uses a balanced two-conductor transmission line, connected on the underside of the antenna, across the slot at the center of the spiral [2,8]. Another is the so-called "infinite-balun" coaxial feed, where a coaxial cable spirals in toward the center of the spiral along the underside of one of the metallic arms, and is connected across the slot at the antenna's center. Frequently a dummy cable is added along the underside of the other metallic arm, to keep the structure symmetric and the impedance consistent [1,3,8].

The "infinite balun" feed has the advantage over the balanced two-wire feed for simple structures - the balun is inherent in the feed design, is as broad-band as the antenna, and is simple to build. More complex systems, such as multi-mode direction-finding systems, etc., often use some variation of the balanced twin-wire feed, where the balun can be integrated into other parts of the system, such as the beamforming circuitry [8]. When accuracy is not as important, the balun may also be placed inside the absorbing cavity [4].

The second type of feed, shown in Figure 2, makes use of the unused area in the middle of the hollow spiral shown in Figure 1b by placing the balun structure there. Essentially, a coaxial line is brought up through the cavity, as the balanced twin-wire line would be for the first feed, and transitions to a co-planar waveguide (cpw) transmission line on the top of the substrate. This cpw line tees, and the two resulting cpw lines are then converted to slotlines through balanced cpw-slotline transitions [5,6], and become the radiating arms of the slot spiral.

5 Discussion of New Antenna and Feed Designs

- Coax-cpw-slotline Feed

  As mentioned in the above description, this feed, pictured in Figure 2, makes use of two cpw-to-slotline transitions, which also act as baluns. These transitions are fed by a coax-to-cpw transition, allowing a single coaxial feed. Initially, not much consideration was given to the overall size of each of the baluns. It was expected that, although little room would be available, the feed could be made to fit, especially given that it could be rearranged so that only one cpw-slotline transition was needed. In fact, by using radial stubs and at the cost of some deformation, one balun structure could be made to fit. However, as will be discussed later, because the radiation region of the spiral was wider than anticipated, several extra turns needed to be added to the spiral's center. This greatly reduced the amount of space available at the center of the hollow spiral, making this implementation of an integrated planar feed impractical.

- Balanced Twin-wire Feed

  The actual implementation of the balanced twin-wire feed is quite straightforward; some complexities exist, but techniques exist to overcome them [8]. On the other hand, the design and integration of the balun required to convert from the unbalanced coaxial line to the required balanced twin-wire line is more complex. Several balun designs have been documented [4,8], but they either require a deeper cavity than allowed by the design specifications, or a relatively large external circuit. Hence, while the feed itself would work quite well, the idea was put aside until a more reasonable balun structure could be developed or acquired.

- "Infinite-Balun" Feed

  Initially, because of size constraints, there was no obvious way to implement this feed. The spiral arms are quite narrow, making it difficult to attach the coaxial lines to them without changing the driving-point impedance of the antenna significantly. To circumvent these problems, a slight modification was proposed, which amounted to replacing the

coaxial line with a microstrip line (this technique was later found in [10]). Because the width of a constant impedance microstrip line is determined by the substrate thickness, an "infinite-balun" feed can be designed that has very little effect on the overall input impedance of the spiral antenna by choosing the appropriate substrate.

Having decided to use the microstrip "infinite-balun" feed, there was some concern about the amount of coupling between the microstrip transmission line and the radiating slots (the microstrip line runs relatively close to the slots). However, by again choosing the appropriate substrate, an optimum design can be found which minimizes both the microstrip losses and the microstrip-slotline coupling. This is discussed further in a later section.

For the microstrip implementation, there are two possible methods of exciting the slot at the antenna's center. The first is similar to the method used with the coaxial "infinite-balun" feed—the microstrip is shorted to the opposite side of the slot, thus creating a current maximum at the slot and maximizing the magnetic field coupling between the microstrip and the slotline. This may be done with either a plated-through hole (via), or by cutting a slit, pulling the microstrip through, and soldering it to the other side, as shown in Figures 3a and 3b, respectively.

The second method uses a $\lambda/4$-long open-circuited stub, as shown in Figure 3c. The microstrip spirals inward towards the center of antenna as usual, crosses the slot, and terminates in an open-circuit approximately one-quarter of a center-frequency guide-wavelength away. It seems clear that each technique has its advantages and disadvantages. While the first will more accurately give a short circuit, and possibly better coupling and a better match, the via holes make it harder to fabricate. On the other hand, the second technique is considerably easier to build, but may not couple as well to the slot or give as good an impedance match. Moreover, it is relatively narrow band. For our design, since the bandwidth specification is quite narrow, the $\lambda/4$-long open-circuit feed will be used.

25

6 Spiral Antenna Structure

There are many radiating structures that are "frequency-independent." In fact, any antenna that obeys the "angle principle," as defined by Rumsy [7], will be frequency independent. However, to fit this criterion, most antenna structures also require infinite size. Clearly, a practical "frequency-independent" antenna must also obey the "truncation principle" [7], which states both that the current on the radiating structure must approach zero with distance away from the feed, and that, in addition, the radiation pattern of the structure approaches a limiting form with increasing frequency. Defining the "active region" of the antenna as the area where the amplitude of the current diminishes rapidly due to radiation allows the "truncation principle" to be restated in a more useful way. It is seen to imply that the current on the antenna must greatly diminish in amplitude soon after it has passed the active region, so that the truncation of the antenna will not disturb it. Several well-known antennas obey these principles, notably the equiangular spiral and the various forms of the log-periodic antenna. However, the archimedean spiral does not. It is interesting to note that it also doesn't follow the "angle-principle," and hence is not a true frequency-independent antenna, even though it appears so in practice.

To truncate the archimedean spiral, even far beyond its active region, some sort of termination must be applied at the truncation point to minimize the reflections due to the abrupt change in impedance. To accomplish this, some idea of the size and position of the active region must be established so that the truncation is not applied too close, and the efficiency of the antenna reduced. An approximate method for determining the location and dimension of the active region is suggested in [8], and used to great effect in this study. Instead of plotting the current on the spiral arms, however, the field in the slot arms is plotted. Actually, a quantized version of the phase of the slot fields is plotted. In the plots shown in Figures 4 and 5a-c, the black lines indicate the phase ϕ s.t. $0° \leq \phi < 180°$, and the grey lines indicate the phase s.t. $180° \leq \phi < 360°$. The active region can be easily identified by locating the areas where there are more that one or two lines of the same shade adjacent to one another. Figure 4 shows the fields in the spiral slots for the hollow spiral design. Comparison with Figure 5b, which shows an example of the standard spiral design, demonstrates the usefulness of this technique. It is readily seen that the active region for the spiral antenna at this frequency (the center frequency of the antenna) extends inward further

than do the slots in the hollow spiral design. Figures 5a-c show the same plots for the standard spiral design. Figure 5a shows the fields at the low frequency limit of 955 MHz, Figure 5b at the center frequency of 1100 MHz, and Figure 5c at the high frequency limit of 1247 MHz. These frequency limits were determined by keeping the bandwidth constant throughout the scaling procedure mentioned at the beginning of this report. It is interesting to verify that the active region moves away from the center as the frequency decreases.

From the the figures discussed above, it is apparent that the hollow spiral design needs to be extended significantly inward towards the center, to accomodate the rest of the active region. However, this greatly reduces the hollow area in the center of the antenna, making it impossible to use the coax-cpw-slotline feed in its present form. For this reason, the hollow spiral design was set aside.

Having determined the size and location of the active region, the termination of the antenna can now be discussed. A good termination is critical to the operation of a spiral antenna because, if poorly executed, it is the greatest contributor to increased axial ratio. While experiment has shown that the spiral arms can be truncated inside the active region [8], it has also shown that this requires very accurate terminations, and that a reduction in gain and pattern performance is to be expected. Although termination outside the active region is not as demanding, many of the same methods are used because they are simple and work well. Most of these involve the tapered application of a lossy material such as absorber foam or resistive paint to the spiral arms or slots. These can either be specially applied, or can be made of the foam in the absorbing cavity. There are many examples of these sorts of terminations in the literature [2,8,9]. For the antenna in question, a tapered application of lossy foam below the antenna will be used, as shown in Figure 6, because a cavity will not be used initially.

Having qualified the fundamental issues involved in designing a spiral antenna, the actual dimensions can now be determined. The number of turns, the growth rate, the width of the slotline and of the microstrip feedline, and to a lesser extent, the overall diameter of the antenna, are all inter-related. The driving issue of the design eventually becomes the feed structure. The allowable amount of coupling between the microstrip line and the slotline and the thickness of the substrate effectively combine to determine the minimum allowable growth rate for the spiral. The thinner the substrate, the closer together the spiral slots can be for a given amount of coupling with the

microstrip feedline, and the smaller the growth rate can be, yielding a higher performance antenna. Eventually this is limited by construction feasibility issues. The width of the slotline also affects the choice of the growth rate, but to a much lesser extent. The characteristic impedance of a wide slotline on a thin subtrate (slot width $\gg$ substrate thickness) is virtually independent of the slotline width, allowing a wide range of choices. The number of turns is basically determined by the growth rate of the spiral, and the required operating bandwidth, as is the outer diameter of the antenna.

For this antenna, the following parameters give a good compromise between microstrip loss and coupling, as discussed above. For a dielectric thickness of 18 mils, the 50 Ω microstrip feedline is 32 mils wide, and the 100 Ω slotline is 44 mils wide. The growth rate was chosen to be $a = .166$, which spaces the slotlines 205 mils apart, center-to-center. Figures 5a-c were generated using these values, and indicate that approximately 7 turns are required to adequately cover the required frequency band and allow for a good termination.

7 Experimental Results

A spiral slot antenna was constructed according to the dimensions mentioned in the preceding section, and both the input impedance and pattern characteristics were measured.

Figure 7 shows the reflection coefficient of the antenna, measured at the antenna's connector, between 500 MHz and 5.0 GHz. For the frequency range of interest (950 to 1250 MHz), the reflection coefficient is approximately -17.5 dB, corresponding to a VSWR of 1.31. Contrary to the above discussion, the $\lambda/4$-long tuning stub does not seem to restrict the bandwidth of the antenna significantly. An investigation of this effect is currently underway.

The radiation patterns were measured for five different antenna configurations:

1. The antenna, with no modifications.

2. The antenna, with a ring of absorbing material placed on the slot side to terminate the slots, as discussed above. The ring was made of Eccosorb LS-26, 0.125" thick, with I.D. = 5.625" and O.D. = 9.00". The ring of

28

absorber was held against the antenna with a ring of thin cardboard, and fastened with eight nylon screws around its periphery.

3. The antenna, with another absorber ring inside the first. The second ring was made of the same thickness material, with I.D. = 5.375", and O.D. = 5.625".

4. The antenna, with the inner absorber ring removed, and a second ring, with the same dimensions as the first, placed on top of the first. Both rings were held on with the same structure used in configuration 2.

5. The antenna, with both layers of absorber, and a ground plane placed on top of the absorber rings. All three layers were held on with the same structure as above.

Patterns taken at the center of the frequency band of interest (1100 MHz) for each of the five modifications mentioned above are shown in Figures 8a-e, respectively.

To determine the axial ratio of the radiation pattern, and thus the antenna's ability to recieve or radiate circularly polarized fields, a rotating source antenna is usually used. This allows the polarization of the incident field to be changed rapidly compared to the azimuthal rotation of the antenna-under-test. As the antenna-under-test rotates in azimuth, the variation of the received level then indicates the dependence of the gain on the incoming field polarization at every azimuth angle, from which the axial ratio can be derived.

Unfortunately, the facility where the radiation patterns in Figures 8a-e were measured is not equipped with a rotating source antenna, making this technique difficult at best. To give some idea of the axial ratio however, the following scheme was used. At boresight, the source antenna was first rotated to maximize the signal received by the antenna-under-test, and an azimuthal pattern taken. Then, again at boresight, the source antenna was oriented to minimize the received signal, and another azimuthal pattern taken. The main disadvantage of this technique is that it only gives the true axial ratio at boresight—the axial ratio at all other angles is only an optimistic estimate of the true axial ratio. For the patterns in Figures 8a-e, boresight is at 0°, and the two patterns are a result of the maximization and minimization of the received signal, as discussed above.

The radiation patterns for the unmodified antenna are shown in Figure 8a. At boresight, the axial ratio is approximately 6 dB, and at 180°, the axial ratio appears to be very close to zero. However, because the source polarization wasn't calibrated with the antenna-under-test at this orientation, this is an optimistic estimate at best. An investigation of the axial ratio around 180° is currently underway.

To reduce the axial ratio, as discussed above, a ring of absorber was used to create a tapered termination for the spiral slots. The radiation patterns resulting from this modification are shown in Figure 8b. The benefits of this modification, insofar as indicated by these patterns, are somewhat nebulous. The axial ratio at boresight did not improve, and the axial ratio at 180° appears to have deteriorated significantly. However, both the front-to-back and side-to-side symmetry of the patterns have greatly improved, and the location of the nulls is more realistic. In spite of the seeming decrease in pattern quality, these improvements to the symmetry give some credibility to the modification.

In an effort to improve the axial ratio, another ring of absorber was added inside the first, as discussed above. If the slots weren't adequately terminated previously, this should have improved matters, reducing the axial ratio somewhat. However, as shown in Figure 8c, the axial ratio increased noticeably, and extreme pattern asymmetry resulted. While a better termination would not have these effects, an improperly terminated slot would reflect energy back along the slots, and cause similar problems. On examination of the second ring of absorber, a jagged edge was discovered (much rougher than that of the first ring). This would seem to bear out the necessity of a very precise termination, as discussed above.

Still working under the assumption that the termination was not functioning adequately, the inner absorber ring was removed, and another ring of absorber placed on top of the first. The resulting pattern, shown in Figure 8d, is virtually identical to the pattern in Figure 8b. This result would seem to indicate that, in fact, the slot termination was functioning properly, and that some other source must be responsible for the poor axial ratio. Further discussion of this follows in the next section.

Accepting for the moment the poor axial ratio, a ground plane was placed behind the slot spiral to verify its unidirection operation. Figure 8e shows the resulting pattern. The axial ratio improved somewhat, and the rear radiation levels were reduced to an acceptable level. However, the overall gain of the antenna decreased by approximately 4 dB. Increasing the frequency,

however, verified that the ground plane had been placed too close to the slots, and had shorted some of the field in the slot. At 1500 and 2000 MHz, instead of decreasing the gain by 4 dB, the ground plane increased the gain by approximately 1.5 dB over the antenna without the ground plane.

8   Future Work

As discussed above, the poor axial ratio doesn't seem to be a result of the reflections an improper slot termination would create. Based on the patterns shown in Figures 8a-e and on the fundamental geometrical symmetry of the antenna, another possible source of the high axial ratio is radiation from the microstrip feedline. The feedline's radiation would have the opposite circular polarization as the spiral slots, greatly increasing the overall axial ratio. Feedline radiation would also cause a front-to-back asymmetry in the radiation patterns, as the microstrip would have a greater effect on the front of the antenna that on the back. As the ground plane behind the microstrip line is rather narrow, this mechanism seems rather likely.

To eliminate this possibility, another antenna is currently being fabricated on a thinner substrate. This will not only place the microstrip line closer to the groundplane, but also make it narrower. Both of these modifications should serve to reduce the feedline radiation, and help to reduce the overall observed axial ratio of the antenna.

Further investigation of the $\lambda/4$-long tuning stub are also underway, with the dual goals of determining the actual workings of the feed and developing a narrow-band feed for application to this antenna.

References

1. J.D. Dyson, "The Equiangular Spiral Antenna," *IRE Trans. Antennas Propagat.*, Vol AP-7, Apr 1959, pp. 181-187.

2. J.A. Kaiser, "The Archimedean Two-Wire Spiral Antenna," *IEEE Trans. Antennas Propagat.*, Vol AP-8, No. 3, May 1960, pp. 312-323.

3. J.D. Dyson, "The Unidirectional Equiangular Spiral Antenna," *IRE Trans. Antennas Propagat.*, Vol AP-7, Oct 1959, pp. 329-334.

4. R. Bawer, J. Wolfe, "A Printed Circuit Balun for Use with Spiral Antennas," *IEEE Trans. Microwave Theory Tech.*, Vol. MTT-8, May 1960, pp. 319-325.

5. G. Oltman, "The Compensated Balun," *IEEE Trans. Microwave Theory Tech.*, Vol. MTT-14, No. 3, Mar 1966, pp. 112-119.

6. W. Grammer, K.S. Yngvesson, "Coplanar Waveguide Transitions to Slotline: Design and Microprobe Characterization," *IEEE Trans. Microwave Theory Tech.*, Vol. MTT-41, No. 9, Sept. 1993, pp. 1653-1658.

7. V.H. Rumsey,"Frequency Independent Antennas," Academic Press, New York, 1966.

8. R.G. Corzine, J.A. Mosko,"Four-Arm Spiral Antennas," Artech House, 1990.

9. J. Reese, "Terminator for Spiral Antenna," U.S. Patent 3,787,871, Jan 22, 1974.

10. R.G. Corzine, J.A. Mosko, "Integrated Spiral Antenna and Printed Circuit Balun," U.S. Patent 4,525,720, Jun 25, 1985.
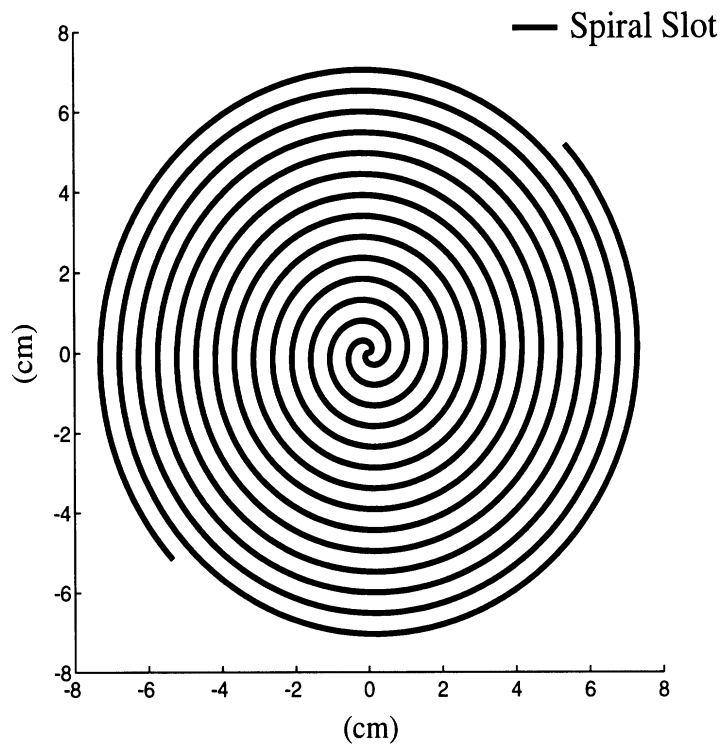
Figure 1a. Standard Archimedean Spiral Antenna
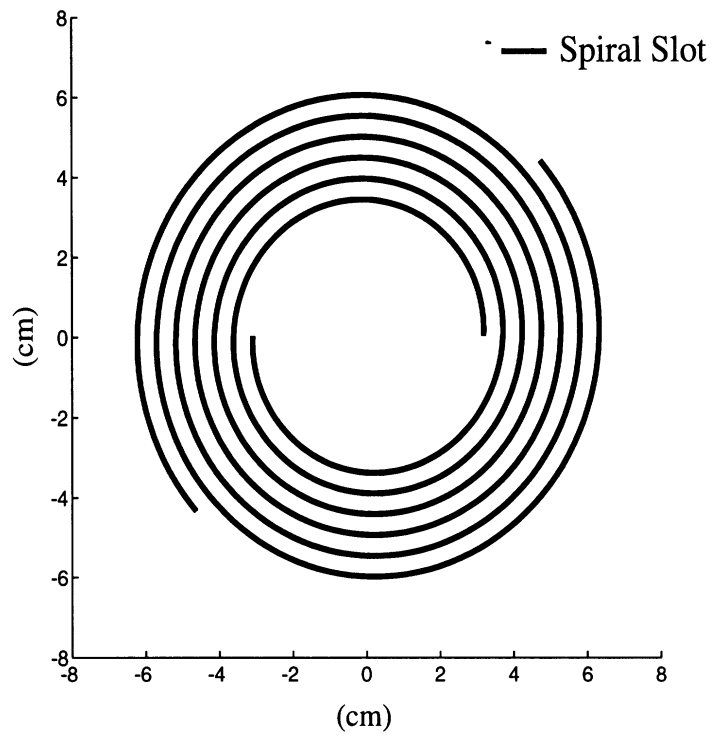
Figure 1b. Hollow Archimedean Spiral Antenna

33
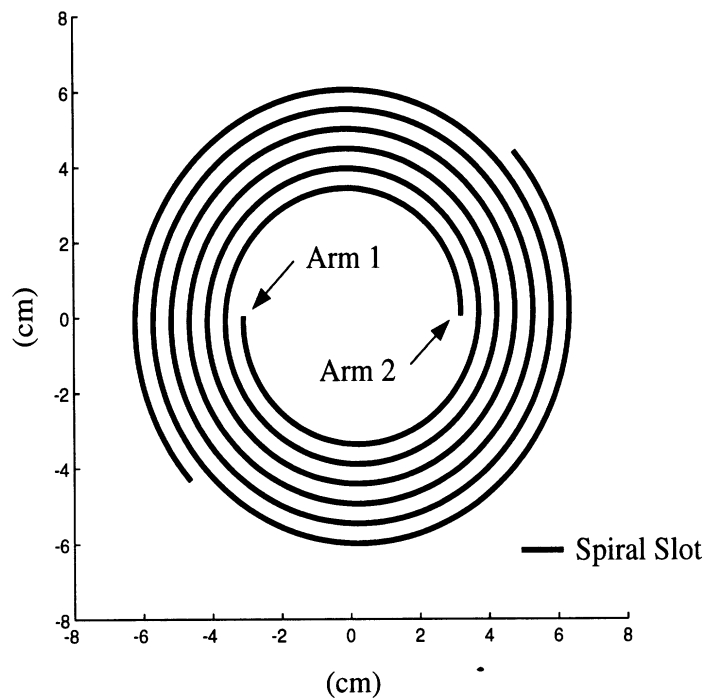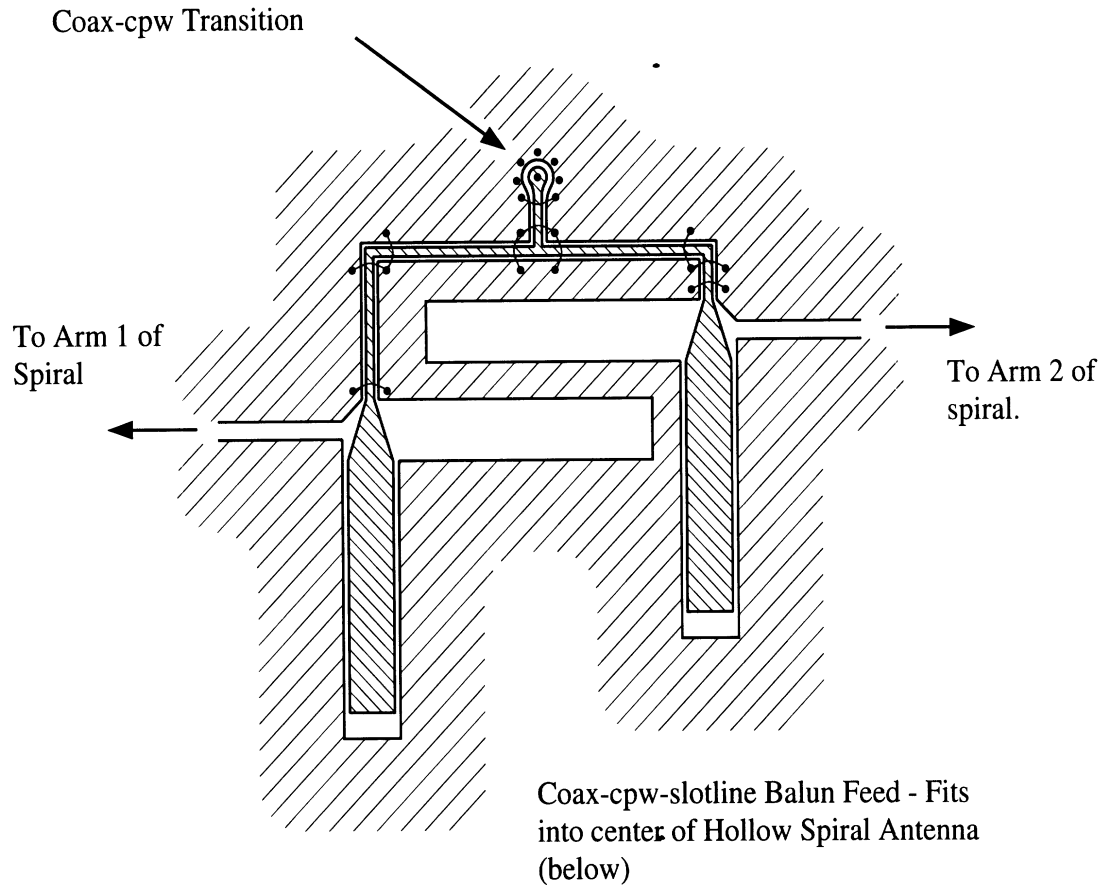
Figure 2. Coax-cpw-slotline Balun Feed with
Hollow Archimedean Spiral Antenna
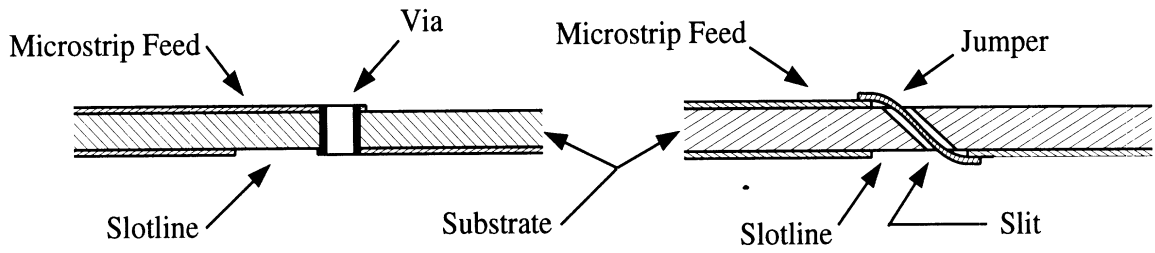
Figure 3a. Microstrip "Infinite Balun" Feed with Short-Circuit Via.

Figure 3b. Microstrip "Infinite Balun" Feed with Short-Circuit Slit.

——— Slotline   - - - - Microstrip "Infinite Balun" Feed
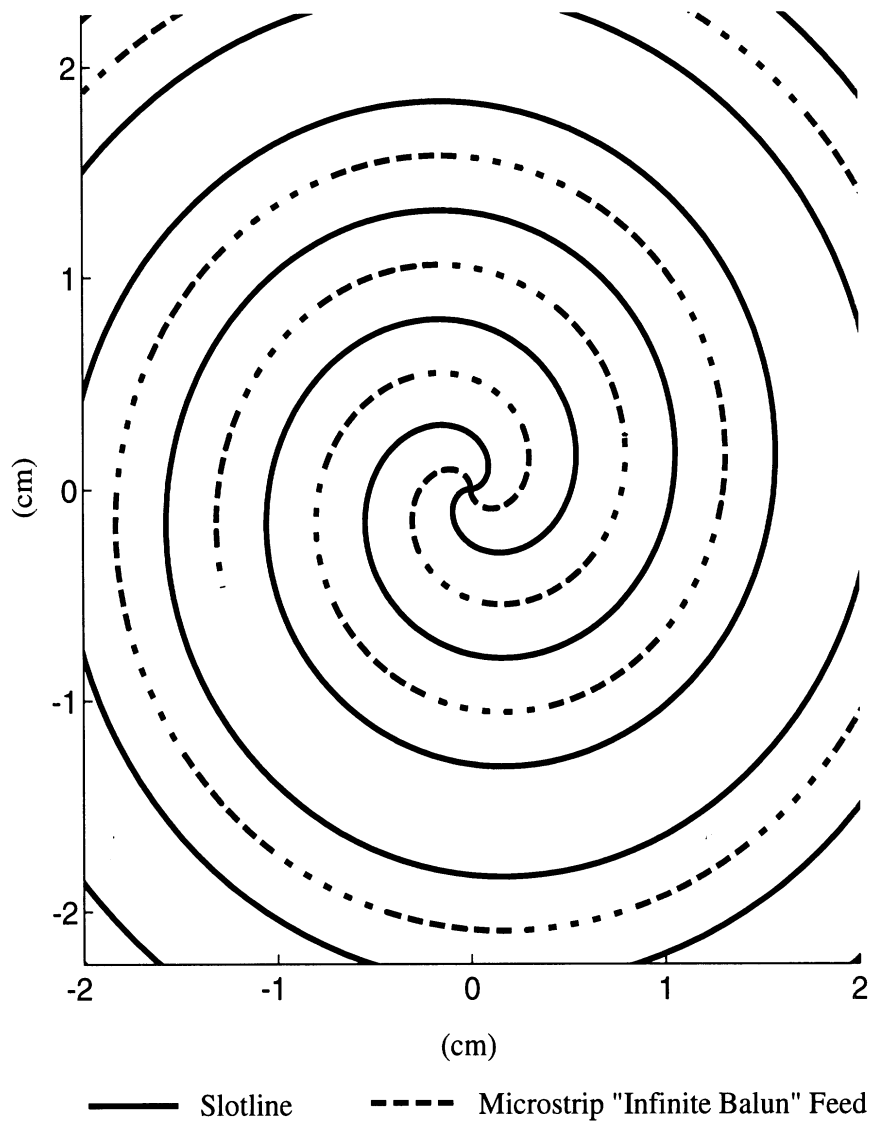
Figure 3c. Microstrip "Infinite Balun" Feed with $\lambda_g/4$ Open-Circuit Stub.
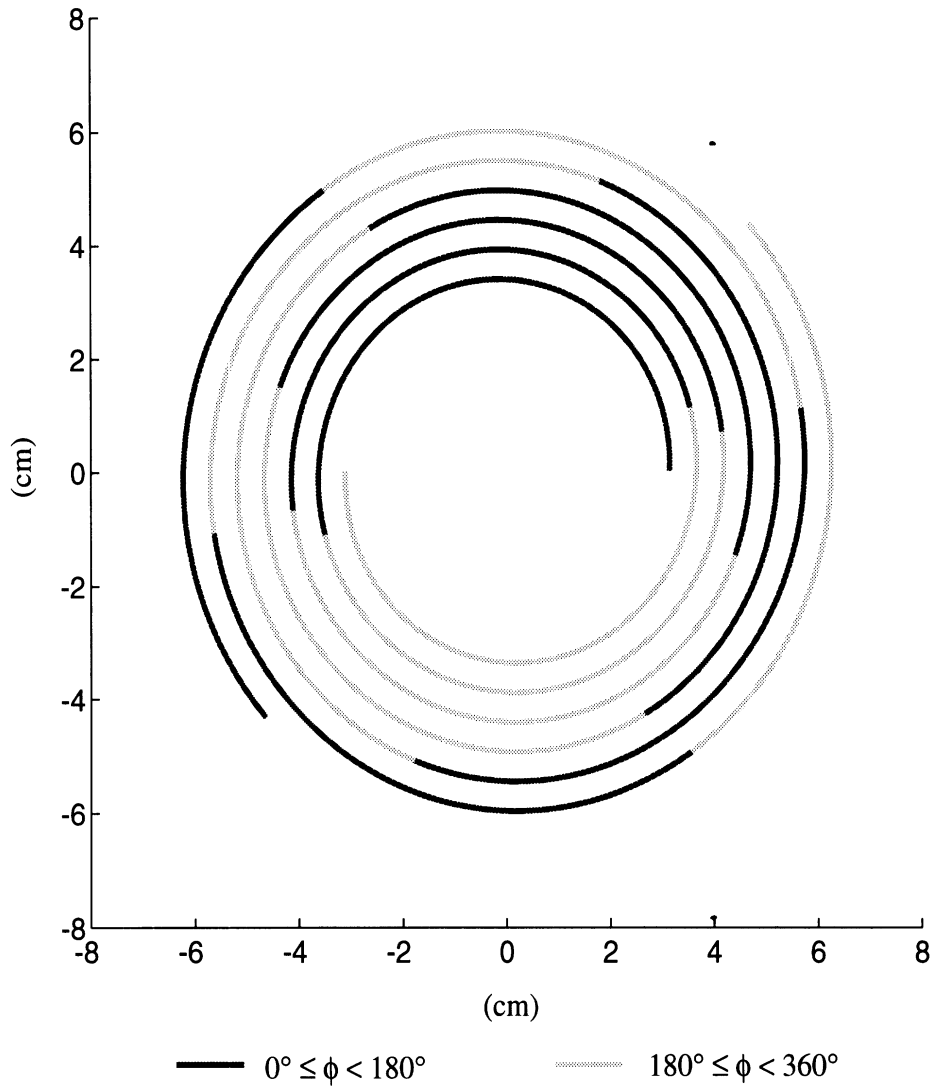
Figure 4. Quantized Phase (φ) in Hollow
Archimedean Spiral Antenna
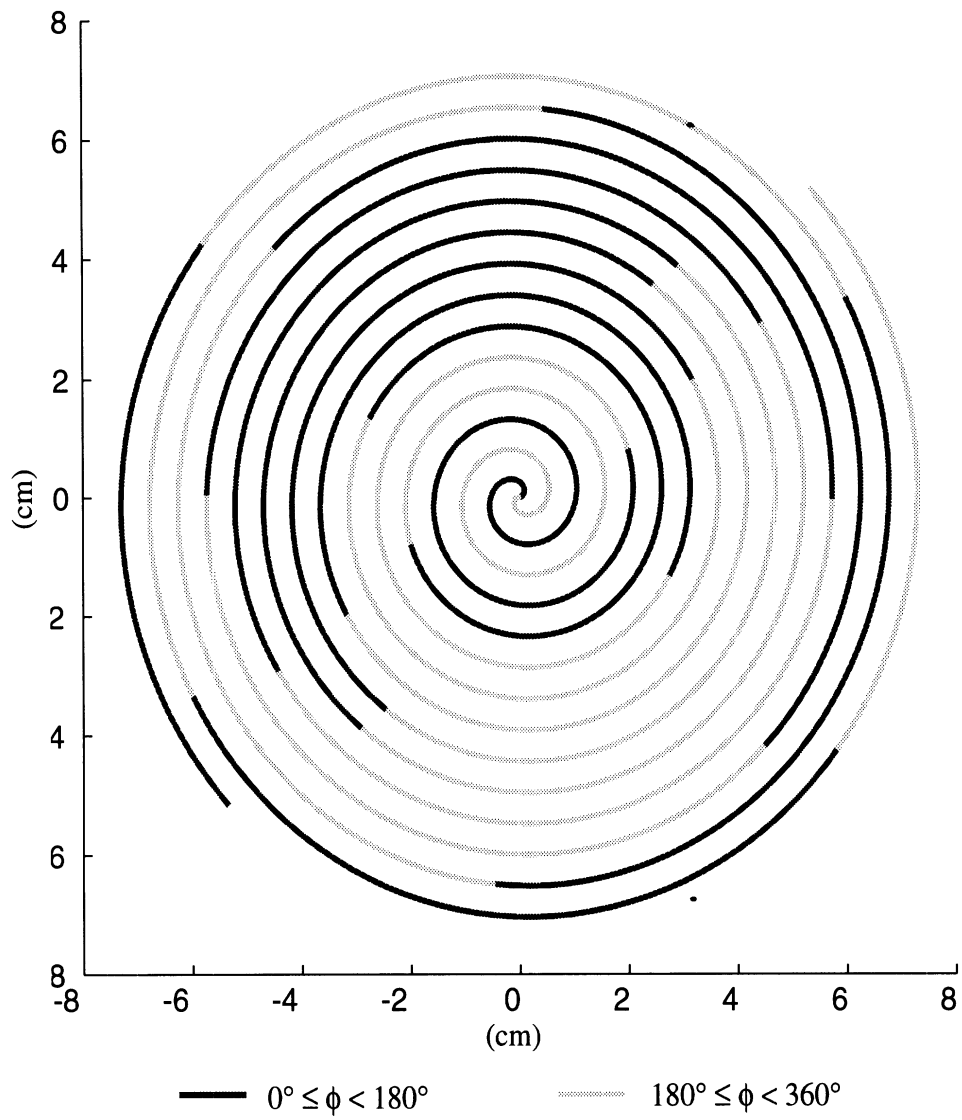
Figure 5a. Quantized Phase (ϕ) at f = 955 MHz for
Standard Archimedean Spiral Antenna
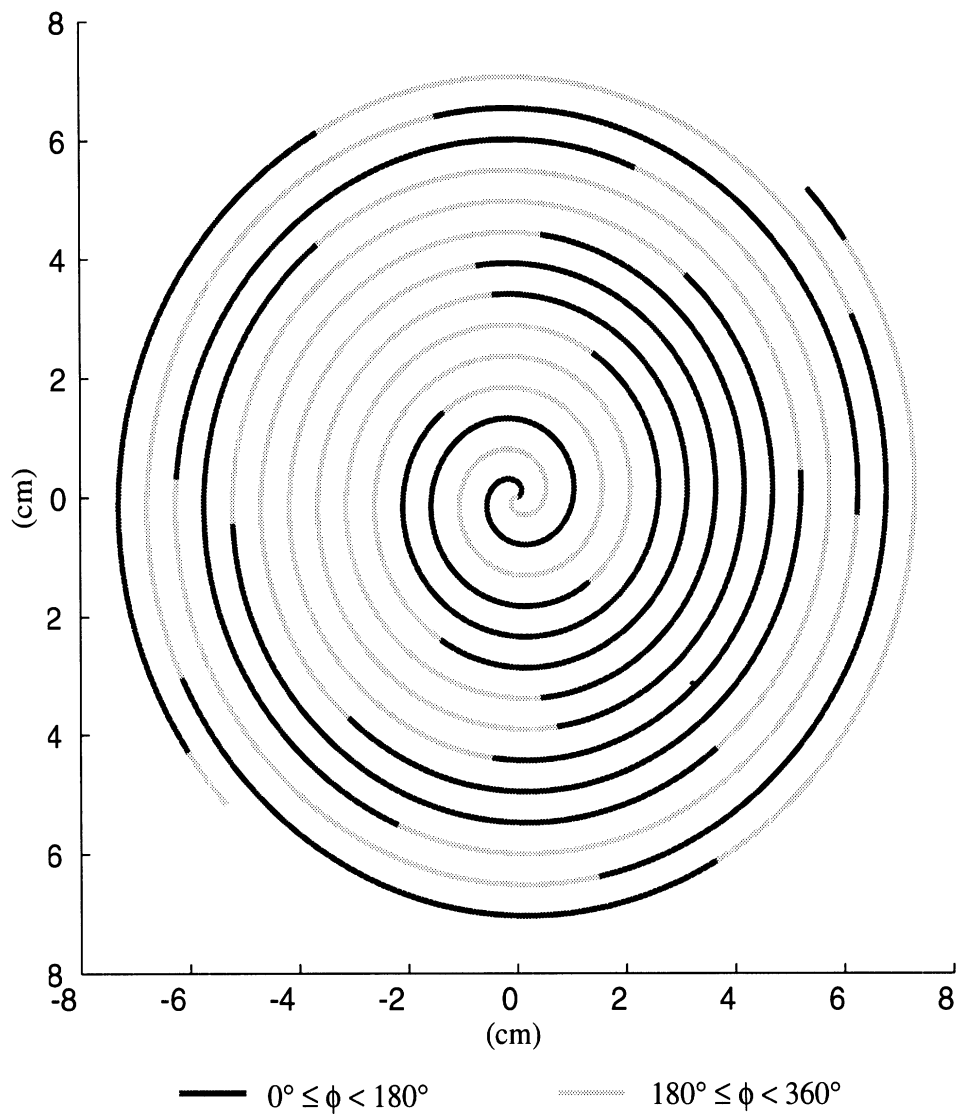
Figure 5b. Quantized Phase (ϕ) at f = 1100 MHz for
Standard Archimedean Spiral Antenna
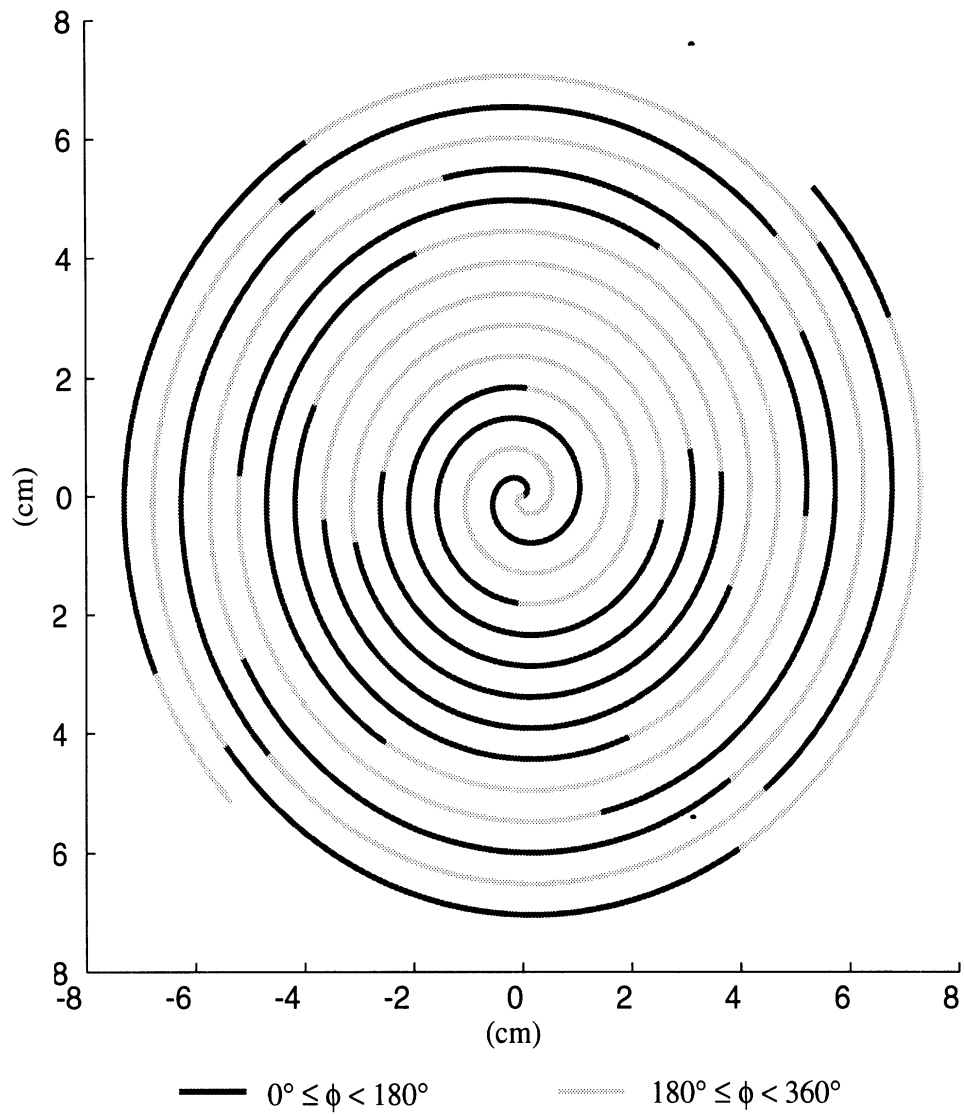
Figure 5c. Quantized Phase (ϕ) at f = 1247 MHz for
Standard Archimedean Spiral Antenna
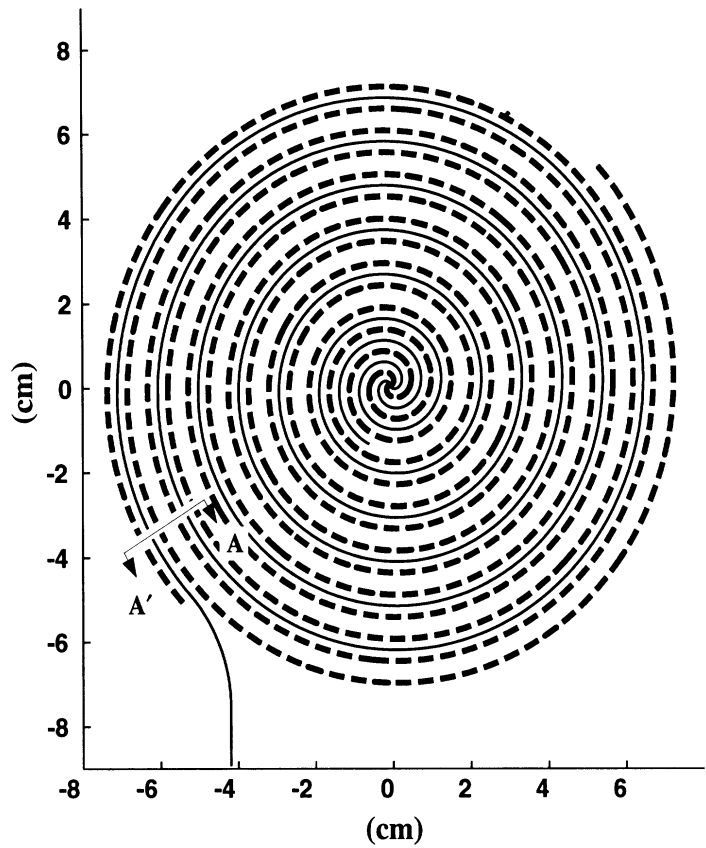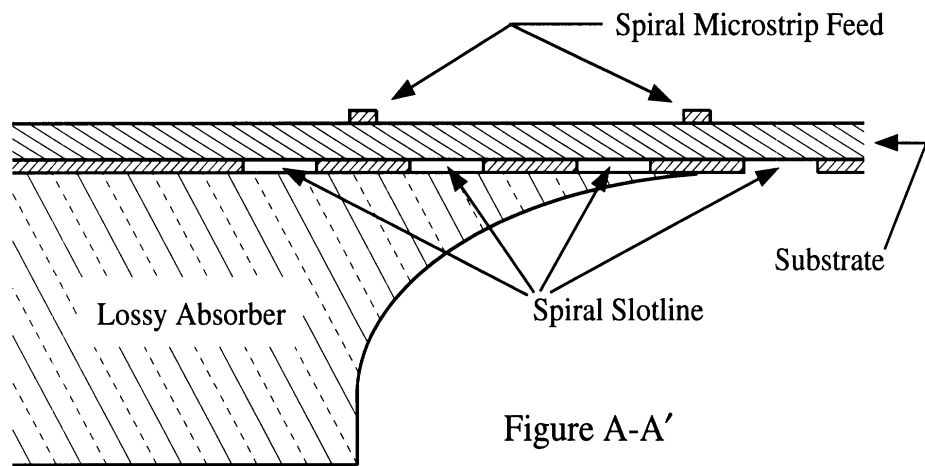
Figure 6. Tapered Lossy Foam Absorber for
Spiral Arm Truncation

1.1000 GHz

Cor   SCALE
  0   5 dB/div

Smo

START   .5000 GHz   STOP 5.0200 GHz
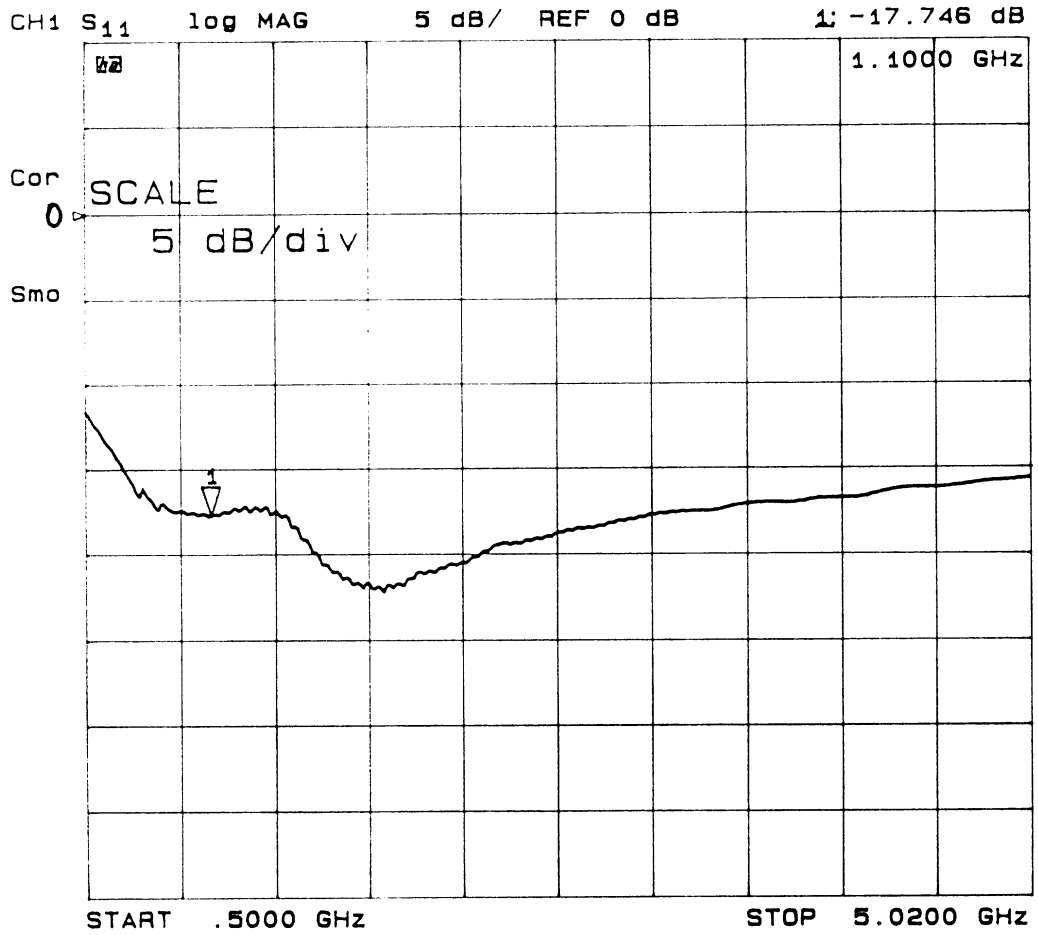
Figure 7. S11 of Unmodified Spiral Antenna
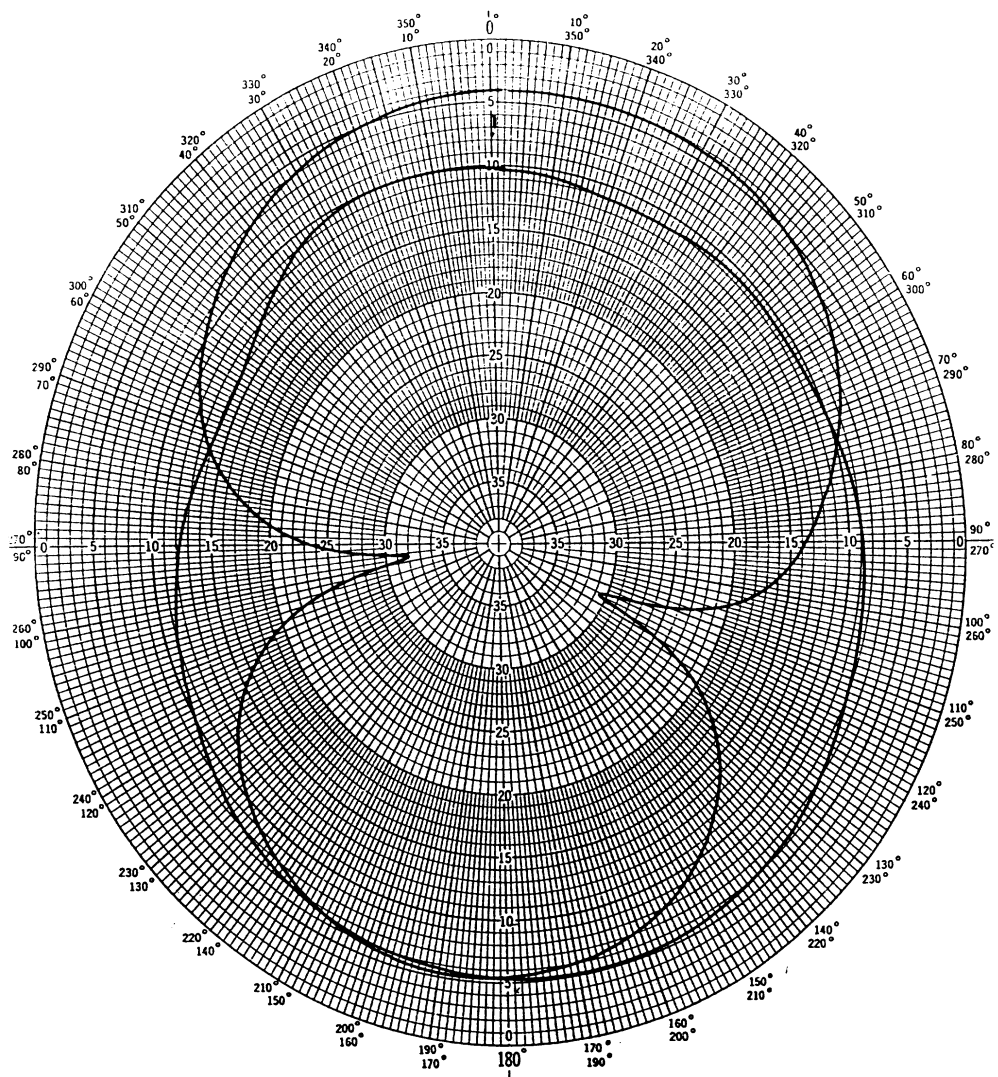
**Figure 8a. Azimuth Pattern of Unmodified
Spiral Antenna**

42
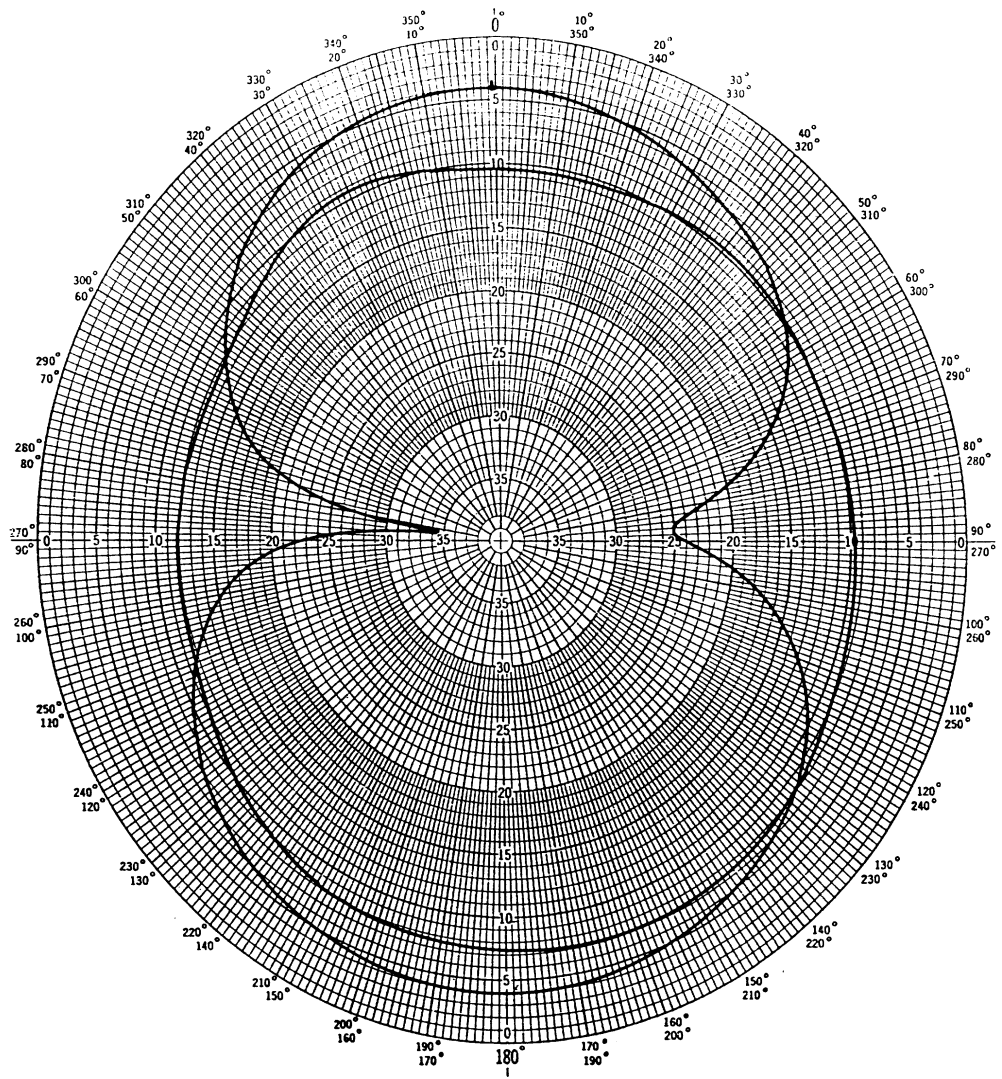
Figure 8b. Azimuth Pattern of Spiral with Absorber Ring

43
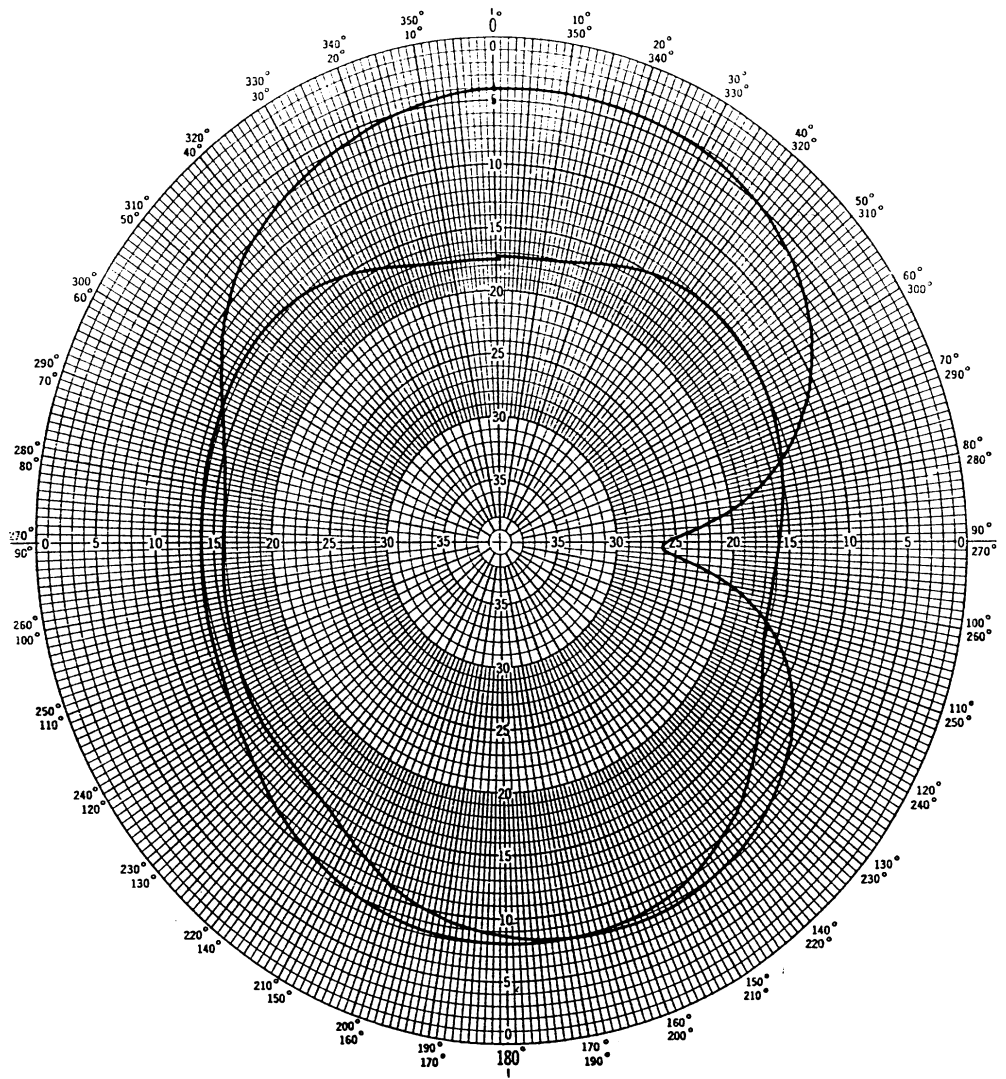
Figure 8c. Azimuth Pattern of Spiral with Inner Absorber Ring
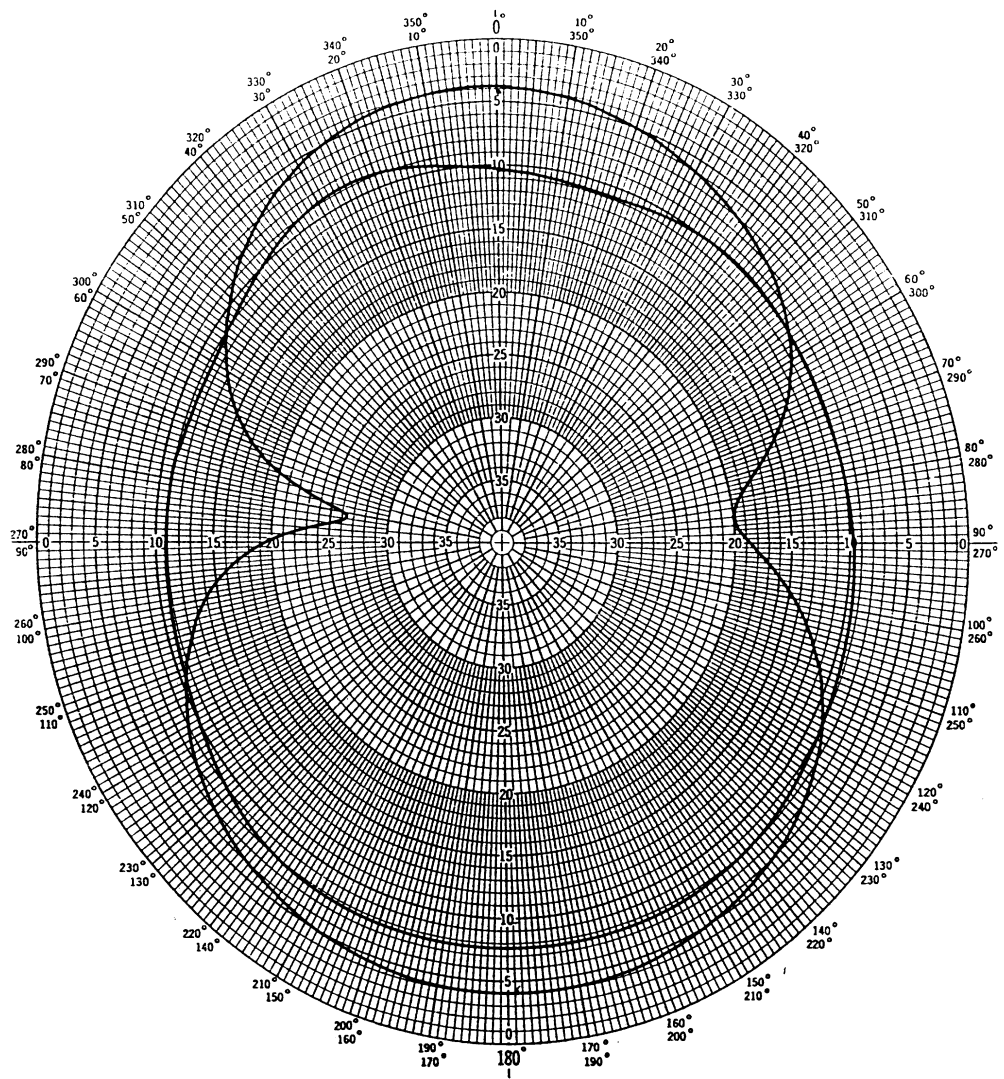
**Figure 8d. Azimuth Pattern of Spiral with
Double-Thickness Absorber Ring**

45
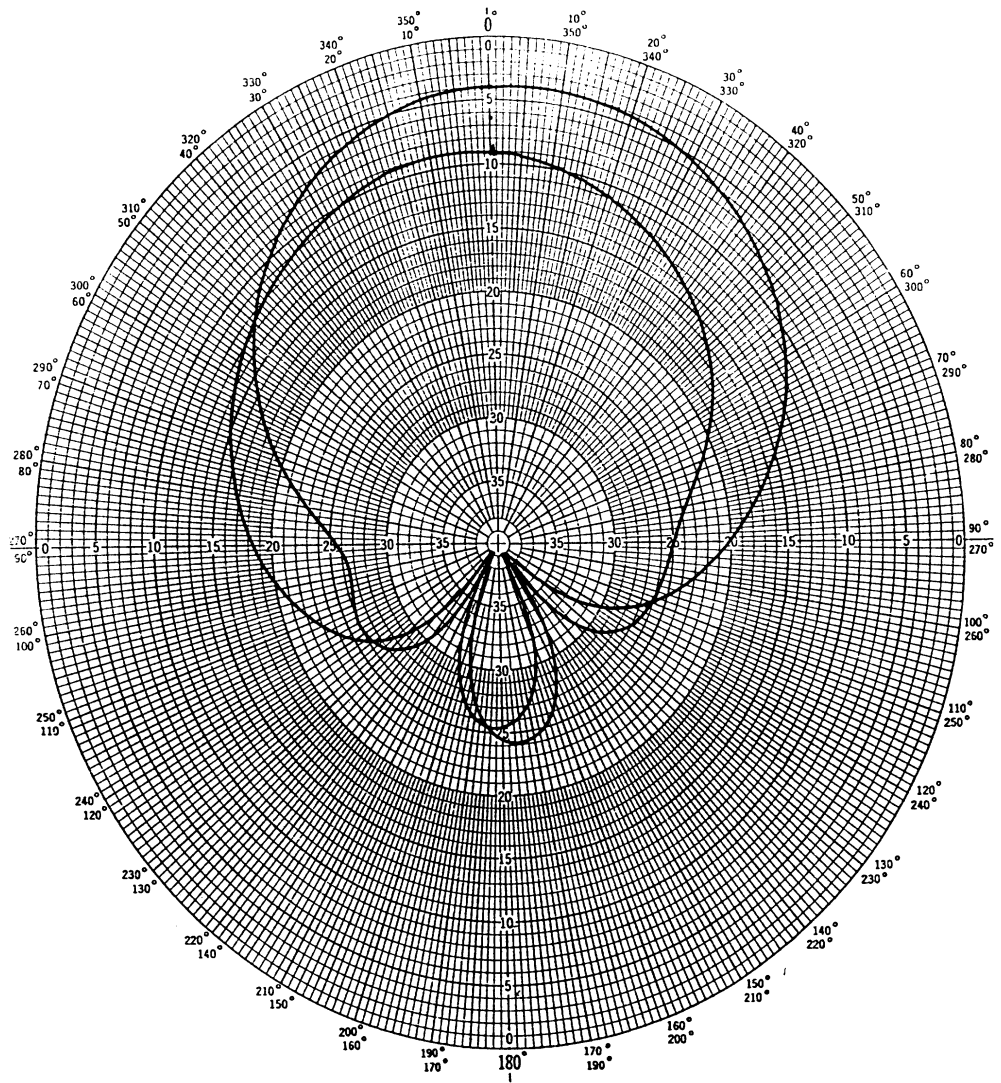
**Figure 8e. Azimuth Pattern of Spiral with
Double-Thickness Absorber Ring
and Ground Plane**

46

An Efficient and Accurate Model Of The Coax Cable Feeding Structure For FEM Simulations

Jian Gong and John L. Volakis,

Radiation Laboratory
Department of Electrical Engineering
and Computer Science
The University of Michigan
Ann Arbor MI 48109-2122

Abstract

An efficient and accurate coax cable feed model is proposed for microstrip or cavity-backed patch antennas in the context of a hybrid finite element method (FEM). A TEM mode at the cavity-cable junction is assumed for the FEM truncation and system excitation. Of importance in this implementation is that the cavity unknowns are related to the model fields by enforcing an equi–potential condition rather than field continuity. This scheme proved quite accurate and may be applied to other decomposed systems as a connectivity constraint. Comparisons of our predictions with input impedance measurements are presented and demonstrate the substantially improved accuracy of the proposed model.

I. Introduction

The coax cable is widely used as a feeding structure for microstrip or cavity-backed patch antennas because of its simplicity and low spurious radiation. Indeed, abundant literature exists on the theoretical and experimental investigation of coax cable feeds [1]–[3]. Most of these papers present integral equation techniques in conjunction with the pertinent Green's functions. However, the Green's function is only available for a certain class of geometries, and this limits the application of the integral techniques to those geometry designs. Also, the formulation must be modified and recoded for different antenna configurations corresponding to Green's function variations. To avoid the complexity of the Green's function, a hybrid finite element – boundary integral approach [5] was recently proposed to simulate cavity-backed antennas of arbitrary shapes. For antenna radiation it is observed that a simple

47

probe model with a constant current along the inner conductor linking the grounded base to the antenna element is straightforward and efficient. But the probe feed is only valid for thin substrates and this is consistent with the Moment Method (MM) results. To model an electrically thick substrate, in this communication we propose a more sophisticated feed modeling scheme in the context of the finite element method (FEM) using linear edge-based tetrahedral elements. In the next section, the formulation of the entire hybrid numerical system is first described for reference purposes. The proposed feed model is then presented in section III on the basis of a TEM mode excitation. Model improvements are also discussed for the case when the TEM assumption at the cavity-cable junction does not hold. Input impedance comparisons between measurements and predictions based on this technique are presented in section IV.

II. Hybrid FE–BI System

The functional pertinent to the radiation by a cavity-backed antenna with a coax cable feed (as shown in figure 1) is given by

$$
\begin{aligned}
F(\mathbf{E}) \;=\; & \frac{1}{2} \iiint_V \left\{ (\nabla \times \mathbf{E}) \cdot \frac{1}{\mu_r}(\nabla \times \mathbf{E}) - k_0^2 \epsilon_r \mathbf{E} \cdot \mathbf{E} \right\} dv \\
& - 2k_0^2 \iint_S (\mathbf{E} \times \hat{z}) \cdot \left\{ \iint_{S'} (\mathbf{E} \times \hat{z}) \cdot \left(\bar{\mathbf{I}} + \frac{1}{k_0^2}\nabla\nabla \right) G_0(\mathbf{r},\mathbf{r}') \, dS' \right\} dS \\
& - jk_0 Z_0 \iint_C (\mathbf{E} \times \mathbf{H}) \cdot \hat{z} \, dS,
\end{aligned}
\tag{1}
$$

where V refers to the cavity volume and the surface S encompasses the cavity aperture excluding the portion occupied by the metallic antenna elements; ϵ_r and μ_r denote, respectively, the relative permittivity and permeability; k_0 is the free space wave number, Z_0 is the free space intrinsic wave impedance, $\bar{\mathbf{I}}$ is the unit dyad, and $G_0(\mathbf{r},\mathbf{r}')$ is the free space Green's function with $\mathbf{r}$ and $\mathbf{r}'$ denoting the observation and integration points; the surface C is the cross section of the coax cable at the cavity–cable junction.

Following the standard discretization procedure [5], we obtain a system of equations of the form

$$
\sum_{e=1}^{N_e} \left\{ [A_{ij}^e]\{E_j^e\} \right\} + \sum_{e \in S}^{N_S e} \left\{ [B_{ij}^e]\{E_j^e\} \right\} + \sum_{e \in C}^{N_C e} \frac{\partial F_C(\mathbf{E},\mathbf{H})}{\partial E_i} = 0,
\tag{2}
$$

where the explicit expressions for A_{ij} and B_{ij} may be found in [5] and the functional term F_C is the surface integral on C in (1). It is apparent that the system excitation is associated with the functional F_C whose evaluation is the subject of this communication.

III. Coax Cable Feed Modeling

To proceed with the evaluation of

$$
F_C = -jk_0 Z_0 \iint_C (\mathbf{E} \times \mathbf{H}) \cdot \hat{z} \, dS,
\tag{3}
$$

a boundary constraint relating $\mathbf{E}$ to $\mathbf{H}$ is needed. To this end, we assume a TEM mode on C and consequently the fields within the cavity may be expressed as (see Figure 2)

$$\mathbf{E} = \frac{I_0 Z_0}{2\pi\sqrt{\epsilon_{rc}}}(1+\Gamma)\frac{1}{r}\hat{r}, \quad \mathbf{H} = \frac{I_0}{2\pi}(1-\Gamma)\frac{1}{r}\hat{\phi}, \tag{4}$$

where ϵ_{rc} is the relative permittivity inside the coax cable; Γ denotes the reflection coefficient measured at $z = 0$ and I_0 is the given input current source at the same location. Also, (r, ϕ, z) are the polar coordinates of a point in the cable with the center at $r = 0$. To simplify the analysis, we introduce the quantities

$$e_0 = \frac{I_0 Z_0}{2\pi\sqrt{\epsilon_{rc}}}(1+\Gamma), \quad h_0 = \frac{I_0}{2\pi}(1-\Gamma). \tag{5}$$

Hence,

$$\mathbf{E} = \frac{e_0}{r}\hat{r}, \quad \mathbf{H} = \frac{h_0}{r}\hat{\phi}, \tag{6}$$

and from (5) it follows

$$h_0 = -\frac{\sqrt{\epsilon_{rc}}}{Z_0}e_0 + \frac{I_0}{\pi}, \tag{7}$$

which is the desired constraint at the cable junction in terms of the new quantities h_0 and e_0. Note that e_0 and h_0 are field coefficients as new unknowns in place of the fields $\mathbf{E}$ and $\mathbf{H}$, and it is therefore appropriate to rewrite F_C in terms of these new coefficients. To do so, we substitute (5) and (7) into (3) and upon making use of the axisymmetric field property we obtain

$$F_C = -2\pi j k_0 Z_0 e_0 h_0^{src} ln(\frac{b}{a}), \tag{8}$$

where a and b are the radii of the inner and outer cable conductors. The superscript *src* stands to indicate that h_0 is treated as a source term in the extremization of the functional.

We choose the linear edge-based tetrahedral elements to discretize the cavity and the corresponding mesh on the cross section C is shown in Figure 2(b). In this formulation, the field across the pth edge, p=1,2,..., N_C (N_C is the number of cavity mesh edges on C), is set to a constant as dictated by the linear edge-based expansion function inside the cavity. However, the cable TEM modal fields (4) behave as $1/r$ and this modeling inconsistency makes it difficult to apply the tangential field continuity condition at the cable junction (i.e. over the aperture C). To overcome these difficulties, we can relate the fields across the cable junction by recognizing that the potential difference between the inner and outer conductors must be the same as computed by the fields of the cavity or those in the cable region. Specifically, if the N_p^{th} edge of the cavity region borders and is also across the coax cable, from (4)-(6) it then follows that the appropriate equi–potential condition is

$$\Delta V = E_i(b-a) = e_0 ln\frac{b}{a}, \quad i = N_p(p = 1, 2, ..., N_C). \tag{9}$$

49

where ΔV denotes the potential difference between the inner and outer surface of the cable. This condition simply provides a relation between the constant cavity edge field and the coax cable modal field. When used into the functional F_C, it introduces the excitation into the hybrid finite element system without a need to extend the mesh inside the cable or to employ a fictitious current probe. It remains to rewrite F_C in terms of E_i, i.e. the field value of the edges bordering the cable and to do so we substitute (7) and (9) into (8). Then upon taking into account all N_C cavity mesh edges on the cable junction, we obtain

$$
F_C = -\frac{\pi}{3}jk_0Z_0(b-a)\left\{\frac{I_0}{\pi} - \frac{\sqrt{\epsilon_{rc}}}{Z_0}\frac{b-a}{ln\frac{b}{a}}E_i\right\}^{src}\sum_{i=N_p}^{N_C}E_i. \tag{10}
$$

In this expression, rather than representing the functional F_C in terms of a single edge field, we made use of the average field across the cable as computed by the totality of the equal element fields on the cable's aperture (because of the axisymmetric property, all elements fields at the cable's aperture are equal). The factor inside the curly brackets of (10), with the superscript src, functions as a source in the extremization process. Hence, the extremization of (10) yields

$$
\begin{aligned}
\frac{\partial F_C}{\partial E_i} &= -\frac{1}{3}\pi jk_0Z_0(b-a)\left\{\frac{I_0}{\pi} - \frac{\sqrt{\epsilon_{rc}}}{Z_0}\frac{b-a}{ln\frac{b}{a}}E_i\right\} \\
&= U_iE_i - V_i, \quad i = N_p(p=1,2,...N_C),
\end{aligned} \tag{11}
$$

where

$$
U_i = j\frac{1}{3}\pi k_0\sqrt{\epsilon_{rc}}\frac{(b-a)^2}{ln\frac{b}{a}} \tag{12}
$$

$$
V_i = j\frac{1}{3}k_0Z_0(b-a)I_0. \tag{13}
$$

We observe that the 'constant cavity field' along each mesh edge at the cable junction is just a fictitious field representation and its meaningful physical interpretation is governed by the equi–potential constraint (9). To proceed, we assemble the FEM system together with (11). Specifically, each U_i is added to the N_C diagonal entries of the finite element matrix which is associated with the N_C edges bordering the coax cable. Also, the excitation column of the hybrid system is nullified everywhere except for the N_C entries which are set to V_i. Once the hybrid FE-BI system is solved [5], the input admittance at z=0 is calculated from

$$
\begin{aligned}
Y_{in} &= \frac{1}{V_0}\oint_{2\pi}\mathbf{H}\cdot\hat{r}\,rd\phi \\
&= \frac{2I_0}{e_0ln(\frac{b}{a})} - \frac{1}{Z_C}.
\end{aligned} \tag{14}
$$

where Z_c is the characteristic impedance of the coax cable.

In the above feed model we assumed the presence of only the dominant(TEM) mode at the cavity-cable junction, an assumption which may not be suitable for certain applications.

To overcome this limitation, one approach is to extend the mesh (say, a distance d) into the cable. The equi–potential condition will then be applied at z=-d, where all higher order modes vanish. This scheme requires a more suitable expansion for the fields in the $-d < z < 0$ section to avoid the complication of extending the tetrahedral mesh into the cable and, thus, retain the efficiency of the equi–potential feed model. Since the antenna is, in most cases, operated in the frequency range far below the cut–off of the first higher order mode of the coax cable, the field distribution near the junction C will still be dominated by the fundamental TEM mode. With this understanding, a possible suitable expansion for the field in the coax cable (using shell elements rather than tetrahedrals) is

$$\mathbf{E} = \sum_q \sum_i^4 E_q^i \frac{\mathbf{N}_q^i(r,\phi,z)}{r}, \tag{15}$$

where q=r, ϕ or z, i=1,2,3 or 4 and $\mathbf{N}_q^i(r,\phi,z)$ is defined as

$$\mathbf{N}_{q_a}^i = \frac{\tilde{\epsilon}_i}{\Delta q_b \Delta q_c}(q_b - q_b')(q_c - q_c')\hat{q}_a \tag{16}$$

with q_a, q_b and q_c representing r, ϕ and z in a cyclic rotation. Also, i denotes the edge number along each coordinate, and Δq_a is the width of the edge along the $\hat{q}_a$ direction. The correspondence between the edge numbers and the node pairs for each coordinate(r, ϕ or z) is given in Table 1 along with the definition of the primed parameters and $\tilde{\epsilon}_i$ which carries the sign of the vector basis.

TABLE1

coordinates q	i	node pairs	parameters			
			$\tilde{\epsilon}$	r'	ϕ'	z'
r	1	(1–2)	+		$\phi_1 + \Delta\phi$	$z_1 + \Delta z$
	2	(4–3)	-		ϕ_1	$z_1 + \Delta z$
	3	(8–7)	+		ϕ_1	z_1
	4	(5–6)	-		$\phi_1 + \Delta\phi$	z_1
ϕ	1	(1–4)	+	$r_1 + \Delta r$		$z_1 + \Delta z$
	2	(5–8)	-	$r_1 + \Delta r$		z_1
	3	(6–7)	+	r_1		z_1
	4	(2–3)	-	r_1		$z_1 + \Delta z$
z	1	(1–5)	+	$r_1 + \Delta r$	$\phi_1 + \Delta\phi$	
	2	(2–6)	-	r_1	$\phi_1 + \Delta\phi$	
	3	(3–7)	+	r_1	ϕ_1	
	4	(4–8)	-	$r_+\Delta r$	ϕ_1	
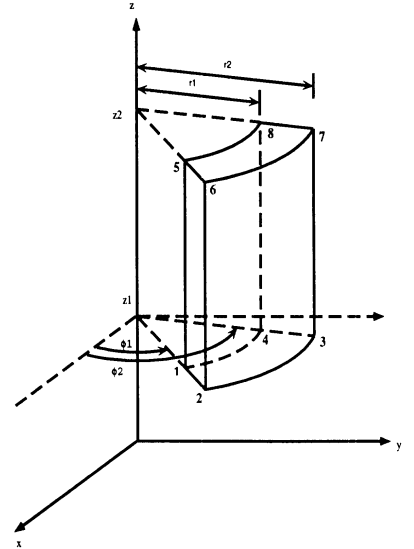
When an axisymmetric field property is assumed, the expansions reduce to

$$N_r^1 = \frac{(z - z_1)}{\Delta z}, \quad N_r^2 = -\frac{(z - z_1 - \Delta z)}{\Delta z}$$

$$N_z^1 = \frac{(r - r_1)}{\Delta r}, \quad N_z^2 = -\frac{(r - r_1 - \Delta r)}{\Delta r} \tag{17}$$

where (r_1, ϕ_1, z_1) denote the coordinates of node 1. The accuracy of expansion (17) is demonstrated in Figure 3, where we show that only 3 elements are needed along the radial direction for the accurate prediction of the dominant field distribution. When compared to the conventional linear tetrahedral elements, the efficiency of this expansion is apparent (i.e., many more tetrahedrals are needed to model the same cable region).

IV. Results and Conclusion

To validate our proposed feed simulation, two circular patch antenna configurations were used for calculation. One patch antenna was of radius 1.3 cm printed atop of a circular cavity (radius=2.1 cm) filled with a dielectric (ϵ_r=2.9) material 0.41 cm deep. For this patch, the feed was placed 0.8 cm from the center and the input impedance was measured over the band 2 – 5 GHz. In Figure 4 we compare the measured input impedance with data computed on the basis of the proposed equi-potential feed model. Clearly, the results from measurements and the equi–potential model are in excellent agreement whereas the probe model yields substantially inaccurate results near resonance.

Figure 5 shows the comparison between measurements and calculations for another patch antenna whose input impedance was measured by Aberle and Pozar [6]. This patch had a radius of 2.0 cm and the 0.218 cm thick substrate had ϵ_r=2.33 and a loss tangent $\tan\delta$=0.0012. The feed was located 0.7 cm from the center, and for our FE-BI calculation the patch was placed in a circular cavity of 2.44 cm in radius. As shown in Figure 5, the equi-potential model is again in excellent agreement with measurements, as opposed to the results by the probe model in [6] .

In conclusion, the presented equi–potential feed model has been shown to be extremely accurate in modeling coax feed structures. Moreover, its implementation in the context of a finite element formulation is very simple and as easy to implement as the probe feed. It was also demonstrated how the proposed feed model can be generalized to the case of asymmetric feed structures where evanescent modes may be present.

References

[1] J.P. Damiano and A. Papiernik,, "Survey of Analytical and Numerical Models for Probe-fed Microstrip Antennas," *IEE Proc. H.*, Vol. 141, No. 1, pp. 15–22, February, 1994

[2] J Zheng and D.C. Chang, "End-Correction Network of a Coaxial Probe for Microstrip Paths Antennas,' *IEEE Trans. Antennas Propagat.*, Vol. 39, No.1,pp. 115–118, January 1991

[3] W.C. Chew, Z. Nie, Q.H. Liu and Y.T. Lo, "Analysis of a probe-fed microstrip disk antennas," *IEE Proc. H*, Vol. 138, No. 2, pp. 185–191, 1991.

[4] J.L. Volakis, J. Gong and A. Alexanian, "Electromagnetic Scattering From Microstrip Patch Antennas and Spirals Residing in a Cavity," *Electromagnetics*, Vol. 14, No. 1, pp 63–85, 1994

[5] J. Gong, J.L. Volakis, A.C. Woo and H.G. Wang, "A Hybrid Finite Element-Boundary Integral Method for the Analysis of Cavity-backed Antennas of Arbitrary Shape," To appear in *IEEE Trans Antenna and Propagat.*, September 1994

[6] J.T. Aberle, D.M. Pozar and C.R. Birtcher,"Evaluation of Input Impedance and Radar Cross Section of Probe-Fed Microstrip Patch Elements using an Accurate feed model," *IEEE Trans. Antennas Propagat.*, Vol. 39, No.12, pp. 1691-1696. Dec. 1991

List of Figures

Figure 1: Illustration of a cavity-backed patch antenna with a coax cable feed.

(a)

(b)
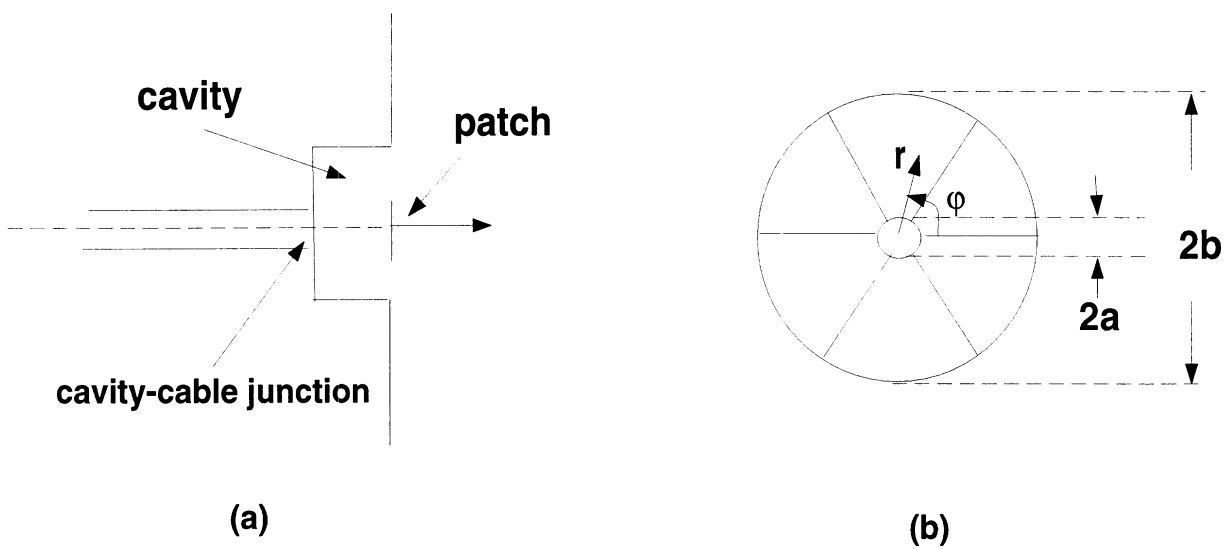
Figure 2: (a) Side view of a cavity-backed antenna with a coax cable feed; (b) Illustration of the FEM mesh at the cavity-cable junction.

55
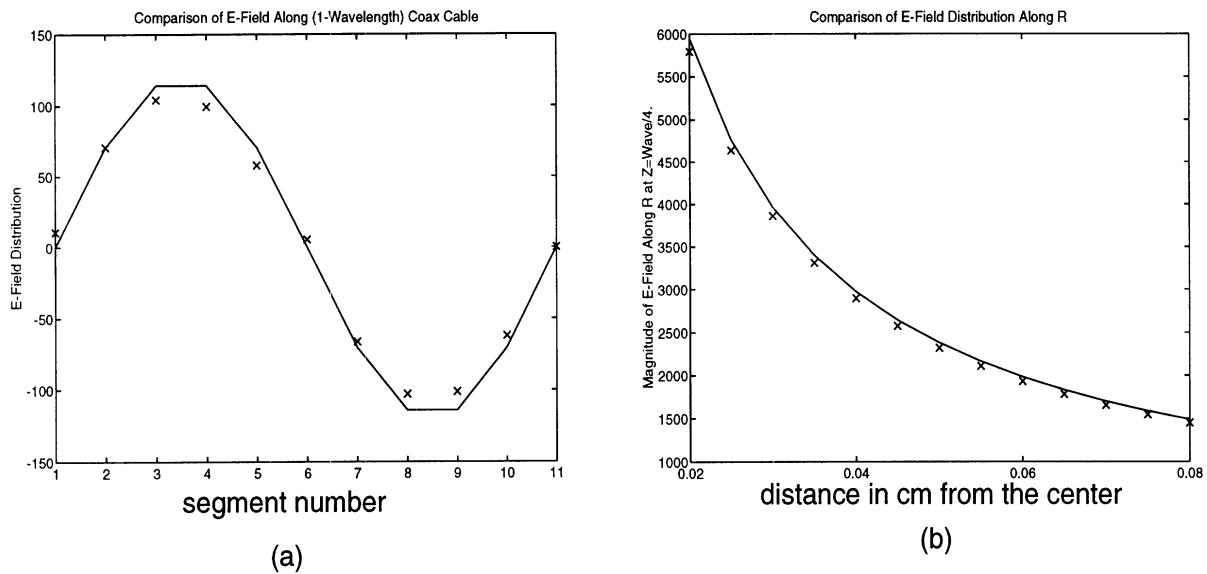
Figure 3: Field distribution in a shorted coax cable as computed by the finite element method using the expansion (14). —: analytical; xxx: numerical. (a) Field coefficient e_0 along the length of the cable (leftmost point is the location of the short); (b) Field along the radial coordinate calculated at a distance $\lambda/4$ from the shorted termination.
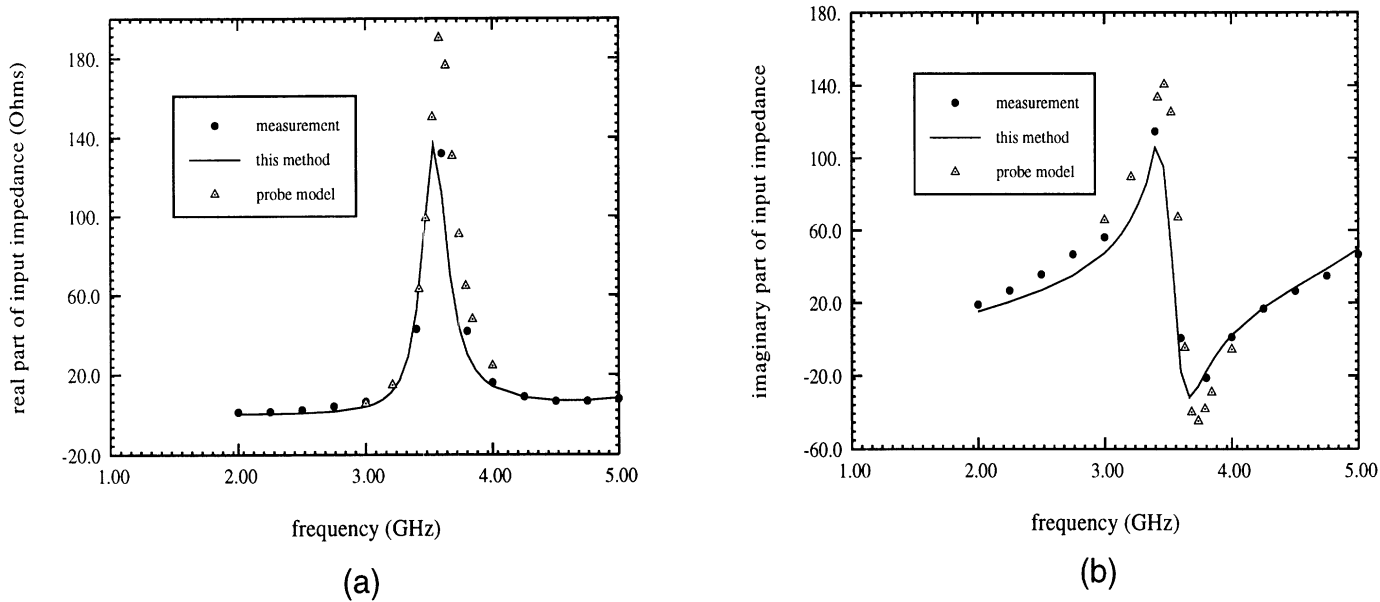
Figure 4: Measured and calculated input impedance for a cavity-backed circular patch antenna having the following specifications: patch radius r=13mm; cavity radius R=21.1mm; substrate thickness t=4.1mm; ϵ_r=2.4; and feed location x_f=0.8 cm distance from center. Results based on the simple probe model are also shown for comparison. (a) Real part; (b) Imaginary part.
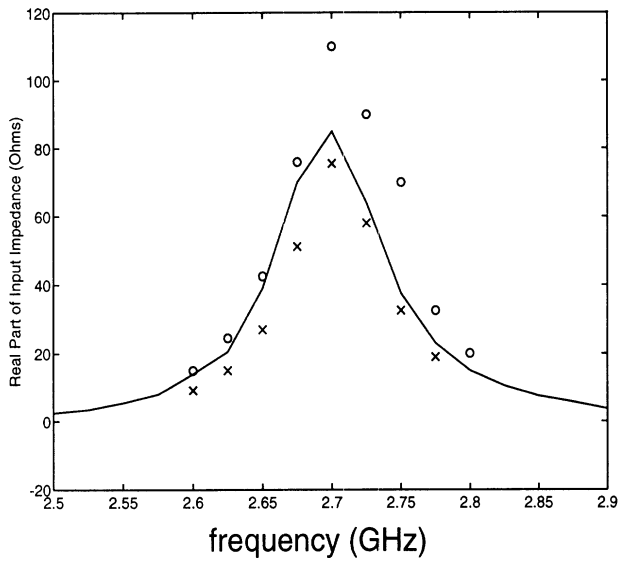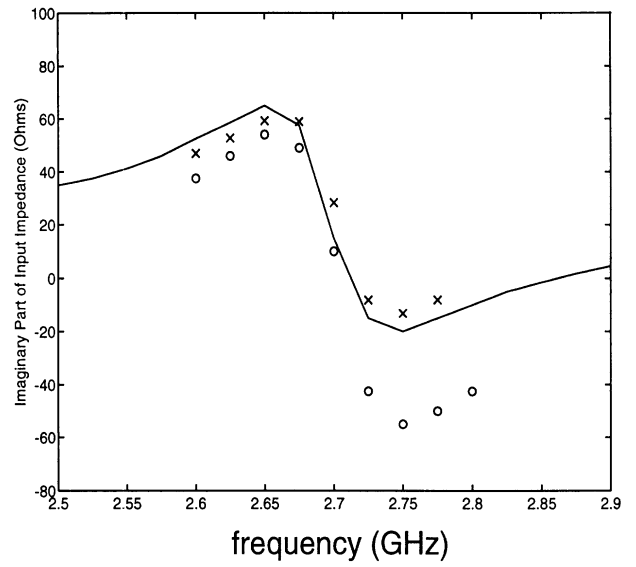
Figure 5: Measured and calculated input impedance for a circular patch antenna [6] having the following specifications: patch radius r=2cm; substrate thickness d=0.21844cm; feed location from center x_f=0.7cm; ϵ_r=2.33; $tan\delta$=0.0012. [6]. —: measurement; xxx: this method; o o o: probe model [6] (a) Real part; (b) Imaginary part.

Arbitrarily shaped Dual–stacked Patch Antennas: A Hybrid FEM Simulation

Jian Gong and John L. Volakis
Radiation Laboratory
Department of Electrical Engin. and Comp. Sci.
University of Michigan
Ann Arbor, MI 48109-2212

Abstract

A dual–stacked patch antenna is analyzed using a hybrid finite element – boundary integral (FE–BI) method. The metallic patches of the antenna are modeled as perfectly electric conducting (PEC) plates stacked on top of two different dielectric layers. The antenna patches may be of any shape and the lower patch is fed by a coaxial cable from underneath the ground plane or by an aperture coupled microstrip line. The ability of the hybrid FEM technique for the stacked patch antenna characterization will be stressed, and the EM coupling mechanism is also discussed with the aid of the computed near field patterns around the patches.

I. Introduction

Since being proposed, the dual stacked patch antennas received tremendous attention mainly because of the drastic improvement of their operational bandwidth in comparison to the inherent narrow band feature of single patch configurations. Further bandwidth improvement was also reported by employing an aperture coupled microstrip line, where the lower patch is electromagnetically coupled to a microstrip line through an opening at the ground

58

plane. This design was shown capable of achieving over 10% bandwidth. Certain numerical approaches for extensive analysis of non–rectangular single patch antennas with an aperture coupled feed have been investigated (e.g. [1, 2]). Unfortunately reports for non–rectangular stacked structure analyses have not been seen in the literature, except for experimental results published in [3, 4]). An analysis was only reported in [5] where the Hankel transform was employed on the assumption that the feed structure is absent from the analytical system. This implies that any change in the resonance due to the feed can not be modeled using this technique. A comprehensive simulation for stacked non–rectangular patch configurations is therefore desired for design purposes. This is the motivation of this report and we will discuss both probe and aperture coupled feeds. The former offers flexibility in the feeding network layout and makes the feed design separable from that of antenna elements [3], whereas the latter design, while challenging for most of the existing methodologies, is readily incorporated into our proposed hybrid FEM formulation, especially when the patches and the coupling opening (aperture) are non–rectangular for wider bandwidth designs.

In the following sections, we first briefly describe the hybrid FEM formulation as applied to the patch antenna analysis. More detailed discussions of the numerical approach may be found in [6] and [7]. Using our numerical simulator for characterizing the antenna's dielectric and geometric parameters, we concentrate on the microstrip feed line modeling with the aid of an FEM connectivity scheme. Some results for a circular stacked–patch antenna will be presented to show the ability of the technique, and typical computed 3-D near field distributions around the patches inside the two dielectric layers are displayed for visualization which reveals the insight of the EM coupling mechanism between the two patches.

II. Hybrid FEM Formulation

Consider the configuration of a stacked circular patch antenna shown in Figure 1, where a cavity encompassing the patches is recessed in the ground plane to simulate the truncation of the computational region V. As described in [6], the finite element method (FEM) is employed to model the fields in the three dimensional volume, whereas a boundary integral equation on the aperture of the cavity (excluding the metallic patch area) is built up based upon the equivalence principle to associate the radiated fields in the region above

59

the ground plane to those in the cavity so that the continuity conditions of the tangential fields across the aperture is inherently imposed. (Interested Readers are referred to [6] for detailed discussions and mathematical derivations.) It should be noted that the edge-based tetrahedral elements were used for the 3-D cavity fields and the triangular surface elements for the aperture fields simulation. The reasons are twofold (a) the edge elements have shown a precise representation of the vectorial electromagnetic fields without spurious modes; (b). arbitrarily shaped geometries and more sophisticated feeding schemes (e.g. aperture coupled stripline, microstrip line, equi–potential model for coaxial cable [8], etc.) are easier to model using edge elements. After the standard discretization and assembly procedures, we obtain a system of equations in a matrix form as

$$\sum_{j}^{N_V} [A_{i^v j}] \left\{ E_j^v \right\} + \sum_{j}^{N_S} [B_{i^s j}] \left\{ E_j^s \right\} = \left\{ K_{i^v} \right\}, \quad i = 1, 2, ..., N^V \tag{1}$$

where i^v and i^s represent the unknown indices in the cavity and on the aperture, respectively, and the former contains the latter in global numbering since the aperture fields E_j^s are part of the cavity fields E_j^v. N_V and N_S are the number of cavity and aperture edges that do not lie on any PEC surfaces. It is apparent that the total number of the system unknowns is N_V and, in most cases, $N_S \ll N_V$. This property is important because $[A_{i^v j}]$ is a sparse system although $[B_{i^s j}]$ is a full matrix. Thus the storage requirement is insignificant for this exact boundary truncation, which governs the modeling accuracy for the radiation problems.

In the case of stacked patch antennas, the lower patch is usually placed close to the cavity's base, which is treated as a grounded PEC wall. Hence, inside the FEM cavity, the lower patch should also be modeled as a PEC plate. Two separate dielectric layers above and below this patch must be considered to account for the substrate effects. Indeed, an attractive feature of the FEM over integral equation method is its capability to model multilayer structures with the same case as it does with the homogeneous structures.

III. Feed Simulations

Probe Feed

For the radiation analysis of a probe-fed patch antenna, we use the infinitesimally thin current source which is chosen to coincide with some mesh element edge. In this fashion, the excitation term $\{K_{iv}\}$ is usually modeled such that all the entries are set to zero except for those coincident with the probe(s) which link the patch and the ground plane. Specifically, if the probes are assumed to have a constant current $I_i, i = 1, 2, M_p$ (M_p is the number of the probes), then the excitation entries associated with the corresponding edges may be written as

$$K_i = -jkZ_0 I_i l_i, \tag{2}$$

where k is the free space wave number, Z_0 is the free space intrinsic wave impedance and l_i is the length of the ith edge. The phase difference between different probes may be readily represented by the phasor notation of each complex current I_i. Once the system of equations are solved, the input impedance is found to be

$$Z_{in} = \frac{E_i l_i}{I_i}, \tag{3}$$

where E_i denotes the calculated field along the ith edge of length l_i. The radiation pattern may be obtained by integrating the computed aperture fields with the far–zone approximation of the dyadic Green's function in the presence of an infinitely large PEC ground plane.

Microstrip line Feed

When the stacked patch antenna is fed with a microstrip line network underneath the ground plane (cavity's base) via a coupling aperture (see Figure 2), special treatment for the feed structure must be considered in the FEM formulation. This is because the microstrip line is usually designed to have different size and shape as compared to the cavity's geometric parameters. In addition, the microstrip line used as a transmission line, in most cases, carries traveling waves, thus, changing the field behavior in the cavity. Hence, the conventional FEM simulation treating the entire 3-D domain in a same fashion is not appropriate for this problem.

Consider the structure to be modeled as shown in Figure 3. In this case, it is appropriate to separate the computational domains because of the small element size required in modeling the feed structure. One difficulty encountered when this decomposition is implemented is how one must model the coupling through the aperture. (We consider in this report a rectangular aperture which has been extensively employed in practice. Other aperture shapes for wideband consideration have also been seen in the literature and this formulation can be readily extended for those designs.) As described in [6], the cavity fields are discretized using tetrahedral elements, whereas in the microstrip line rectangular brick elements are considered the best candidates for field modeling. The selection of brick elements is particularly useful because of the geometry and the field property of the microstrip line, and it is shown that this choice retains better accuracy and efficiency in comparison to other element selections. As shown in Figure 4, although both types of elements employ edge–based field expansions, the meshes across the common area (coupling aperture) are different, and this causes the inconsistency for the field representation in the formulation. In the implementation, this implies that the usual boundary condition for the tangential field continuity across the aperture can not be enforced in a straightforward manner.

We observe that the aperture is narrow in shape along the microstrip line and this fact allows us to assume a 'static' field feature for a given frequency. Therefore, the 'potential' concept may be applied to the problem in order to relate the fields below and above the aperture. Specifically, we enforce the 'equi–potential' continuity condition, which states that: the potential across the narrow aperture due to the field distribution in the cavity region must be equal to that due to the microstrip line excitation. If the edges are classified as

in mesh (b):

- E_j^{b1} $j = 1, 2, 3, ...$ *vertical   edges*

- E_j^{b2} $j = 1, 2, 3, ...$ *diagonal   edges*

in mesh (c):

- E_j^c $j = 1, 2, 3, ...$ *vertical   edgesonly*

then the 'equi–potential' continuity condition is expressed as

$$E_j^{b1} = \epsilon_j E_j^c \qquad (4)$$

$$E_j^{b2} = \frac{t}{2d}(\epsilon_j E_j^c + \epsilon_{j+1} E_{j+1}^c), \qquad (5)$$

where

$$\epsilon_j = \left\{ \begin{array}{l} 1 \\ -1 \end{array} \right. , \qquad (6)$$

t and d are the lengths of vertical and diagonal edges, respectively. (Thus, t happens to be the width of the narrow rectangular aperture.)

The connectivity scheme for entirely different computational domains may be extended by generalizing this concept. It is apparent that this approach makes the FEM implementation straightforward for different geometry/size domains that would be significantly inefficient if only one type of elements were used for modeling the structure. In addition, this technique ensures the system condition since the number of distorted elements in the mesh are minimized.

Results

As an example, a circular stacked patch antenna was used as shown in Figure 1, where the geometry parameters were designed for the antenna to be operated in the frequency range from 7 to 9 GHz. When excited using a microstrip line, it is observed that the field across the coupling aperture has a Gaussian–like distribution, as expected. Figure 5 shows the gain computed as a function of frequency and as seen, the design is indeed wideband, as promised. Figure 6–9 show the radiation patterns for both polarizations in the E–plane and H–plane, respectively, and Figure 10 plots the input impedance, whose VSWR is 2:1, corresponding to a bandwidth of 15%. In Figure 11, we show the magnitude of the computed field distribution on the antenna's radiating aperture when a probe feed was employed for excitation. It is noted that the energy is concentrated on the two opposite sides of the top patch and that the PEC cavity wall has little effect on the field near the antenna edges. Also, we observe from Figure 12 that the field couples to the lower patch from two locations even though only one probe is used for excitation.

References

[1] D. Zheng and K.A. Michalski, "Analysis of coaxial fed antennas of arbitrary shape with thick substrates," *J. Electromagn. Waves Appl.*, Vol. 25, No. 12, pp. 1303–1327, 1991

[2] J. Zheng and D.C. Chang, "End-Correction Network of a Coaxial Probe for Microstrip Paths Antennas,' *IEEE Trans. Antennas Propagat.*, Vol. 39, No.1, January 1991

[3] C.H. Chen, A. Tulintseff and R.M. Sorbello, *IEEE AP-S/URSI Symposium Digest*, pp 251–254, 1984

[4] Albert Sabban, "A New Broadband Stacked Two–layer Microstrip Antenna," *IEEE AP-S/URSI Symposium Digest*, pp. 63–66, 1983.

[5] K. Araki, H. Ueda and T. Masayuki, "Numerical Analysis of Circular Disk Microstrip Antenna With Parasitic Elements," *IEEE Trans. Antennas Propagat.*, Vol. 34, No. 12, pp 1390–1394, December, 1986

[6] J. Gong, J.L. Volakis, A.C. Woo and H. T. G. Wang, "A Hybrid Finite Element-Boundary Integral Method for the Analysis of Cavity-backed Antennas of Arbitrary Shape," *IEEE Trans Antenna and Propagat.*, Vol. 42, No. 9, pp 1233–1242, September 1994

[7] J.L. Volakis, J. Gong and A. Alexanian, "Electromagnetic Scattering From Microstrip Patch Antennas and Spirals Residing in a Cavity," *Electromagnetics*, Vol. 14, No. 1, pp 63–85, 1994

[8] J. Gong and J.L. Volakis, "An Efficient and Accurate Model For Coax Cable Feeding Structure Using Finite Element Method," Submitted to *IEEE Trans Antenna and Propagat.* for publication, 1994
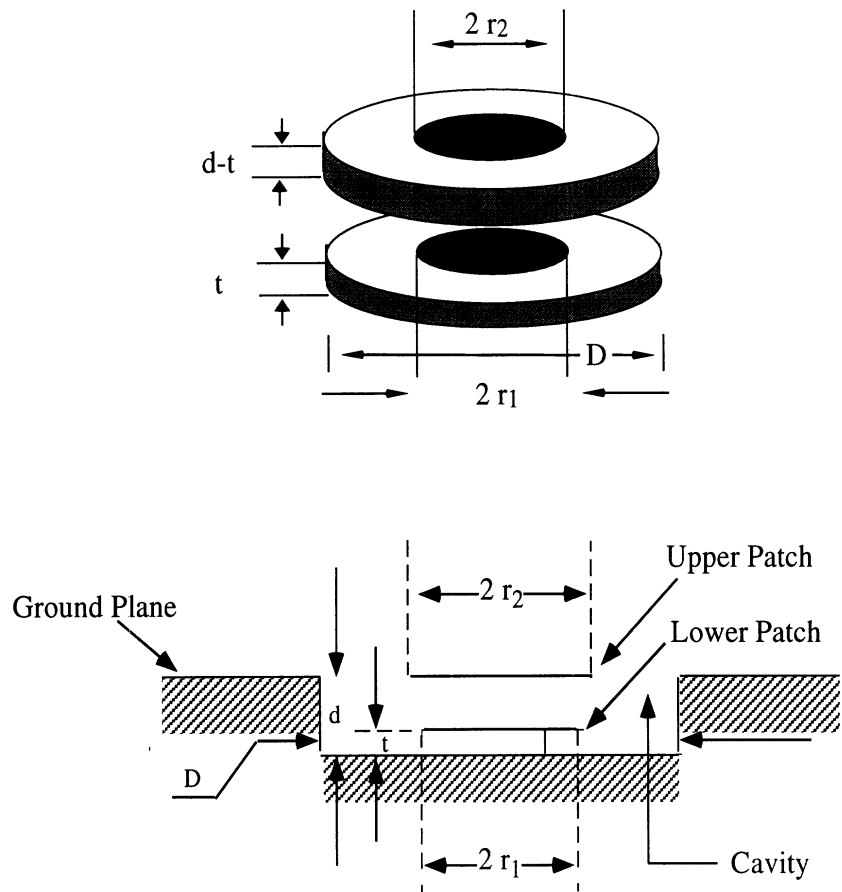
Figure 1: Illustration of A Cavity-backed Stacked Circular Patch Antenna, which could be fed by a probe or by an aperture coupled microstrip line.

FEM Mesh Terminated by
Assuming Dominant Mode

0.18128 cm

2r₂

2r₁

ε=1.12

ε=3.27

0.08128cm

d-t

t

air

0.16764 cm

ε=1.00

Feed

s

λ_g/4

0.05588 cm

Pins are placed
around stripline
to suppress higher
order modes

0.08cm

0.5802cm

0.1934cm

0.56cm
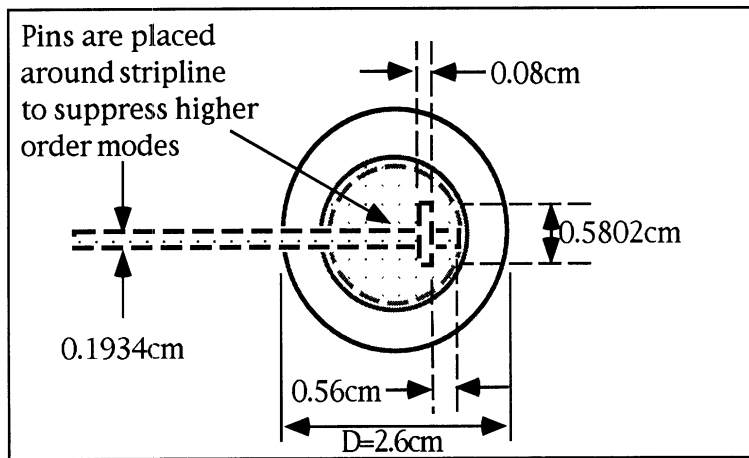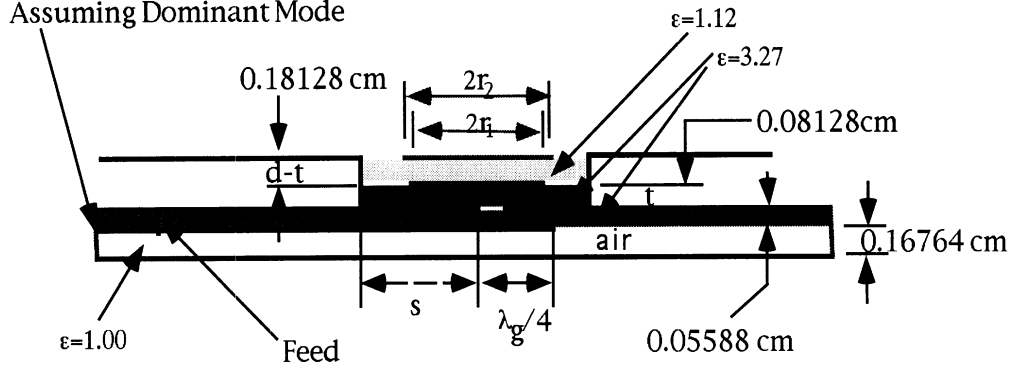
D=2.6cm

r₁ = 0.65 cm
r₂ = 0.75cm
t = 0.08128 cm
d-t = 0.18128 cm
d= 0.26256 cm
s= 0.2145cm

slot width=0.04 cm
λ_g= guided wavelength

D = 2.6 cm*   * Calculations were done using this cavity size.
Thus, performance will remain unchanged
when array elements are separated by comparable
distances. Tighter placement requires further
investigation to maintain performance within specs.

Figure 2: A stacked circular patch antenna with a microstrip line feed. The
design of geometric and dielectric parameters will be used for modeling.

66
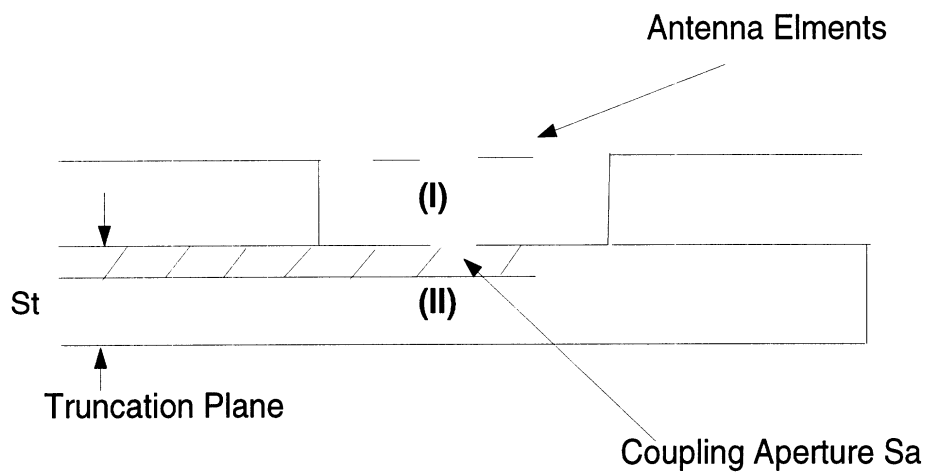
Figure 3: Cross–section of an aperture coupled patch antenna, showing the cavity region I and the microstrip line region II for two different FEM computation domains.

(a)
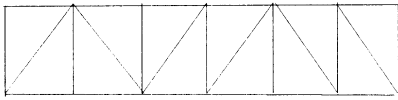
(b)

(c)

Figure 4: (a). a rectangular aperture; (b). a typical mesh from cavity region
I ; (c). the uniform mesh from microstrip line region II.
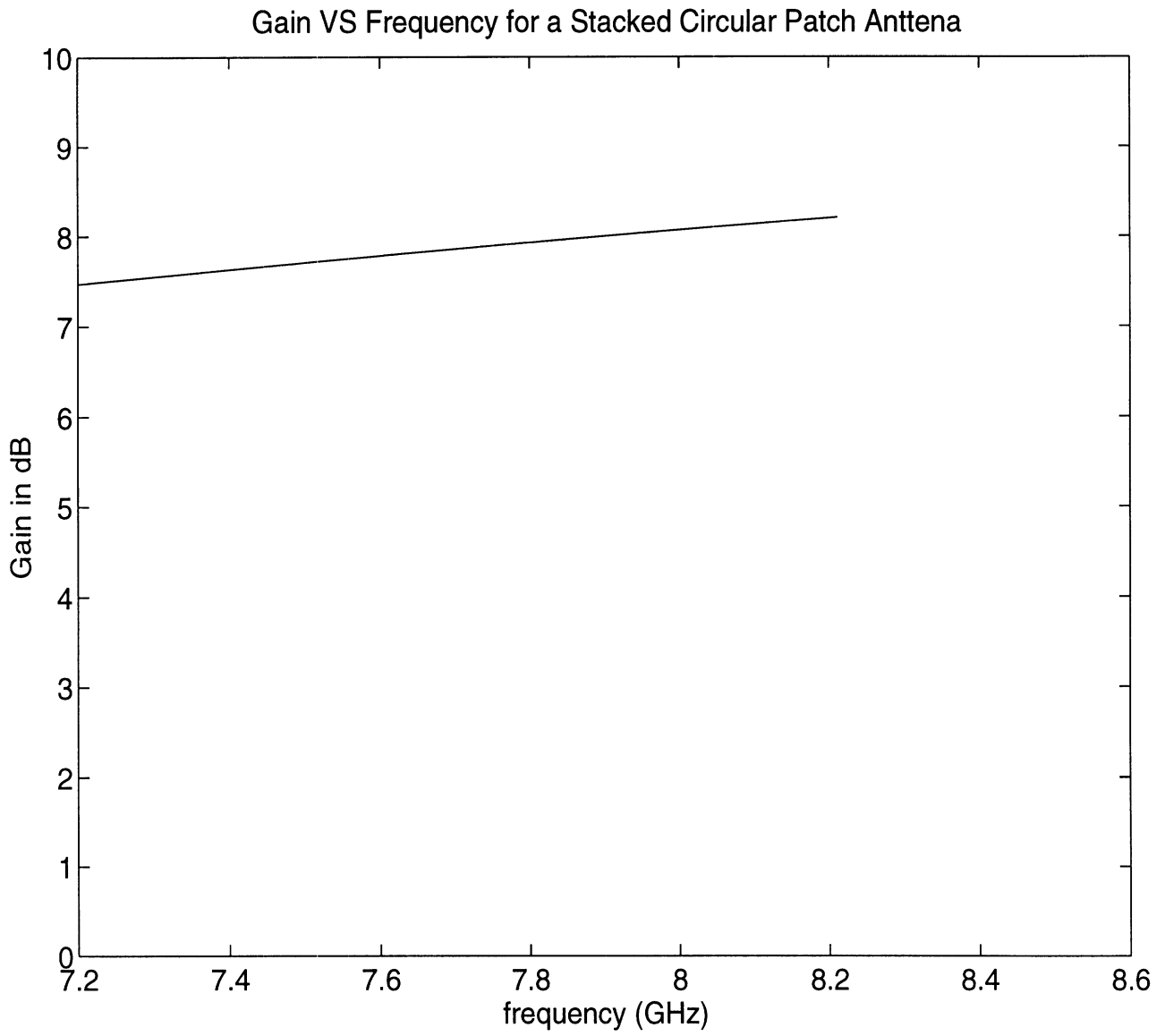
Figure 5: The gain pattern vs. freqency in GHz for circular stacked patch antenna.
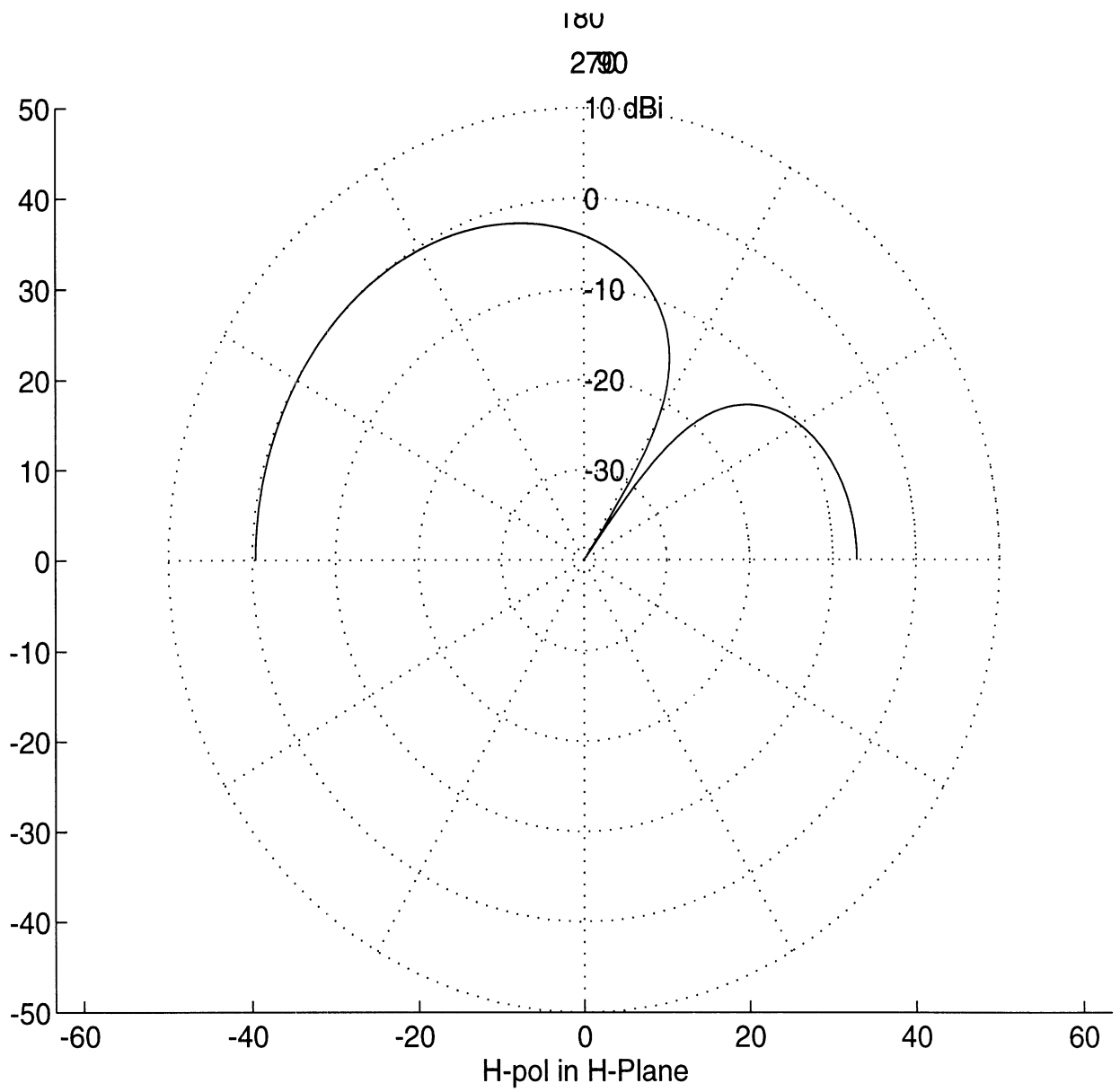
Figure 6:

Figure 7:

71

Figure 8:

72

Figure 9:

73
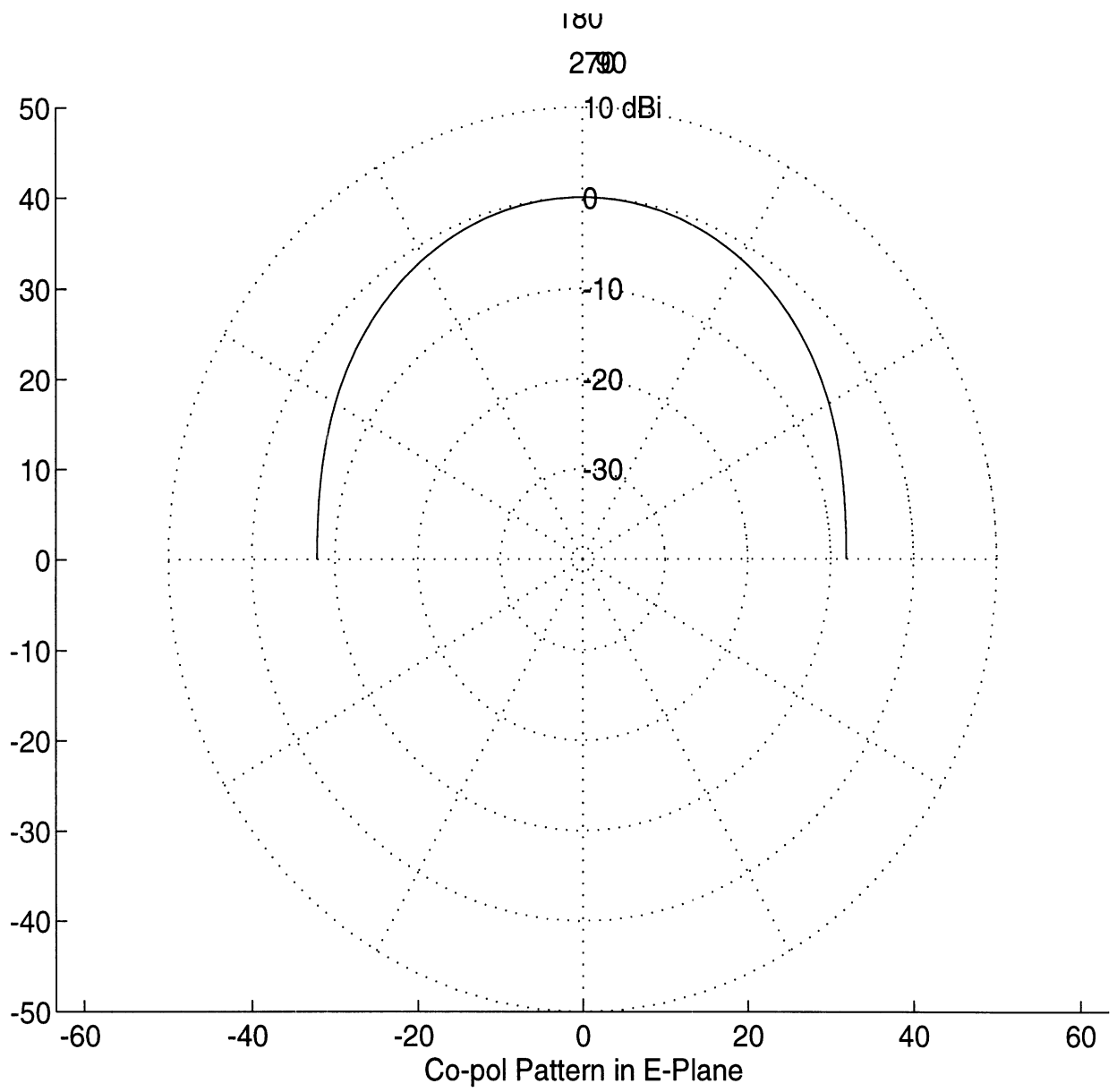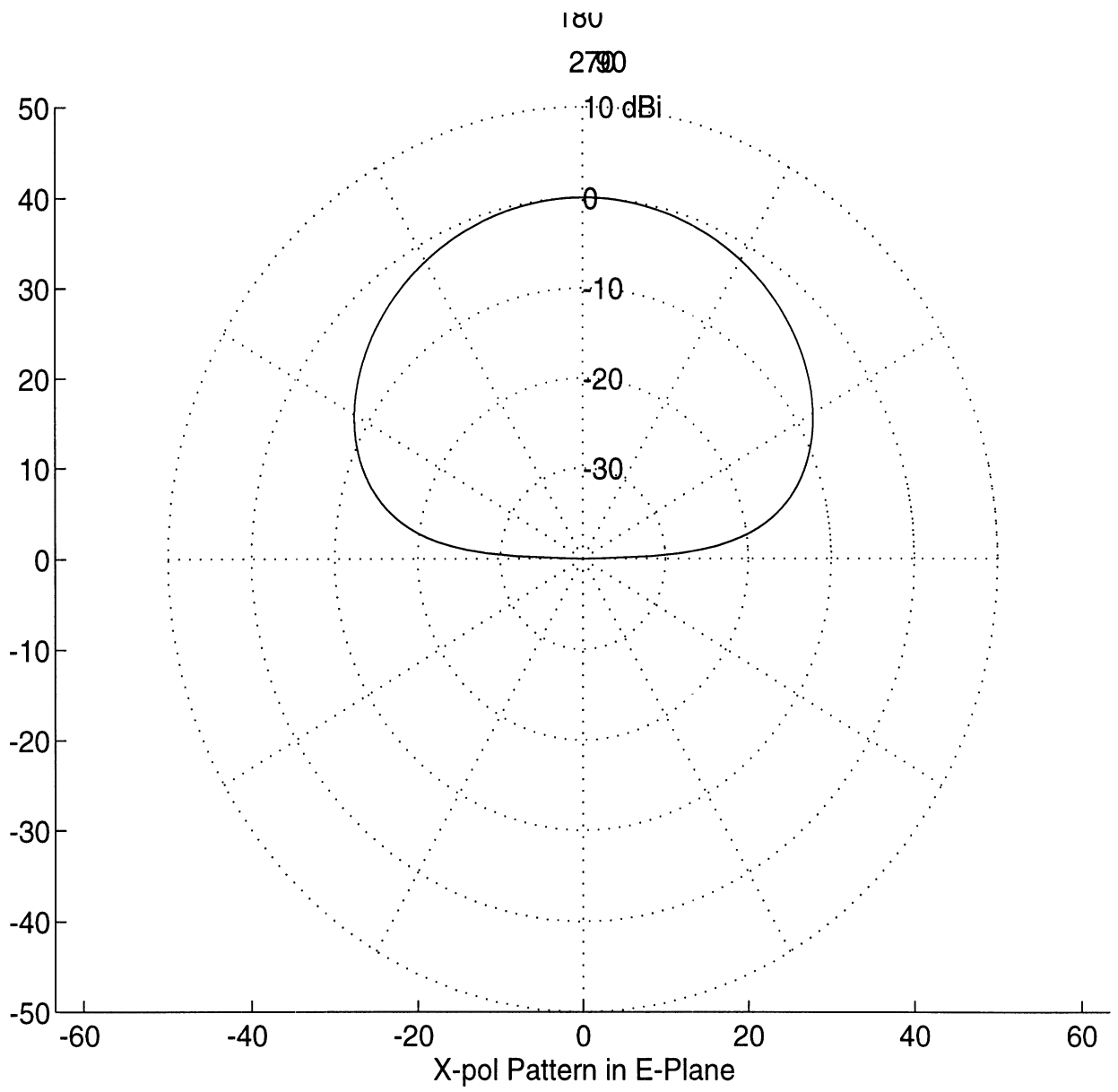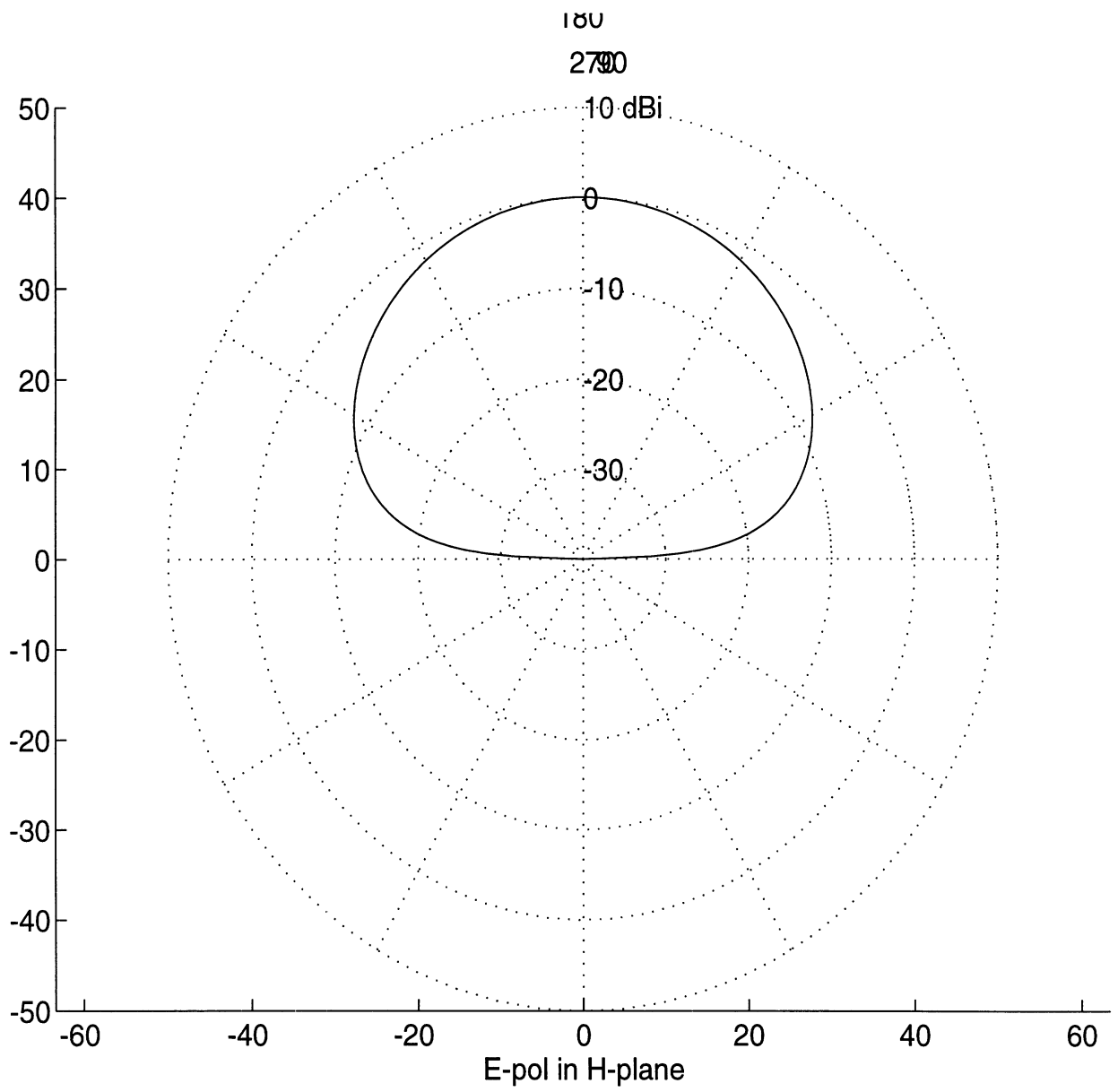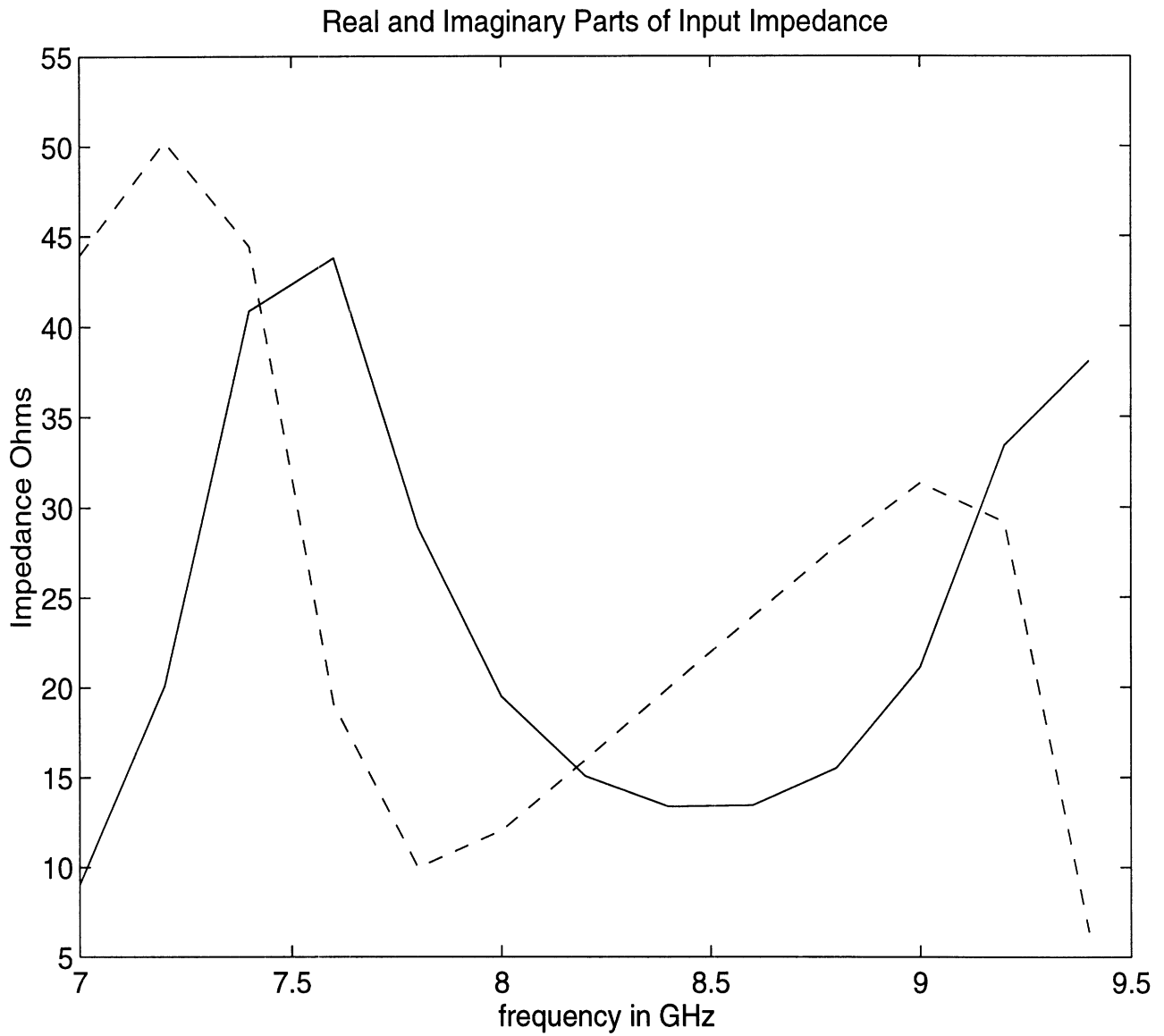
Figure 10: Input impedance vs. frequency in GHz for the circular stacked patch antenna. Solid line is for read part and dashed line for imaginary part.
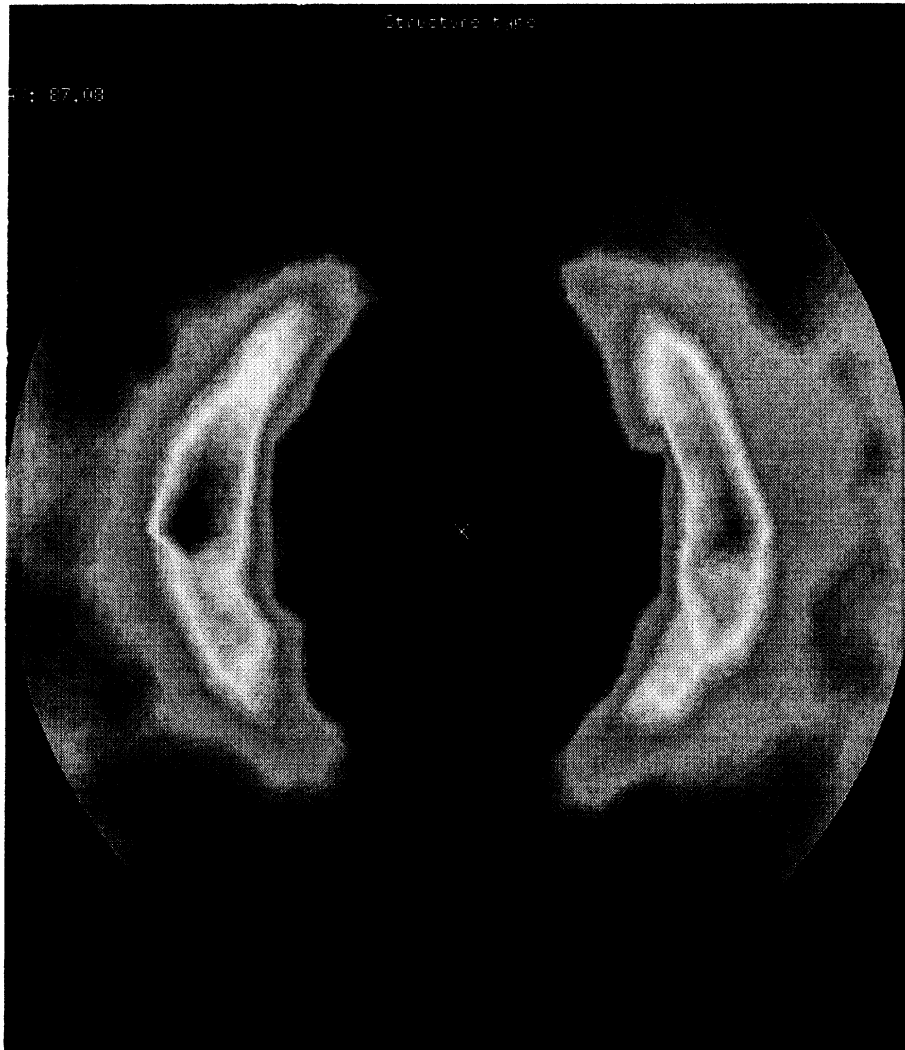
Figure 11: The field magnitude distribution on the antenna's radiating aperture. It is shown that the energy is concentrated on two opposite sides of the top patch and that the PEC cavity wall has little effect on the field.
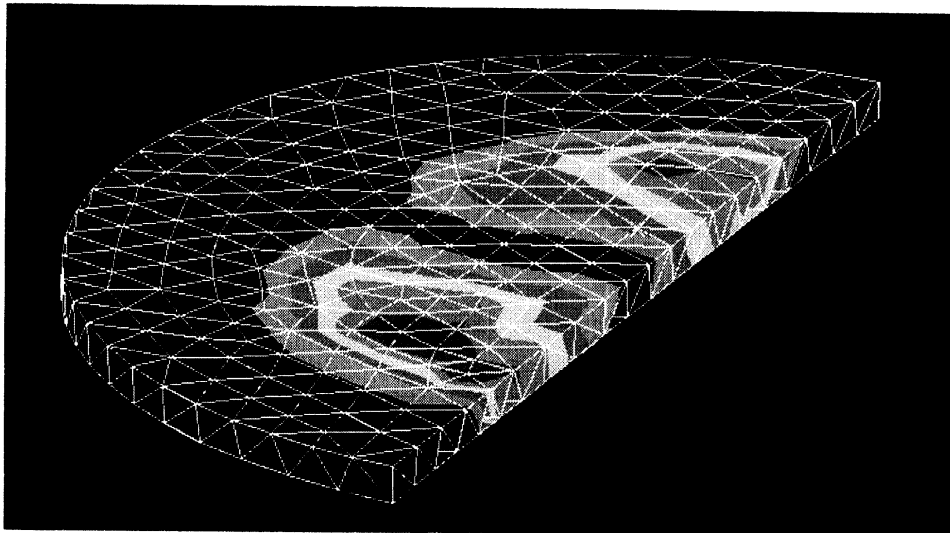
Figure 12: The field magnitude distribution within the cavity of the antenna excited by a probe. It is shown that the energy couples to the lower patch from two locations even though only one probe is utilized for excitation.

Performance of an Artificial Absorber for Truncating FEM Meshes

Jian Gong and John L. Volakis
Radiation Laboratory
Department of Electrical Engin. and Comp. Sci.
University of Michigan
Ann Arbor, MI 48109-2212

Abstract

We investigate the effectiveness of an artificial absorber for truncating finite element (FE) meshes. Specifically, we present the implementation of a novel mesh truncation approach using a perfectly matched anisotropic absorber for waveguides and stripline circuits. This truncation scheme is useful in many applications, including antennas, scattering and microwave circuits.

I. Introduction

One of the most important aspects of finite difference and finite element implementations is the truncation of the computational volume (see Figure 1). An ideal truncation scheme must ensure that the outgoing wave is not reflected backwards at the mesh termination surface, i.e. the mesh truncation scheme must simulate a surface which actually does not exist. To date, a variety of non–reflecting or absorbing boundary conditions (ABCs) have been employed for truncating the computational volume at some distance from the radiating or scattering surface. These conditions have also been extensively used in modeling microwave circuits and devices. The ABCs are typically second or higher order boundary conditions and are applied at the mesh termination surface to truncate the computational volume as required by any PDE solution. Many 2D and 3D variations of ABCs are nowadays available and several successful applications of these have been reported in the literature. Among them, a class of ABCs is based on the one–way wave equation/method [1, 2, 3] and another is derived starting with the Wilcox Expansion [4, 5]. Also, higher order ABCs using the Higdon [6] or Liao [7] formulation and problem specific numerical ABCs have been successfully used particularly for

77

truncating needs in guided structures. There are several difficulties with traditional ABCs. Among them is the need to apply them at some distance from the perturbance (leading to a large computational volume) and their limited accuracy particularly for truncating meshes atop of radiating elements or in guided structures. The latter prompted the use of higher order ABCs using the Higdon or Liao formulation (see [8, 9, 10]) and a variety of numerical ABCs [11, 12]. Nevertheless, regardless of the improvements realized by higher order and numerical ABCs, they substantially complicate the implementation of PDE techniques especially when inhomogeneity is present and when parallelization of the codes is needed.

An alternative to the traditional ABCs is to employ an artificial absorber for mesh truncation. Basically, instead of an ABC, a thin layer of absorbing material with $\epsilon_r = \mu_r$ is used to truncate the mesh as illustrated in Figure 2. Typically, the absorber must be 0.15 λ thick and so far only homogeneous layers have been investigated [13]. Such absorbing layers are therefore necessarily narrow band in addition to exhibiting a non–vanishing reflection coefficients for angles near grazing. One approach to overcome both of these difficulties is to employ a uniaxial rather than an isotropic material layer and in this communication we examine the performance of such a mesh truncation scheme in the context of a finite element implementation. More specifically, the uniaxial absorbing layer is employed for truncating meshes in waveguide and stripline propagation problems.

II. Formulation

Consider the rectangular waveguide and a shielded stripline structure in Figure 3. We are interested in modeling the wave propagation in these structures using the finite element method. For a general anisotropic medium, the functional to be minimized is

$$\mathcal{F} = \int_V \nabla \times \mathbf{E} \cdot (\overline{\overline{\mu}}_r^{-1} \cdot \nabla \times \mathbf{E}) - k_0^2 \overline{\overline{\epsilon}}_r \cdot \mathbf{E} \cdot \mathbf{E} \, dV$$

$$- \int_{S_{in}+S_{out}} \mathbf{E} \times (\overline{\overline{\mu}}_r^{-1} \cdot \nabla \times \mathbf{E}) \cdot dS, \tag{1}$$

in which $\overline{\overline{\mu}}_r$ and $\overline{\overline{\epsilon}}_r$ denote the permeability and permittivity tensors whereas $\mathbf{E}$ is the total electric field in the medium. The surface integrals over S_{in} and S_{out} must be evaluated by introducing an independent boundary condition and the ABC serves for this purpose but alternatively an absorbing layer may be used as illustrated in Figure 2. One approach in evaluating the performance of an absorbing layer for terminating the FE mesh is to extract the reflection coefficient computed in the presence of the absorbing layer used to terminate the guided structure. In this study we consider the performance of a thin uniaxial layer for terminating the FE mesh in a rectangular waveguide and a stripline. Such a uniaxial layer was proposed by Sacks *et.al.* [14] who considered the plane wave reflection from an

78

anisotropic interface (see Figure 4). If $\overline{\overline{\mu}}_r$ and $\overline{\overline{\epsilon}}_r$ are tensors of the form

$$\overline{\overline{\mu}}_r = \overline{\overline{\epsilon}}_r = \begin{pmatrix} a & 0 & 0 \\ 0 & b & 0 \\ 0 & 0 & 1/c \end{pmatrix} \tag{2}$$

the TE and TM reflection coefficients at the interface are

$$
\begin{aligned}
R^{TE} &= \frac{\cos\theta_i - \sqrt{\frac{b}{a}}\cos\theta_t}{\cos\theta_i + \sqrt{\frac{b}{a}}\cos\theta_t} \\
R^{TM} &= \frac{\sqrt{\frac{b}{a}}\cos\theta_t - \cos\theta_i}{\cos\theta_i + \sqrt{\frac{b}{a}}\cos\theta_t}
\end{aligned}
\tag{3}
$$

and by choosing $a = b$ and $c = \frac{1}{b}$ it follows that $R^{TE} = R^{TM} = 0$ for all incidence angles, implying a perfectly matched material interface. Moreover, by setting $a = \alpha - j\beta = 1 - j\beta$ the reflected field of such a metal-backed uniaxial layer is

$$|R(\theta_i)| = e^{-2\beta k_0 t \cos\theta_i} \tag{4}$$

where t is the thickness of the layer and θ_i is the plane wave incidence angle. Basically, the proposed metal backed uniaxial layer can have a reflectivity of as much as -17 dB if $\beta t \cos\theta_i = 0.16\lambda_0$, where λ_0 is the free space wavelength. The reflection coefficient (4) can be reduced further by backing the layer with an ABC rather than a PEC. However, the PEC backing is more attractive because it eliminates altogether the integrals over the surfaces.

Below we present a number of results which show the performance of the proposed uniaxial absorbing layer as a function of the parameter β, the layer thickness t and the frequency for a waveguide and a stripline under single mode operations.

Results

Let us first consider the rectangular waveguide shown in Figure 3. The guide's cross–section is chosen to propagate only the TE_{10} mode and is excited by an electric probe at the left. Figure 5 shows the mode field strength inside the waveguide which has been terminated by a perfectly matched uniaxial layer having $\beta = 4.2$ and thickness $t = 1.0cm$. Clearly, the field amplitude is fairly constant once away from the probe indicating a small VSWR. Plots which illustrate the performance of this uniaxial layer as a function of frequency for different values of β are shown in Figure 6. The plots show that for $\beta = 4.2$ the reflection coefficient is less than -17 dB over a broad range of frequencies. Interestingly, different values of β can have a better performance (see Figure 9) but most importantly, in all cases, the broadband performance is maintained.

The performance of the perfectly matched uniaxial layer in absorbing the shielded stripline mode is illustrated in Figure 7. In this case, the stripline is

extended into the absorbing layer up to the metallic wall. We observe that the predicted reflection coefficient is now around -13 dB and nearly independent of β. In comparison to the rectangular waveguide example, there is a 4 dB reduction in absorption and this is likely due to the extension of the substrate within the absorbing layer.

A most surprising observation on the performance of this uniaxial layer for truncating finite element meshes is extracted from Figure 8. In this figure, we plot the reflection coefficient as a function of layer thickness (actually as a function of the number of elements used in modeling the layer). It is seen that the performance of the layer for truncating the FE mesh is maintained reasonably well even when two to three sample elements are used within the layer. That is, the proposed perfectly matched uniaxial layer bares no computational burden on the simulation. In fact, it is even simpler to apply this anisotropic absorbing layer than the first order ABC since the PEC backing eliminates the surface integral from the FE formulation.

Conclusions

We examined the performance of a new perfectly matched absorbing layer for truncating FE meshes. Examples relating to propagation in a rectangular waveguide and a stripline were considered and it was demonstrated that a very thin metal–backed anisotropic layer was sufficient to achieve a reflection coefficient which in most cases was -15 dB or less. Surprisingly, the layer could be modeled with as few as two elements across its thickness and its overall implementation was rather simple because of the metal backing. Such an absorbing layer is particularly useful in truncating meshes in guided structures and should be found as useful in the application of finite element methods to scattering prediction and open microwave circuit simulation.

References

[1] B. Engquist and A. Majda, "Absorbing boundary conditions for the numerical simulation of waves," *Math. Comput.* Vol. 31, pp. 629–651, 1977

[2] L.Halpern and L.N. Trefethen, "Wide–angle one-way wave equations," *J. Acoust. Soc. Amer.* Vol. 84, pp. 1397–1404, 1988

[3] W. Sun and C.A. Balanis, "Vecter one–way wave absorbing boundary conditions for FEM applications," *IEEE Trans. Antennas Propagat.* Vol. AP–42, pp. 872–878, 1994

[4] Webb and Kanellopoulos, " Absorbing boundary conditions for the finite element solution of the vector wave equation," *Microwave Opt. Tech. Lett.* Vol. 2, pp. 370–372, 1989

[5] A. Chatterjee and J.L.Volakis, "Conformal absorbing boundary conditions for the vector wave equation," *Microwave Opt. Tech. Lett.* Vol. 6, pp. 886–889,1993

[6] R.L. Higdon, "Absorbing boundary conditions for acoustic and elastic waves in stratified media," *J. Comp. Phys.* Vol. 101, pp. 386–418, 1992

[7] Z.P. Liao H.L. Wong, B.P. Yang and Y.F. Yuan, "A transmitting boundary for transient wave analysis," *Sicentia Sinica* Vol. 28, pp. 1063–1076, 1984

[8] M. Moghaddam and W.C. Chew, "Stabilizing Liao's absorbing boundary conditions using single–precision arithmetic," it IEEE AP-S Int. Symp., London, Canada, pp. 430–433, 1991

[9] J.Fang, "ABCs applied to model wave propagation in Microwave integrated-circuits," *IEEE Trans. MTT*, Vol. 42, No. 8, pp. 1506–1513, Aug. 1994

[10] R. Luebbers and C. Penney, "Scattering from apertures in infinite ground planes using FDTD," *IEEE Trans. Antennas Propagat.* Vol. 42, pp. 731–735, May 1994

[11] B. Stupfel and R. Mittra, "Efficiency of numerical absorbing boundary conditions for finite element applications," *URSI Radio Science Meeting*, pp. 165, 1994

[12] K.K. Mei, R. Pous, Z. Chen, Y.W. Liu amd M.D. Prouty, " Measured equation of Invariance: A new concept in field computations," *IEEE Trans. Antennas Propagat.* Vol. 42, pp. 320–328, March 1994

[13] T. Özdemir and J.L.Volakis, "A comparative study of an absorbing boundary condition and an artificial absorber for truncating finite element meshes," *Radio Science* Vol. 29, No. 5, pp. 1255–1263, Sept. 1994

[14] Z.S. Sacks, D.M. Kingsland, R. Lee and J.F. Lee, "A perfectly matched anisotropic absorber for use as an absorbing boundary condition," *Submitted for publication*, 1994
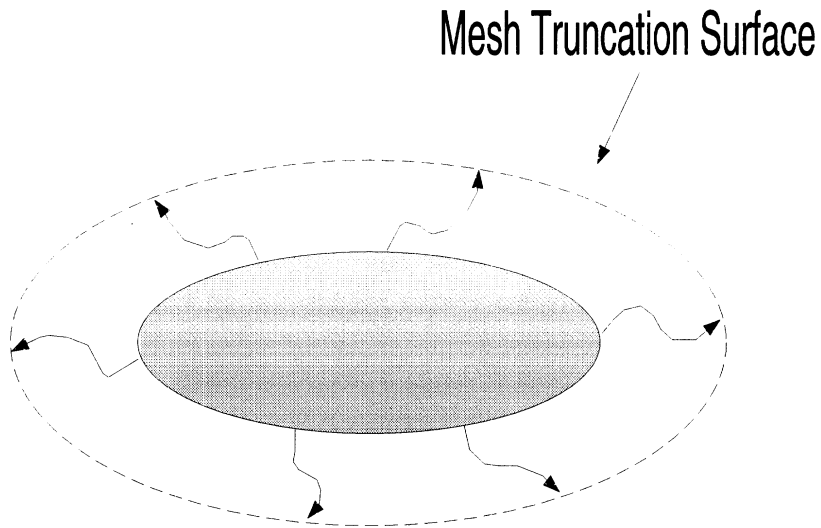
List of Figures

Figure 1: Mesh truncation using an artificial absorbing surface.
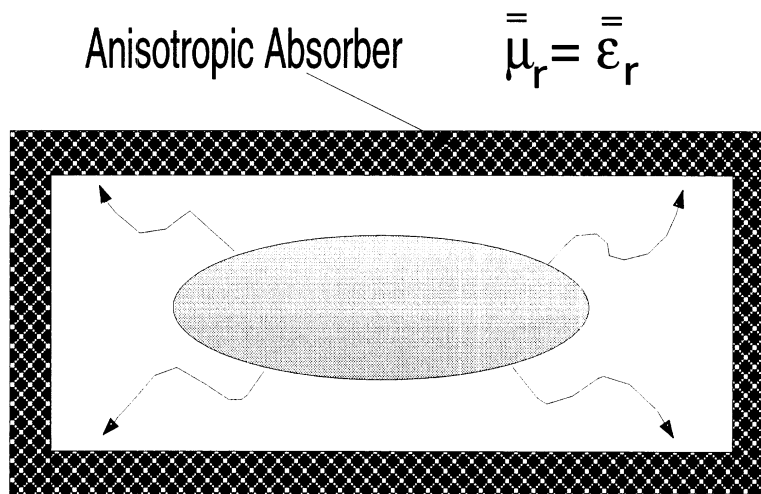
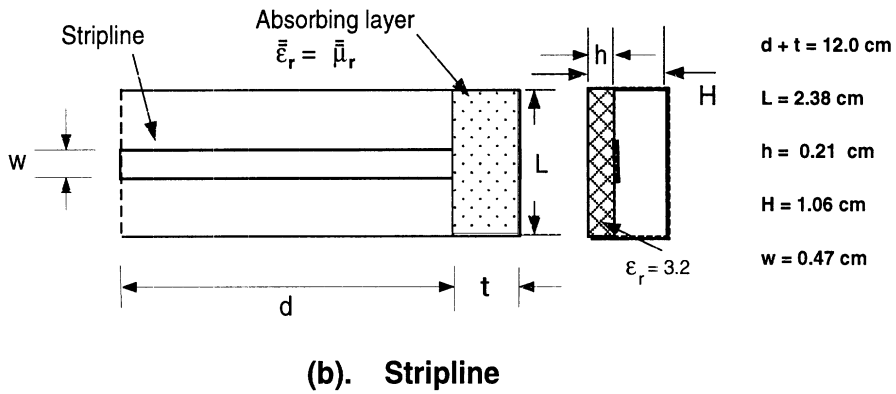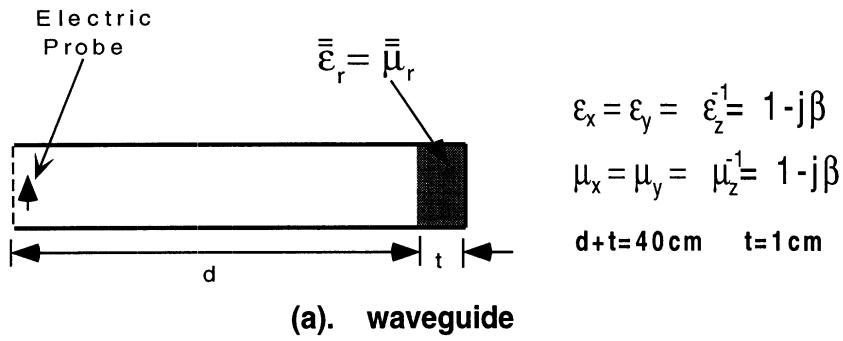
Figure 2: Mesh truncation using a thin anisotropic layer.

(a). **waveguide**

$$\bar{\bar{\varepsilon}}_r = \bar{\bar{\mu}}_r$$

$$\varepsilon_x = \varepsilon_y = \varepsilon_z^{-1} = 1 - j\beta$$

$$\mu_x = \mu_y = \mu_z^{-1} = 1 - j\beta$$

$$d + t = 40\,cm \qquad t = 1\,cm$$

(b). **Stripline**

d + t = 12.0 cm

L = 2.38 cm

h = 0.21 cm

H = 1.06 cm

w = 0.47 cm

$\varepsilon_r = 3.2$

Figure 3: A rectangular waveguide (a) and a stripline (b) truncated using the perfectly matched uniaxial absorbing layer.
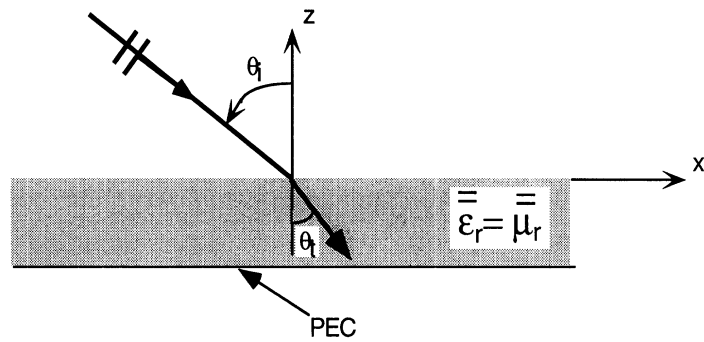
Figure 4: Illustration of plane wave incidence on an anisotropic interface.

84
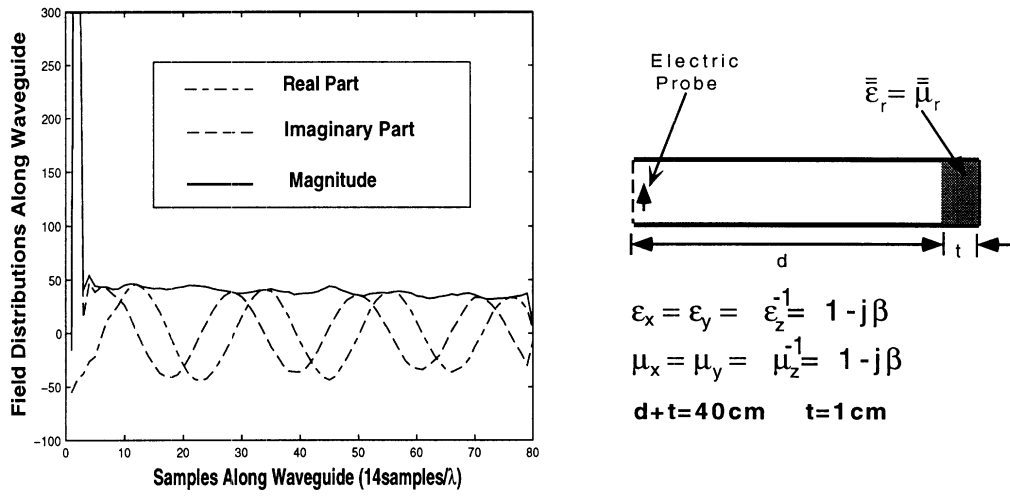
Figure 5: Typical field values of the TE_{10} mode inside a rectangular waveguide terminated by a perfectly matched uniaxial layer.
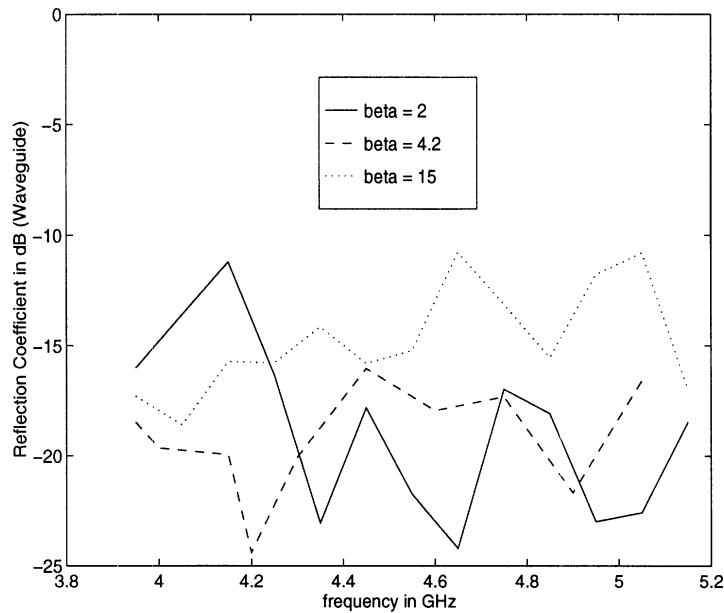

Figure 6: Reflection coefficient vs frequency for the perfectly matched uniaxial layer used to terminate the waveguide shown in Figure 3.
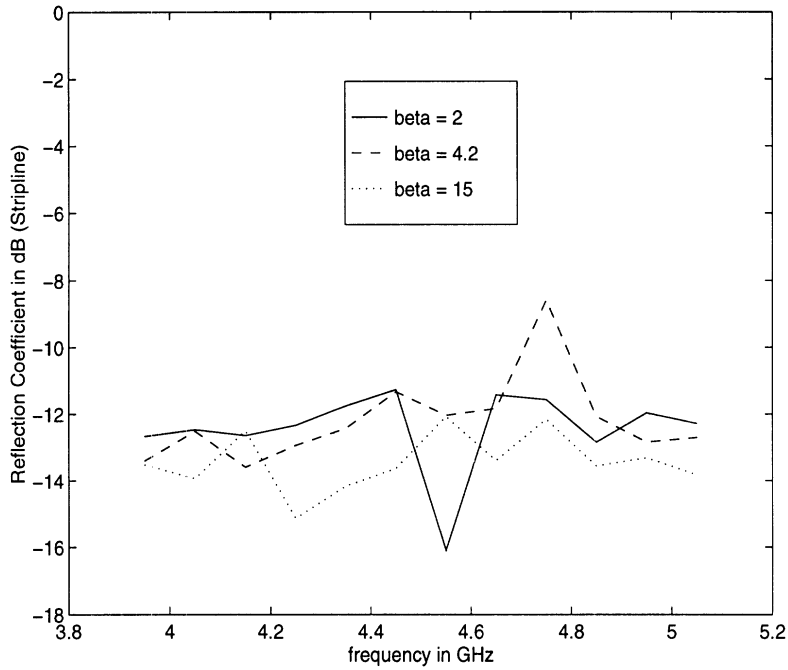
85

Figure 7: Reflection coefficient vs frequency for the shielded stripline terminated by the perfectly matched uniaxial layer.
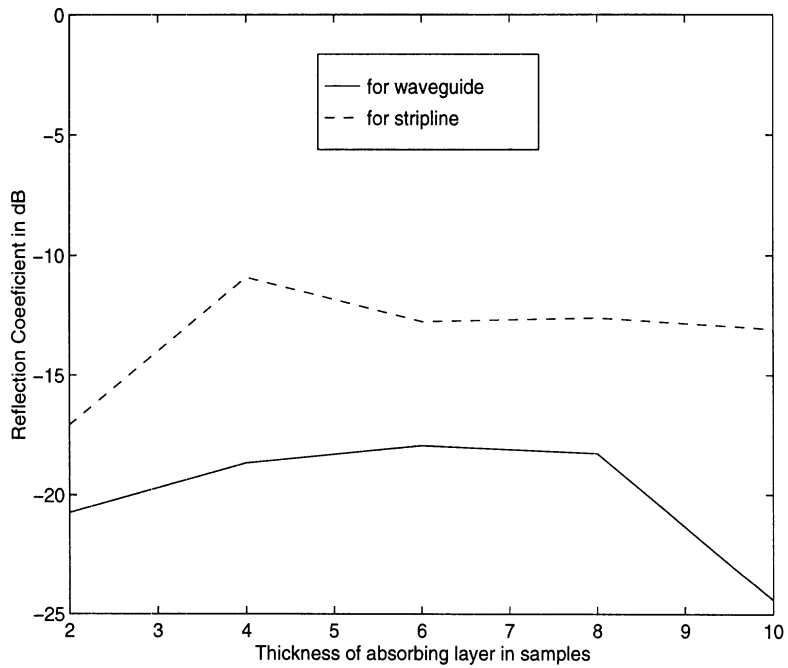

Figure 8: Reflection coefficient vs thickness t of the perfectly matched uniaxial layer for f = 4.2 GHz and β= 4.2.
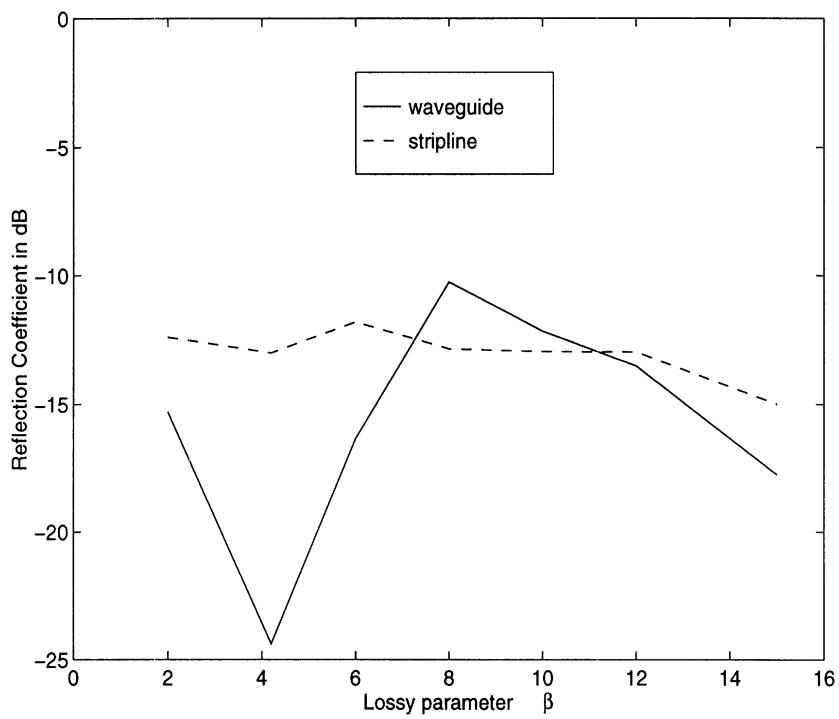
Figure 9: Reflection coefficient vs β of the perfectly matched uniaxial layer for f = 4.2 GHz and t = 10 samples.